BIOREACTIVE SEMICONDUCTOR SURFACES: PREPARATION AND CHARACTERIZATION

by

Hidehiko Asanuma
B.Sc., Simon Fraser University, 2004

THESIS
SUBMITTED IN PARTIAL FULFILLMENT OF
THE REQUIREMENTS FOR THE DEGREE OF

DOCTOR OF PHILOSOPHY

In the
Department
of
Chemistry

SIMON FRASER UNIVERSITY

Summer 2009

Approval

Name: **Hidehiko Asanuma**

Degree: **Ph.D.**

Title of Thesis: **Bioreactive semiconductor surfaces: preparation and characterization**

Examining Committee:

Chair: **Dr. Michael Eikerling, Assistant Professor**

_____

Dr. Hua-Zhong Yu, Associate Professor
Senior Supervisor

_____

Dr. Gary W. Leach, Associate Professor
Committee member

_____

Dr. Melanie A. O'Neill, Assistant Professor
Committee member

_____

Dr. Vance E. Williams, Associate Professor
Internal Examiner

_____

Dr. Richard L. McCreery, Professor
External Examiner
Department of Chemistry
University of Alberta

Date Defended/Approved: August 17, 2009

Declaration of
Partial Copyright Licence

Abstract

Bioreactive surfaces are seminal to the fabrication of semiconductor-based biochip devices. Their efficient preparation by the reaction of silicon with organic molecules, and the characterization of the formed monolayer films with spectroscopic and electrochemical techniques were the main objectives of the research described in this thesis.

For the formation of a carboxy-terminated monolayer on silicon the conventional protocol consists of two steps: thermally or photochemically initiated reaction of an ester (CH_2=CH(CH_2)$_x$COOR) with hydrogen-terminated silicon (111) and subsequent hydrolysis under acidic conditions. Vibrational sum frequency generation (SFG) spectroscopic studies have shown that the ester hydrolysis is incomplete and disrupts the molecular orientation (order) of the monolayer structure.

Searching for a more direct route to bioreactive silicon surfaces, the kinetics of photochemical reactions of silicon with various organic molecules were investigated. It was found that under UV irradiation, alkenes react much faster than alkanoic acids. Therefore, the reaction of bifunctional molecules (e.g., ω-alkenoic acids) can be controlled to preferentially attach the alkene terminus to the silicon surface. Such a one-step reaction eliminates the complications encountered during ester hydrolysis (low efficiency, structural disruption of the monolayer, and possible oxidation of the silicon substrate).

Studies of DNA monolayers immobilized on silicon revealed that their molecular orientation depends on the DNA-cation affinity: during immobilization of single-stranded DNA, the perturbation of molecular orientation of the monolayer occurred in the order $Mg^{2+} > Ca^{2+} > K^{+} \sim Na^{+}$, whereas, during hybridization, disruption of the monolayer occurred in the order $K^{+} \sim Na^{+} > Mg^{2+} \sim Ca^{2+}$.

A reliable metal contact on top of organically modified silicon is vital for solid-state electrical measurements. The thermal and sputtering metal deposition protocols have been assessed with SFG spectroscopy and by the electrical characterizations (J-V and Mott-Schottky); the deposited gold penetrated and damaged the monolayers in both cases. Therefore, a device using a mercury drop electrode was designed and tested with the hydrogen terminated and the decane monolayer on silicon (111). The J-V curves proved that the mercury contact preserved the monolayer (no damages were introduced). Furthermore, the capabilities of the device to reveal electrical properties such as effective barrier height and ideality factor in relation to the molecular structures of ω-functionalized monolayers have been demonstrated. These findings are seminal to the future development of DNA-based molecular junctions.

Keywords: silicon, monolayer, surface chemistry, DNA, biochip, molecular electronics, metal contact.

Thanks

Coco for the perspective and spirit

Bob for the wisdom and creativity

Acknowledgements

During graduate studies, I have enjoyed the opportunity to meet and work with many amazing people. The time I have spent here at SFU and Hokkaido University have forever altered the course of my life. As an undergraduate student, I had no intention of pursuing an advanced degree. This changed after I met my supervisor, Dr. Hogan (Hua-Zhong) Yu. He told me all the pros about being a researcher; the intellectual endeavours will keep your mind active and curious, not only in science, but with everyday life. Although I quickly learned that research is not filled with excitement all the time, he was right. I have enjoyed the five years of research. It was a lot of fun. I am truly thankful for Dr. Hogan Yu for providing me such an opportunity. Over the years, he have given me a freedom to try out a number of ideas, even something that was unrelated to my own thesis. I will not forget all the advice, guidance, encouragement and friendship I have received.

My sincere gratitude goes to members of my Supervisory Committee, Dr.Gary Leach and Dr.Melanie O'Neill for the helpful discussions and constructive suggestions. I believe their critical views have strengthened me as a scientist. I can not thank them more for taking time out of their busy schedule whenever I needed help. I would like to thank Dr. Vance Williams for being the internal examiner, and Professor Richard McCreery for taking his time to attend my defence.

A part of my research was conducted in Hokkaido University under the guidance of Professor Kohei Uosaki and Dr. Hidenori Noguchi. I am grateful for the opportunity

Professor Uosaki provided me. I would like to thank Dr. Hidenori Noguchi for his guidance and support, Mr. Takanobu Yano and Dr. Mikio Ito for help with SFG experiments. Without their help this thesis has not been possible.

I would like to express my gratitude to Dr. Eberhard Kiehlmann for proof-reading all the publications and this thesis. I thank Cassie and Jusroop for the advice and help with the thesis; Cassie, thanks for all the reminders and notes!!! I probably have missed tons of must-do activities without you. All my appreciations go to friends and colleagues whom supported me throughout the graduate studies. Andy, Alan, Bananai, Bixia, Dinah, Corey, Debo, Emily, Erin, Jeff, Lily (× 2), Dr.Liu, Marcus, Navanita, Richard, Shi, and Zheng, I had a great time hanging out with you guys.

I thank Chiyoko, Bob, Emily, Tami, Hisako, Yo, BJ and Michelle for all the advices, festives and their support! And the little one that yet to see light, thanks for bringing joys to our family. I appreciate the presence of all of my brothers (in alphabetical order); Angelo, Genna, Neil, Rob, and Seth. You guys are awesome and will always be my family.

Table of Contents

List of Figures

List of Tables

Glossary

ν_{as}	Asymmetric stretch
ϕ_b	Barrier height
ϕ_{eff}	Effective barrier height
ν_s	Symmetric stretch
$\langle \beta_{i,j,k} \rangle$	Average orientational distribution of molecular hyperpolarizability tensor
$\tilde{N}$	Complex index of refraction
ε_0	Dielectric constant in vacuum
$\chi^{(n)}$	Electrical susceptibility of n^{th} order
$\vec{E}$	Electric field
$\vec{P}$	Polarization field
$\hat{e}$	Unit electric vector
A	Amplitude
Å	Angstrom
A*	Richardson constant
A_{electr}	Surface area of electrode
A-F	Constants used for Cauchy's adsorbent dispersion formula
AFM	Atomic force microscopy
ATR-IR	Attenuated Total Reflectance Infrared
c	Speed of light in vacuum

C	Differential capacitance
d^-	Asymmetric methylene stretch
d^+	Symmetric methylene stretch
DFG	Difference frequency generation
DNA	deoxyribonucleic acid
d_p	Penetration depth
E_B	Binding energy
EDC	1-ethyl-3-[3-dimethylaminopropyl]-carboiimide hydrochloride
EDC	1-ethyl-3-(3-dimethylaminopropyl)-carbodiimide hydrochloride
E_{kin}	Kinetic energy
Et-UD	Ethyl 10-undecenoate
eV	Electron volt
F	Fresnel factor
F_c	Faraday constant
FR	Fermi resonance
ħ	Planck's constant
HEPES	4-(2-hydroxyethyl)-1-piperazineethanesulfonic acid
HREELS	High-resolution electron energy loss spectroscopy
H-Si	Hydrogen-terminated silicon
i, j, k	Cartesian coordinates in the laboratory reference
I_s, I_c	The first and second order harmonic of the reflected light
I_{SFG}	SFG signal intensity

J	Current density
k	Extinction coefficient
k	Boltzmann constant
M	Number of nucleotides per DNA
M	Molecular weight
MCT	Mercury cadmium telluride
Me-UD	10-undecenoate
n	Number of electrons involved in the reation
n	Ideality factor
n’	Refractive index of the interfacial layer
N_d	Doping density
NHS	N-hydroxysuccinimide
NHS	N-hydroxysuccinimide
NR	Non-resonance
N_s	Number of interfacial molecules
n_x	Index of refraction of medium x
OPA	Optical parametric amplification
OPG	Optical parametric generation
OTS	Octadecyltrichlorosilane
PMT	Photomultiplier tube
Pr-UD	Propyl 10-undecenoate
Q	charge

q	Electronic charge
$q\phi_{metal}$	Work function of metal
$q\chi$	Electron affinity of semiconductor
r	Position vector
r^-	Asymmetric methyl stretch
r^+	Symmetric methyl stretch
R_p	Total reflection coefficient for the p component
R_s	Total reflection coefficient for the s component
r_{xy}	Fresnel reflection coefficient between medium x and y
SFG	Sum-frequency generation
SHG	Second-harmonic generation
t	Time
T	Absolute temperature
TDBA-OSu	4”-[3-Trifluoromethyl-3H-diazirin-3-yl] benzoic acid N-hydroxysuccinimide ester
TEMPO	2,2,6,6-tetramethylpiperidinooxy
THF	Tetrahydrofuran
UV	Ultraviolet
V	Applied bias voltage
V_{D0}	Built-in potential
V_{fb}	Flatband potential
XPS	X-ray photoelectron spectroscopy
z	Charge of cation

α	polarizability
β	Phase shift of the electromagnetic wave
β_{tun}	Electron-tunnelling constant
γ	Surface tension
Γ	damping constant width
Γ_{DNA}	Surface Density of DNA
Γ_{Ru}	Surface Density of ruthenium hexamine
Δ	Relative phase change
ε_0	Permittivity of free space
θ	Angle
θ_c	Critical angle
λ	Wavelength
P	Molecular density
Φ	Work function
ψ	Relative amplitude change
ω	Frequency
β	Hyperpolarizability

Chapter 1. General Introduction

Since the illustrious discovery of the double helical structure of DNA (deoxyribonucleic acid) molecules by Watson and Crick in 1953,[1] the advancement of molecular biology and biochemistry has been immense. This was followed by the important development of sequencing techniques which revealed the genetic codes in 1977,[2] and the successful modification of DNA with fluorescent molecular labels in 1986.[3] Together with the polymerase chain reaction (PCR), a technique that amplifies DNA concentrations,[4] these findings became instrumental to the development of DNA microarrays ("gene chips").

The concept of DNA microarrays was demonstrated on filter papers with arrays of spotted probe DNA used to identify proliferation-related complementary DNA.[5] This idea was extended to the miniaturization and multiplication of DNA hybridization assays on a glass substrate in 1995.[6] With the advancement of fabrication techniques for microscale devices, a number of DNA microarrays, typically prepared on glass, quartz, silicon chip or microscopic beads, are in development or have become commercially available. Despite this success, several specific challenges remain. For example, statistical significance is often unachievable because the lack of standardization in sample preparation, analysis methods and handling procedures make it impossible to compare data obtained in different experiments and biochips. These difficulties arise mainly because of our limited understanding of the behaviour and property of biological macromolecules immobilized on solid surfaces.

In order to deepen our understanding of the behaviour of biomolecules tethered to a solid surface, the work embodied in this dissertation explores the preparation methods as well as the structure and function of DNA monolayers immobilized on silicon. In the following sections, the literature pertained to the preparation of organic monolayers (both n-alkyl and ω-functionalized) and the immobilization of DNA oligonucleotide strands on oxide-free silicon will be described. As noted below, the direct attachment of functional organic molecules on hydrogen-terminated silicon (≡Si-H) have great implications for the fabrication of biochips and for molecular bioelectronics in general.[8]

1.1 Si-C bonded monolayers on silicon

In 1993, Linford and Chidsey *et al.* reported the first example of a highly compact Si-C bonded alkyl monolayer on a silicon surface. It was prepared by reacting 1-alkenes with hydrogen-terminated Si (111) in the presence of diacyl peroxides.[7,9] The radical reaction is initiated by homolytic cleavage of the diacyl peroxide:

$$[RC(O)O]_2 \rightarrow 2\ RC(O)O\bullet$$

The acyloxy radical breaks apart to from an alkyl radical and carbon dioxide:

$$RC(O)O\bullet \rightarrow R\bullet + CO_2$$

Then the alkyl radical extracts a hydrogen atom from ≡Si-H:

$$R\bullet + Si\text{-}H \rightarrow HR + Si\bullet$$

The resulting silicon free radical adds to the 1-alkene:

$$Si\bullet + CH_2{=}CH\text{-}R \rightarrow Si\text{-}CH_2(CH\bullet)\text{-}R$$

Subsequently, the secondary carbon radical abstracts hydrogen atom from a nearby Si-H or from an unreacted olefin:

$$Si\text{-}CH_2(CH\bullet)\text{-}R + CH_2{=}CH\text{-}CH_2\text{-}R' \rightarrow Si\text{-}(CH_2)_2\text{-}R + CH_2{=}CH\text{-}(CH\bullet)\text{-}R' \text{ or}$$

$$Si\text{-}CH_2(CH\bullet)\text{-}R + Si\text{-}H \rightarrow Si\text{-}(CH_2)_2\text{-}R + Si\bullet$$

This initiates a chain reaction and leads to the formation of an alkyl monolayer that has approximately 50% of the surface coverage.[9,10] Another initiator used for a similar scheme was 2,2,6,6-tetramethylpiperidinooxy (TEMPO).[11]

Thereafter, many other methods that do not require radical initiators have been discovered: Si-C bonded alkyl monolayers on silicon can be prepared thermally,[7,9,10] photochemically,[12-14] or electrochemically.[15-17] They can also be prepared via the reaction of Grignard reagents and organolithium complexes with chlorine- or hydrogen-terminated silicon.[18-22] A rather surprising result was the reaction of alkenes with ≡Si-H via irradiation with visible light in the range of 447-658 nm.[23,24] This is well above the wavelength required for homolytic cleavage of Si-H bonds that requires 3.5 eV ($\lambda < 350$ nm). Thus the reaction mechanisms underlying these processes differ depending on the conditions.

Thermal and photochemical ($\lambda < 350$ nm) reactions most likely proceed by the free radical mechanism akin to the reaction initiated by diacyl peroxides as mentioned above.[11,12] Here, thermal energy or UV-light cleaves the Si-H bond, leaving a silicon radical. Incoming olefin reacts with the "dangling bond" and forms a secondary carbon radical that subsequently abstracts a nearby hydrogen to produce another silicon radical (Figure 1.1). The process will propagate until the formation of a complete monolayer.

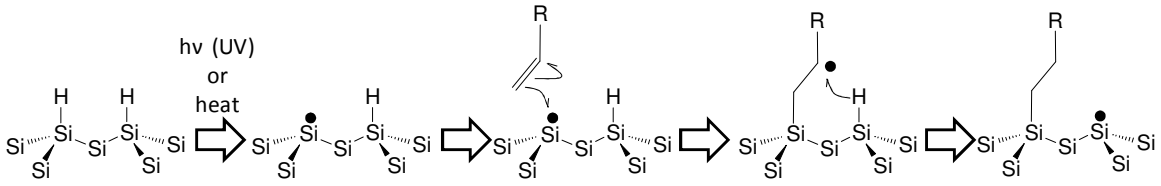

Figure 1.1 Photo- or thermal-initiated free radical mechanism for the attachment of unsaturated hydrocarbon.

The outcome of an electrochemical attachment of alkynes to porous silicon varies depending on the polarity of the applied potential bias. The alkynes are directly attached to the surface upon cathodic electrografting (Figure 1.2 a), whereas an alkyl bridge will form during anodic electrografting (Figure 1.2 b). Based on their experimental results, Robins *et al.* have proposed two mechanisms.[15] In the case of cathodic electrografting, a silyl anion is suggested to be the intermediate formed by surface reduction of ≡Si-H. Then deprotonation of the alkyne mediated by the silyl anion generates a carbanion. A weakly acidic alkyne will subsequently attack the Si-Si bond leading to the direct attachment (Figure 1.2 a). Anodic electrografting is proposed to occur by the formation of an active cationic silyl group where the depletion layer at the semiconductor / electrolyte interface stabilizes the charge. Such a cationic silyl group will be susceptible to attack by alkyne, and the successive hydrosilation reaction generates a bridged alkyl group (Figure 1.2 b). Wang and Buriak have also demonstrated electrochemical additions of organic monolayers on both porous and crystalline silicon (111) using alkylammonium and alkylphosphonium cations. Similar to the reaction pathway for cathodic electrografting of alkyne, the involvement of silyl anions was suggested.[16]

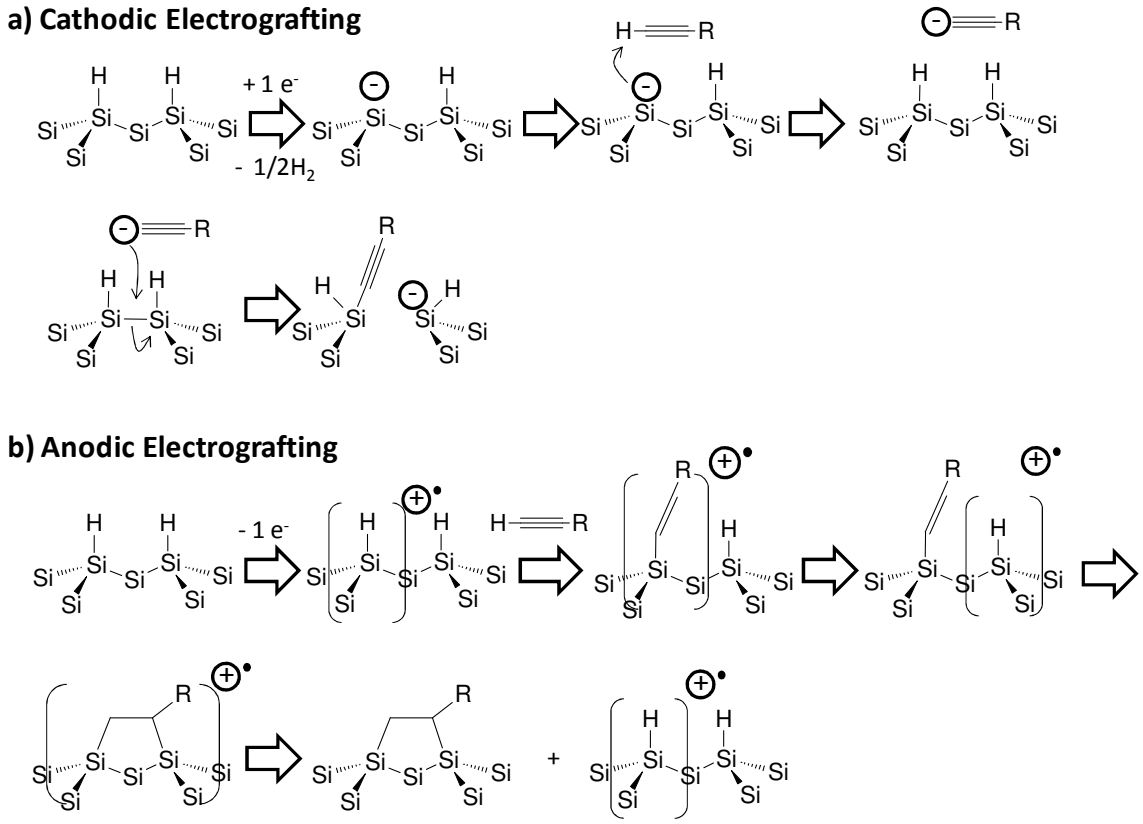

Figure 1.2 Proposed reaction paths for a) cathodic and b) anodic electrografting.

One of the most unusual reaction mechanisms involving addition of alkenes to a flat crystalline silicon surface was reported by Sun *et al.*[23, 24] The basis of the proposition is the activation of the reaction by visible light (447-658 nm). At this energy, the homolysis of Si-H bond is not possible since a wavelength of shorter than 350 nm is required. This led the authors to the hypothesis of an electron/hole pair mechanism; a surface-localized hole created by the light absorption will interact with an 1-alkene to form a silylated β-carbocation followed by the extraction of a hydrogen atom from an adjacent Si-H (Figure 1.3). In fact, Stewart and Buriak proposed a similar exciton-

mediated pathway to explain the hydrosilylation of photoluminescent nanocrystalline porous silicon using 400 nm light.[14] This was suggested to be limited to porous silicon in which quantum confinement effects are pronounced. Nevertheless, these extremely mild conditions may be advantageous by allowing direct attachment of UV-sensitive or fragile molecules to crystalline silicon.[25]

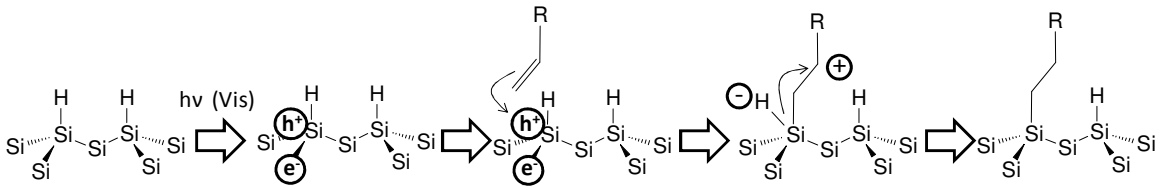

Figure 1.3 Electron/hole pair mechanism for hydrosilylation induced by visible light.

As summarized above, several methods are available to prepare Si-C grafted organic monolayers on oxide-free silicon. Although the reaction mechanisms are still unclear, all the resulting monolayers are chemically robust and stable over long periods of time; for example, organically modified silicon surfaces can survive 40% HF, boiling chloroform, boiling acidic and basic solutions, and are structurally stable for a month.[7, 9, 17, 26, 27] In practice, the preferred preparative procedure depends on the conditions and, in some cases, the desired monolayer structure. In the work presented in this dissertation, photochemical and thermal reactions have been adopted mainly because of their relatively simple reaction procedures.

1.2 Preparation of ω –functionalized monolayers on silicon

While an alkyl monolayer is an excellent passivation layer and provides a stable surface,[26,27] the limited reactivity of saturated hydrocarbons makes further molecular manipulation difficult. Subsequent derivatization of a molecular monolayer, however, is critical to control the interfacial properties as well as to incorporate macromolecules such as DNA strands and proteins.

One of the earliest examples of chemical manipulation of organic monolayers was the modification of the terminal methyl groups.[28] One of the two routes explored was the insertion of a photoactivatable aryldiazirine crosslinker TDBA-OSu (4"-[3-trifluoromethyl-3H-diazirin-3-yl] benzoic acid N-hydroxysuccinimide ester) in the methyl C-H bonds through a highly reactive singlet-state carbene intermediate. The other route was the formation of an amino-terminated sulphonamide via amination of a chlorosulfonated alkyl group. Surfaces tethered with macromolecules were prepared from the two derivatives. These methods, however, are difficult to control; in the case of the route involving a carbene intermediate, the reaction was inefficient and the surface conversion ratio was limited to approximately 10%.[28]

Two independent groups illustrated an approach to use a protected ω-functionalized monolayer for subsequent derivatization on silicon surfaces.[29, 30] Sieval et al. prepared a hydroxy- or carboxy-modified surface from an ester-terminated monolayer on silicon (100).[29] The latter was prepared by reacting ≡Si-H with bifunctional molecules possessing an alkene and an ester group at the two ends. A carboxy is the product of acid-catalyzed hydrolysis of the ester group whereas hydride reduction leads to a primary alcohol terminal group (Figure 1.4). In this case, ester groups are required as protecting

groups since alcohols and aldehydes would form Si(111)-OR by reacting with a hydrogen-terminated surface.[31-33]

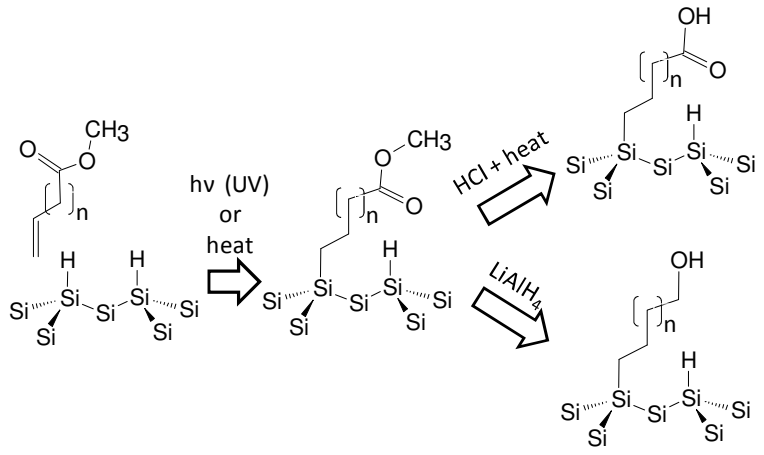

Figure 1.4 An alcohol and a carboxy terminated surface prepared by hydrolysis and reduction reaction of methyl ester monolayer.

Boukherroub and Wayner adopted a similar strategy and reported additional schemes to derivatize ester-terminated monolayers on silicon (111). An ethyl ester group was transformed into a primary alcohol by reduction with $NaBH_4$, to a tertiary alcohol using a Grignard reagent, or to a carboxy group via hydrolysis.[30] More importantly, they explored multistep modifications of the monolayers: the primary and tertiary alcohols were esterified by reaction with acetyl chloride, and the carboxy- terminated silicon surface was coupled with glycine methyl ester through the formation of an amide bond using carbodiimide. These pioneering studies opened up new routes to prepare surfaces with various functionalities.[34- 36]

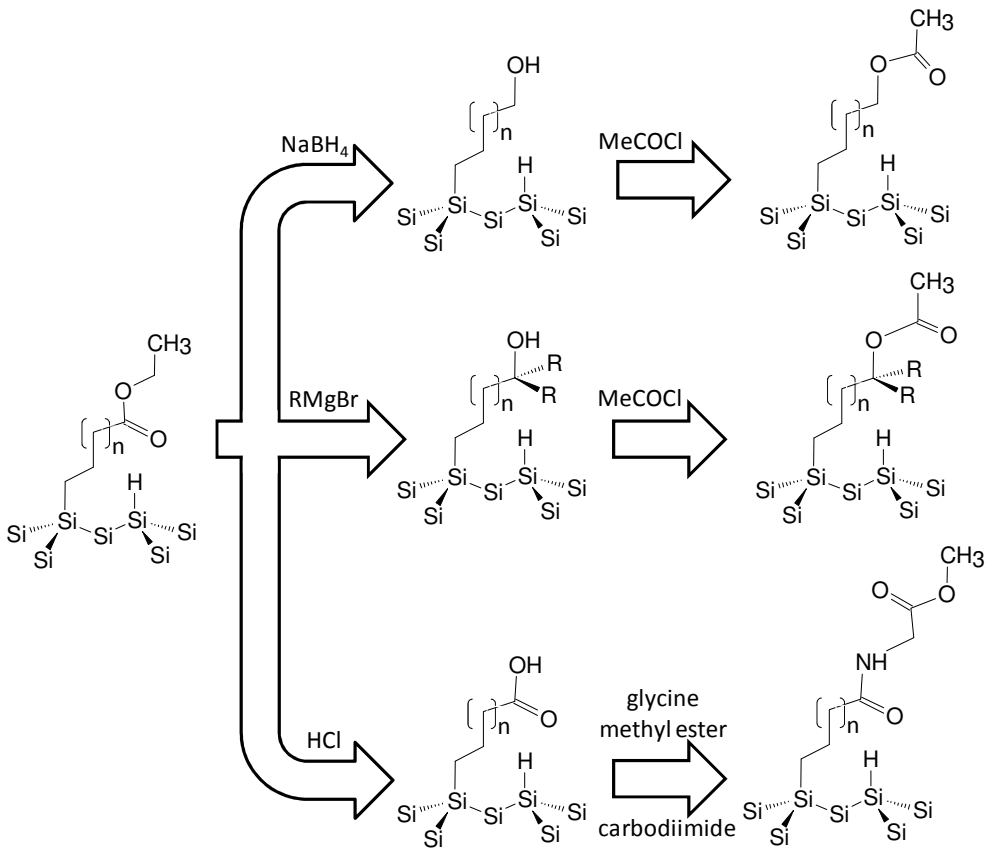

Figure 1.5 Multistep modification of ethyl ester terminated monolayer on crystalline silicon.

1.3 Preparation of DNA monolayers on silicon

The conventional biological macromolecules attachment to glass or oxidized silicon surfaces is often irreproducible as the number of hydroxyl groups depends on the degree of oxidation and hence the past history of the sample (i.e., how the sample was stored). Therefore, atomically flat and structurally well-defined silicon surfaces are of great interest as platforms for biochips. There is also an opportunity to take advantage of the electronic properties of semiconductors to fabricate DNA-based molecular electronic devices.

Strother et al. used a carboxy-terminated monolayer on silicon that was prepared according to the scheme shown in Figure 1.5, to first electrostatically bind a layer of polylysine. Subsequently, thiol-modified DNA strands were immobilized through the heterobifunctional cross-linker sulfosuccinimidyl 4-(N-maleimidomethyl)-cyclohexane-1-carboxylate, which was bound to the top of polylysine layer via amide bonds (Figure 1.6a).[37] Such a system may not be feasible for electrochemical characterization as the electrode potential will significantly influence the electrostatic interaction between polylysine and the cross-linker molecules. These authors used the same cross-linker molecules on an amino-terminated silicon surface to immobilize DNA strands via covalent bonds (Figure 1.6b). The amino-terminated monolayer was prepared by the hydrolysis of t-Boc-protected 10-aminodec-1-ene.[38, 39]

A more direct, two-layer system has been explored where the ω-carboxylic acid monolayer is converted to an N-hydroxysuccinimide ester (NHS ester) by treatment with NHS and 1-ethyl-3-[3-dimethylaminopropyl]-carboiimide hydrochloride (EDC). Then the amino-terminated DNA is coupled to the surface via amide formation. Using this protocol, micron and submicron DNA microarrays have been prepared.[39- 41] Yet another interesting method is an on-chip synthesis in which a DNA synthesizer was used to construct the DNA strand on an ω-alcohol monolayer.[42]

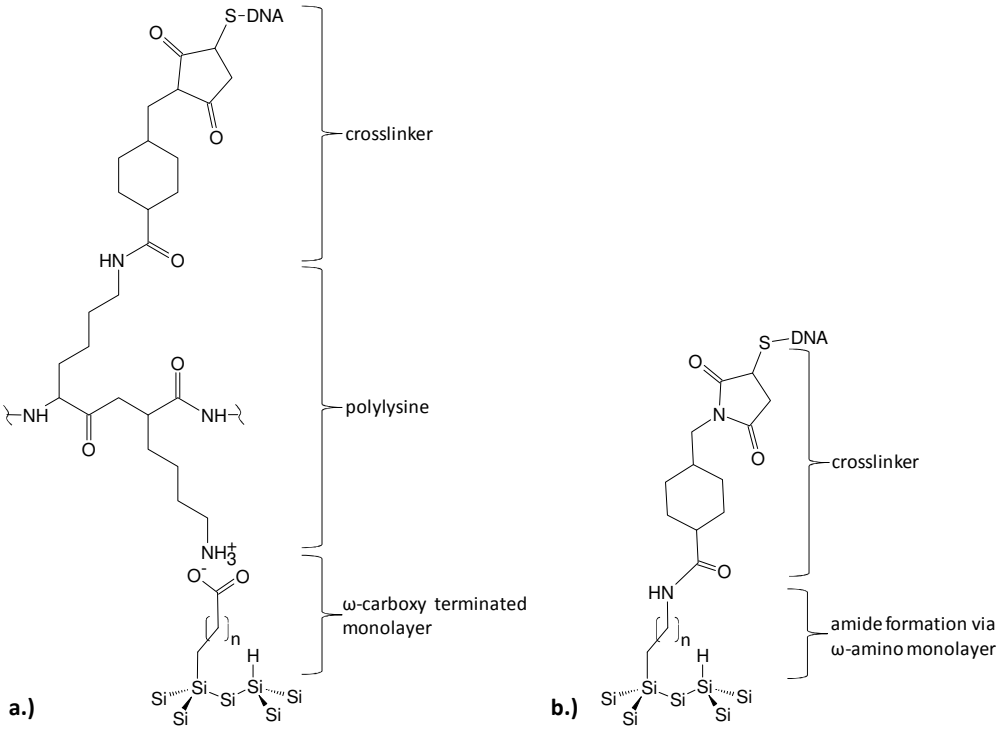

Figure 1.6 DNA attached to Si(111) surface via cross-linker through a.) electrostatic interaction between protonated amine and carboxlic acid or b.) amide formation.

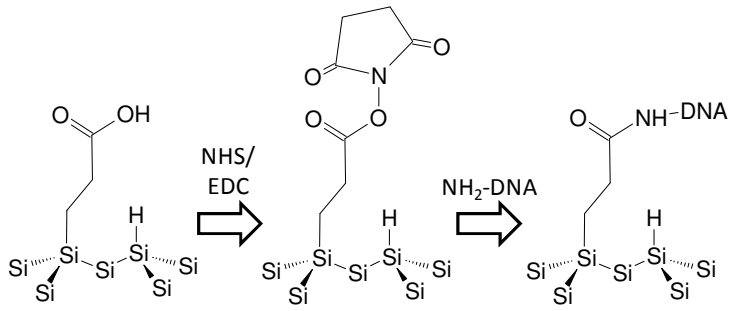

Figure 1.7 DNA monolayer is prepared on Si(111) surface via amide formation between amine terminated DNA and NHS ester.

Several independent groups have assessed the performance (i.e., DNA hybridization efficiency) of DNA monolayers on silicon. The binding of complementary target DNA is typically monitored either by the change in fluorescent signal or by electrical/electrochemical responses. The fluorescence method relies on the hybridization of fluorophore-tagged target DNA,[37, 38, 40, 41] whereas the electrical response depends directly on the interfacial charges.[39] The binding of charged molecules can be probed by monitoring the space-charge layer of the interface via differential capacitance measurements.

1.4 Objectives of this dissertation

The above-mentioned pioneering studies have established methods to prepare and characterise Si-C bonded organic monolayers on crystalline silicon surfaces. As elaborated, this has been extended to the preparation of DNA monolayers on silicon.

The objective of the research described in this thesis was to improve our fundamental understanding of semiconductor-based biochips, their fabrication and structural characterization. First, the preparation method of bioreactive ω-carboxy monolayers on silicon is assessed, by which a new route to prepare bioreactive surfaces is proposed. This is followed by the structural evaluation of DNA monolayers under different saline conditions. The last part of the thesis is devoted to the exploration of solid-state electrical characterization methods of alkyl/DNA monolayers on silicon.

The flow chart on the following page (Figure 1.8) represents the overall scheme of my thesis research. It can be broadly divided into two sections: the first is related to the

chemistry involved in the bioreactive surface preparation (chapter 3-5). The ester hydrolysis is a seminal step for the preparation of carboxy-terminated monolayers however, the influence of the reaction on the monolayers was not well understood. A conventional method for the acid-catalyzed hydrolysis of ester-terminated monolayers has been explored (chapter 3). Based on the findings of chapter 3, a more direct route to carboxy-terminated monolayers on silicon was developed that eliminated the hydrolysis step (chapter 4). This method was used to prepare DNA monolayers on silicon and to explore the influence of cations on the immobilization of DNA strands on silicon and subsequent hybridization with complementary DNA (chapter 5).

With an ultimate goal of understanding the electric properties of DNA, the second portion of the dissertation focuses on the electrical characterization (Chapter 6-8) of organic monolayers on silicon. Such an investigation requires a stable and reliable electric contact which preserves the "molecular fingerprints" of organic/bio- molecules (i.e., without damaging the biomolecules). The studies elaborated in Chapter 6 assess the feasibility of conventional methods such as thermal deposition and sputtering for metal deposition on organic monolayer systems. The findings were the basis for the construction of a device for solid-state electrical measurements of "soft" materials; the device consists of a custom-made micromanipulator and a gas-tight syringe to hold a mercury drop (Chapter 7). The performance of the device is demonstrated and reveals the "molecular characteristics" of ω-functionalized monolayer systems (Chapter 8). The preliminary result for the electrical characterization of DNA monolayers on silicon was reported.

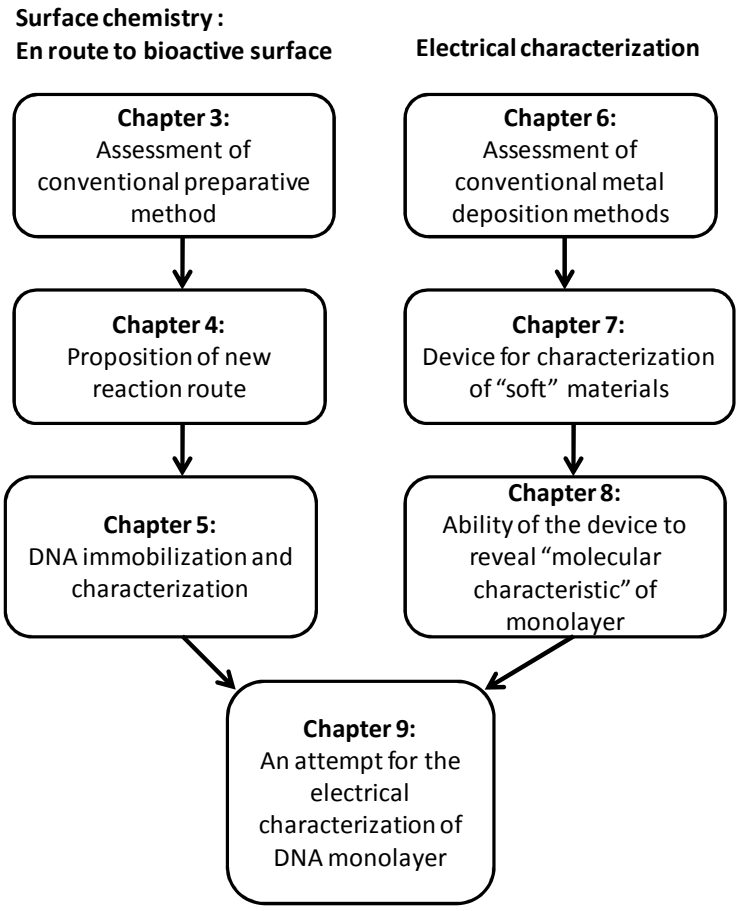

Figure 1.8 Flowchart of the dissertation: It indicates the theme of each chapter.

1.5 Bibliography

(1) Watson, J.D.; Crick, F.H.C. *Nature* **1953**, *171*, 737.

(2) Sanger, F.; Nicklen, S.; Coulson, A. R. *Proc. Nat. Acad. Sci.* **1977**, *74*, 5463.

(3) Maxam, A. M.; Gilbert, W. *Proc. Nat. Acad. Sci.* **1977**, *74*, 560.

(4) Saiki, R.K.; Scharf, S.; Faloona, F.; Mullis, K. B.; Horn, G. T.; Erlich, H. A.; Arnheim, N. *Science* **1985**, *230*, 1350.

(5) Kulesh, D. A.; Clive, D. R.; Zarlenga, D. S.; Greene, J. *J. Proc. Natl. Acad. Sci.* **1987**, *84*, 8453.

(6) Schena, M.; Shalon, D.; Davis, R. W.; Brown, P. O. *Science* **1995**, *270*, 467.

(7) Linford, M. R.; Chidsey, C. E. D. *J. Am.Chem. Soc.* **1993**, *115*, 12631.

(8) Pike, A.; Horrocks, B.; Connolly, B.; Houlton, A. *Aust. J. Chem.* **2002**, *55*, 191.

(9) Linford. M. R.; Fenter, P.; Eisenberger, P. M.; Chidsey, C. E. D. *J. Am. Chem. Soc.* **1995**, *117*, 3145.

(10) Sieval, A. B.; Demirel, A. L.; Nissink, J. W. M.; Linford, M. R.; van der Maas, J. H.; de Jeu, W. H.; Zuilhof, H.; Sudhölter, E. J. R. *Langmuir* **1998**, *14*, 1759.

(11) Perring, M.; Dutta, S.; Arafat, S.; Mitchell, M.; Kenis, P. J. A.; Bowden, N. B. *Langmuir* **2005**, *21*, 10537.

(12) Effenberger, F.; Gotz, G.; Bidlingmaier, B.; Wezstein, M. *Angew Chem. Int. Ed.* **1998**, *37*, 2462.

(13) Cicero, R. L.; Linford, M. R.; Chidsey, C. E. D. *Langmuir* **2000**, *16*, 5688.

(14) Stewart, M. P.; Buriak, J. M. *J. Am. Chem. Soc.* **2001**, *123*, 7821.

(15) Robins, E. G.; Stewart, M. P.; Buriak, J. M. *Chem. Comm.* **1999**, 2479.

(16) Wang, D.; Buriak, J. M. *Surf. Sci.* **2005**, *590*, 154.

(17) de Villeneuve, C. H.; Pinson, J.; Bernard, M. C.; Allongue, P. *J. Phys. Chem. B* **1997**, *101*, 2415.

(18) Bansal, A.; Li, X. L.; Lauermann, I.; Lewis, N. S.; Yi, S. I.; Weinberg, W. H. *J. Am. Chem. Soc.* **1996**, *118*, 7225.

(19) Terry, J.; Linford, M. R.; Wigren, C.; Cao, R.; Pianetta, P.; Chidsey, C. E. D. *Appl. Phys. Lett.* **1997**, *71*, 1056.

(20) Bansal, A.; Lewis, N. S. *J. Phys. Chem. B* **1998**, *102*, 1067.

(21) Song, J. H.; Sailor, M. J. *J. Am. Chem. Soc.* **1998**, *120*, 2376.

(22) Kim, N. Y.; Laibinis, P. E. *J. Am. Chem. Soc.* **1999**, *121*, 7162.

(23) Sun, Q. Y.; de Smet, L. C. P. M.; van Lagen, B.; Wright, A.; Zuilhof, H.; Sudhölter, E. J. R. *Angew. Chem. Int. Ed.* **2004**, *43*, 1352.

(24) Sun, Q.Y.; de Smet, L. C. P. M.; van Lagen, B.; Giesbers, M.; Thüne, P C.; van Engelenburg, J.; de Wolf, F. A.; Zuilhof, H.; Sudhölter, E. J. R. *J. Am. Chem. Soc.* **2005**, *127*, 2514.

(25) De Smet, L. C. P. M.; Stork, G. A.; Hurenkamp, G. H. F.; Sun, Q. Y.; Topal, H.; Vronen, P. J. E.; Sieval, A. B.; Wright, A.; Visser, G.; Zuilhof, H.; Sudhölter, E. J. R. *J. Am .Chem. Soc.* **2003**, *125*, 13916.

(26) Gorostiza, P.; de Villeneuve, C. H.; Sun, Q. Y.; Sanz, F.; Wallart, X.; Boukherroub, R.; Allongue, P. *J. Phys. Chem. B* **2006**, *110*, 5576.

(27) Royea, W. J.; Juang, A.; Lewis, N. S. *Appl. Phys. Lett.* **2000**, *77*, 1988.

(28) Wagner, P.; Nock, S.; Spudich, J. A.; Volkmuth, W. D.; Chu, S.; Cicero, R. L.; Wade, C. P.; Linford, M. R.; Chidsey, C. E. D. *J. Struct. Biol.* **1997**, *119*, 189.

(29) Sieval, A. B.; Demirel, A. L.; Nissink, J. W. M.; Linford, M. R.; van der Maas, J. H.; de Jeu, W. H.; Zuilhof, H.; Sudhölter, E. J. R. *Langmuir* **1998**, *14*, 1759.

(30) Boukherroub, R.; Wayner, D. D. M. *J. Am Chem. Soc.* **1999**, *11*, 11513.

(31) Cleland, G.; Horrocks, B. R.; Houlton, A. J. *Chem. Soc. Faraday Trans.* **1995**, *91*, 4001.

(32) Effenberger, F.; Götz, G.; Bidlingmaier, B.; Wezstein, M. *Angew. Chem. Int. Ed.* **1998**, *37*, 2462.

(33) Boukherroub, R.; Morin, S.; Sharpe, P.; Wayner, D. D. M. *Langmuir* **2000**, *16*, 7429.

(34) Wayner, D. D. M.; Wolkow, R. A. J. *Chem. Soc. Perkin Trans.* **2002**, *2*, 23.

(35) Buriak, J. M. *Chem. Rev.* **2002**, *102*, 1271.

(36) Boukherroub, R. *Curr. Opin. Solid State Mater. Sci.* **2005**, *9*, 66.

(37) Strother, T.; Cai, W.; Zhao, X.; Hamers, R. J.; Smith, L. M. *J. Am Chem. Soc.* **2000**, *122*, 1205.

(38) Strother, T.; Hamers, R. J.; Smith, L. M. *Nucleic Acids Res.* **2000**, *28*, 3535.

(39) Cai, W.; Peck, J. R.; van der Weide, D. W.; Hamers, R. J. *Biosens. Bioelectron.* **2004**, *19*, 1013.

(40) Yin, H. B.; Brown, T.; Greef, R.; Wilkinson, J. S.; Melvin, T. *Microelectron. Eng.* **2004**, *73*, 830.

(41) Voicu, R.; Boukherroub, R.; Bartzoka, V.; Ward, T.; Wojtyk, J. T. C.; Wayner, D. D. M. *Langmuir* **2004**, *20*, 11713.

(42) Pike, A. R.; Lie, L. H.; Eagling, R. A.; Ryder, L. C.; Patole, S. N.; Connolly, B. A.; Horrocks, B. R.; Houlton, A. *Angew. Chem. Int. Ed.* **2002**, *41*, 615.

Chapter 2. Experimental techniques

This chapter is a brief introduction to the experimental techniques that have been used in the research described in this thesis. Herein, I will focus on the analytical aspects (i.e., the application) of an individual technique, in particular how it was used to characterize the monolayer systems. More detailed theoretical descriptions are available in the literatures (see 2.7 Bibliography).

2.1 Ellipsometry

Although the name "Ellipsometry" was not used until 1945,[1] its fundamental concept was first reported more than a century ago.[2, 3] The basic idea of ellipsometry is to monitor the changes in polarization of light upon reflection from a solid sample.

The polarization of light is the orientation of the oscillations of electromagnetic waves; the waves that are in the plane of incidence are defined as "p" and those situated perpendicular to the plane are defined as "s" wave (Figure 2.1). The electric field vector may be represented by the combination of p and s waves. For instance, linearly polarized light where the oscillation occurs in a plane is described by the two components (s and p) that are in phase. When the two components are out of phase, resulting vector is no longer linear but the direction of the field rotates and traces an ellipse and is called

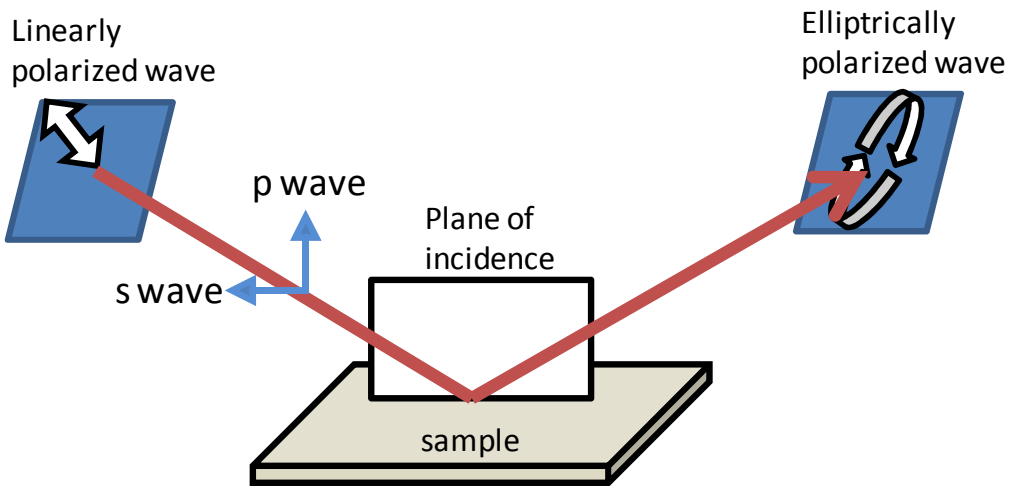

Figure 2.1 Reflection of a linearly polarized light beam from a sample.

elliptically polarized light except for the case where two components with the same amplitude is out of phase by 90°. In such case, circular polarization will be the result.

The technique of ellipsometry is based on the fact when linearly polarized light reflects off a surface, the phases of both p and s components shift. In general, the amplitude of phase shift differs between the two components and result in an elliptical polarization. This phenomenon depends on the optical properties and the thickness of the film on the substrate. In principle, one can deduce these properties from ellipsometric parameters ψ and Δ.

The parameters ψ and Δ quantify the polarization change of a light upon reflection. These parameters are expressed as

$$\tan \Psi \, e^{i\Delta} = \frac{R_p}{R_s} \tag{1}$$

where ψ is the relative change in amplitude and real part of the equation, Δ represents the relative phase change and imaginary part of the equation, R_p and R_s are the total reflection coefficients for the p and s component, respectively.[4, 5] The total reflection coefficients express the changes in amplitude and phase of the linear polarization component responding to the sample properties. For the system composed of air/film/substrate (Figure 2.2), R_s and R_p is formulated with the ratio of the amplitude of the reflected wave to that of incident wave [4, 5]

$$\mathbf{R_p} = \frac{\mathbf{r_{12}^p + r_{23}^p exp(-j\,2\beta)}}{\mathbf{1 + r_{12}^p\, r_{23}^p exp(-j\,2\beta)}} \qquad \mathbf{R_S} = \frac{\mathbf{r_{12}^S + r_{23}^S exp(-j\,2\beta)}}{\mathbf{1 + r_{12}^S\, r_{23}^S exp(-j\,2\beta)}} \tag{2}$$

where the superscript refers to p or s waves and the r is the Fresnel reflection coefficient of the interface between the subscripted numeric; "12" indicates the interface between medium 1 and 2. The Fresnel reflection coefficient is the ratio of the amplitude of the reflected wave to the amplitude of the incident wave for an interface:

$$\mathbf{r_{12}^p} = \frac{\mathbf{\tilde{N}_2\, cos\theta_1 - \tilde{N}_1\, cos\theta_2}}{\mathbf{\tilde{N}_2\, cos\theta_1 + \tilde{N}_1\, cos\theta_2}} \qquad \mathbf{r_{12}^s} = \frac{\mathbf{\tilde{N}_1\, cos\theta_1 - \tilde{N}_2\, cos\theta_2}}{\mathbf{\tilde{N}_1\, cos\theta_1 + \tilde{N}_2\, cos\theta_2}} \tag{3}$$

$\tilde{N}_x$ is the complex index of refraction of medium x. β in equation (1) describes phase shift of the electromagnetic wave upon travelling a distance within the film and is therefore related to the thickness d of the film (Figure 2.2): [4, 5]

$$\boldsymbol{\beta = 2\pi \left(\frac{d}{\lambda}\right) \tilde{N}_2 \cos \theta_2} \tag{4}$$

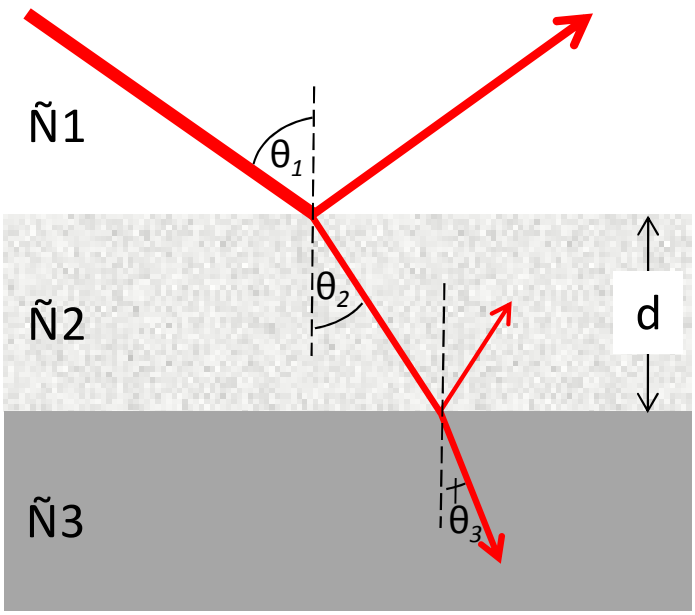

Figure 2.2 Reflection and refraction at the layered interfaces.

The complex index of refraction $\tilde{N}$ reflects the interaction of light with the material and is represented by a real and an imaginary part

$$\tilde{\mathbf{N}} = \boldsymbol{n} - \boldsymbol{jk} \tag{5}$$

where n is the index of refraction and k is the extinction coefficient. At the interface, Snell's law depicts the light refraction:

$$\tilde{\mathbf{N}}_1 \sin \boldsymbol{\theta}_1 = \tilde{\mathbf{N}}_2 \sin \boldsymbol{\theta}_2 \tag{6}$$

With dielectric material, only n is considered since a light is not absorbed and k = 0:

$$\mathbf{n}_1 \sin \boldsymbol{\theta}_1 = \mathbf{n}_2 \sin \boldsymbol{\theta}_2 \tag{7}$$

In a spectroscopic ellipsometer, the intensity of the reflected light is measured as the first and second order harmonics, I_s and I_c using the fast Fourier transform. These two parameters I_s and I_c are expressed in terms of ψ and Δ as

$$\mathbf{I_s = \sin 2\Psi \sin\Delta} \tag{8}$$

$$I_c = \sin 2\Psi \cos\Delta \tag{9}$$

The $\widetilde{N}$ and d of the film can be extracted by applying a model to the obtained ellipsometric values. In this thesis, a two-layer model where an organic film is on the crystalline silicon will be used to model the samples, where the top layer is simulated by Cauchy's adsorbent dispersion formula:

$$\mathbf{n(\lambda) = A + \frac{B}{\lambda^2} + \frac{C}{\lambda^4}} \tag{10}$$

$$k(\lambda) = D + \frac{E}{\lambda^2} + \frac{F}{\lambda^4} \tag{11}$$

The ellipsometry fitting method used in this thesis is described in Appendix I.

2.2 Attenuated Total Reflectance Infrared (ATR-IR)

ATR-IR spectroscopy is a surface sensitive method used to study thin films. In the ATR technique, an infrared beam is internally reflected in an ATR crystal (Figure 2.3). The total refection of electromagnetic wave occur at the interface when the angle of incidence is larger than the critical angle; θ_c, which is defined as

$$\theta_c = \sin^{-1} \frac{n_2}{n_1} \quad (1)$$

where n_1 is the refractive index of the crystal and n_2 is the refractive index of the sample positioned at the interface (Figure 2.3). It is clear from equation (1) that the n_1 must be greater than the n_2 in order to observe total reflectance. This is why ATR crystal is often made from a material with a high refractive index such as zinc selenide, silicon, germanium, or diamond.

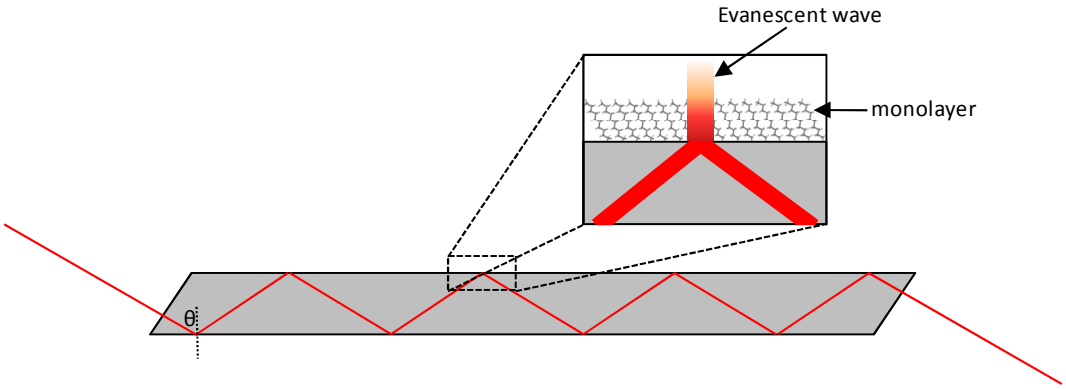

Figure 2.3 Schematic of the evanescent field at the surface of ATR.

The infrared light will be able to interact with the molecules positioned at the surface since an evanescent wave is produced upon internal reflection. In another words, the IR radiation extends beyond the surface boundary of the crystal although the effective penetration depth is less than the wavelength. The intensity of the evanescent wave decays exponentially with increased distance from the interface. The decay length or the penetration depth, d_p, of the evanescent wave is given by [6]

$$\mathbf{d_p = \frac{\lambda_1}{2\pi\sqrt{\sin^2\theta - \left(\frac{n_2}{n_1}\right)^2}}} \quad (2)$$

here θ is the angle of incident, and λ_1 is the wavelength in the ATR crystal and defined as $\lambda_1 = \lambda/n_1$. Equation (2) implies that the longer the wavelength, the larger d_p will be (i.e., the wave penetrates deeper at lower wavenumbers). The d_p is also greater at smaller θ as long as $\theta < \theta_c$.

Throughout this study, undoped silicon ATR crystals (n = 3.875) were used. The drawback of silicon ATR crystals is that the IR transmittance is significantly reduced at wavenumbers below 1500 cm^{-1} and therefore the fingerprint region (1200-600 cm^{-1}) of IR spectroscopy is not accessible. However, the higher sensitivity and the ability to directly prepare Si-C bonded organic monolayers on ATR crystals, as well as the availability of number of useful bands in the group frequency region (1500-3600 cm^{-1}) are particularly beneficial to the research carried in this thesis. The experimental setup with incident IR angle of θ = 45º, provides d_p in the range of 147-338 nm for the group frequency region.

2.3 X-ray Photoelectron Spectroscopy (XPS)

Photoelectron spectroscopy is based on the photoelectric effect that results from the irradiation of a substance with photons of sufficient excitation energy. The electronic structure of solid materials is analyzed with respect to the kinetic energy of the emitted electrons and the direction of propagation in angle-resolved photoemission. Ultraviolet photoelectron spectroscopy (UPS) uses UV to analyze the valence-band structure where XPS uses soft X-Rays to explore core-level electrons.

In order for the photoelectric effect to occur, the photons must possess enough energy to overcome the electron binding energy (E_B) and the work function (Φ). The excess energy will then turn into the kinetic energy (E_{kin}) and is expressed as [6]

$$\mathbf{E_{kin}} = \boldsymbol{h\nu} - \boldsymbol{E_B} - \mathbf{\Phi_{sp}} \quad \textbf{(1)}$$

here $h\nu$ represents the X-ray energy, and Φ_{sp} is the spectrometer work function. The spectrometer work function is used instead of the sample work function under the assumption that the sample and the spectrometer are in equilibrium (Figure 2.4). It is important to emphasize that the spectrometer work function is not the energy required for an electron to escape the spectrometer, but it is an instrumental term that off-sets all of the processes within the equipment such as the thermalization of the collected electrons. The spectrometer work function is determined through instrumental calibrations.

Since both $h\nu$ and Φ_{sp} are known, the electron binding energy can be estimated using the measured kinetic energy. The electron binding energy is unique to each element. In fact, XPS can identify all the elements except for hydrogen although the absolute quantification as in elemental analysis is challenging. This is because the electronic band structures are often too complex for a quantitative analysis.

A change in local chemical state induces rearrangement of the valance band and in turn influences the charge distribution surrounding the core-shell. The consequence is a deviation of the binding energy. The binding energy is therefore sensitive to the chemical environment of an atom. Such deviation is called chemical shift and useful for detecting various functional groups as well as oxidation states of the sample.

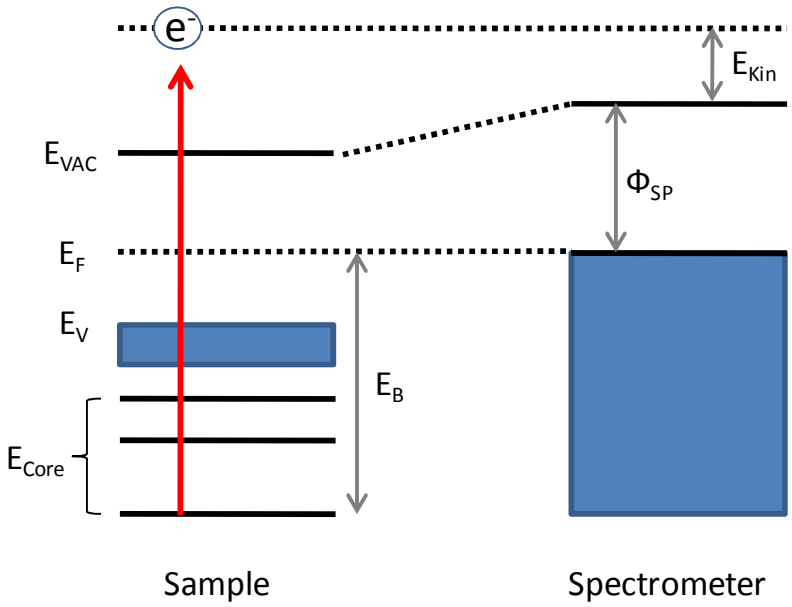

Figure 2.4 Schematic energy level diagram. Electron, e^-, was excited by $\boldsymbol{h\nu}$. E_{Core}, E_V and E_F represent core, valance, and Fermi level energy, respectively.

2.4 Atomic Force Microscopy (AFM)

The first AFM instrument was developed by Binning, Quante and Gerber in 1986 by modifying a STM microscope.[7] Today, the device exists as an essential high resolution imaging tool for surface science.

The basic setup of the AFM is shown in Figure 2.5. As the probe (tip) mounted at the end of a flexible cantilever scan over the sample in a raster pattern, the cantilever deflects or twists. Such movements alter the position of the laser reflecting off the cantilever; this change is monitored by the photodiode (quadrant position-sensitive photo detector). This signal can be used in a feedback loop to alter the z direction of the piezo

(scanner) to keep the force experienced by the cantilever constant. In turn, the movement of the piezo will be converted to a topographic image. Such a procedure is called the constant force mode. In the constant height mode, the height of the cantilever will be constant and the cantilever deflection monitored by the photodiode will be converted to a topographic image. Generally, constant-force mode is more widely used; however, when atomic-scale images of atomically flat surfaces or high scan speed are required the constant-height mode may be more advantageous. The above-mentioned methods are classified as contact AFM mode where the tip is in close proximity to the surface. The other more commonly used modes of operations are non-contact mode, where cantilever vibrates at its resonant frequency 50-150 Å above the surface, and tapping mode in which the cantilever also oscillates at its resonant frequency but the tip lightly touches or tap the surface. These two modes are not used in this thesis.

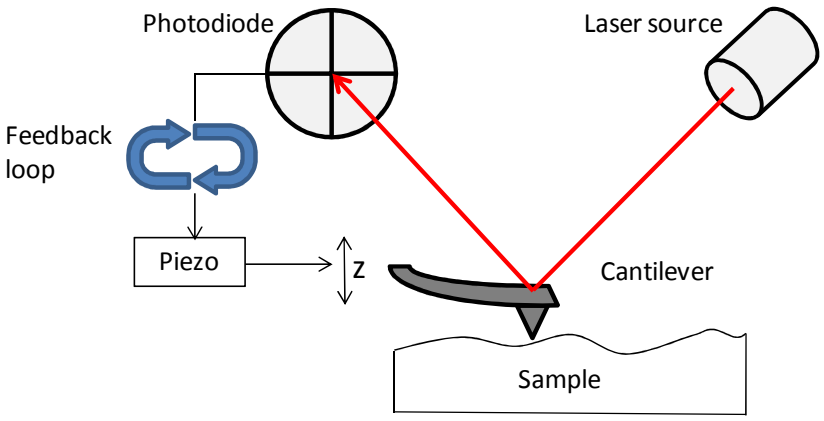

Figure 2.5 Schematic of basic AFM setup.

2.5 Contact angle measurement

The shape of a water droplet on a flat surface can be characterized by the contact angle, θ. It is described as the equilibrium between the interfacial tension vectors, the solid-vapour vector (γ_{sv}), the liquid-vapour vector (γ_{lv}), and the solid-liquid vector(γ_{sl}) as shown in Figure 2.6. The relationship between these forces and the contact angle is defined by Young's equation [8]

$$\boldsymbol{\gamma_{SV} = \gamma_{SL} + \gamma_{LV} \cos\theta} \qquad \textbf{(1)}$$

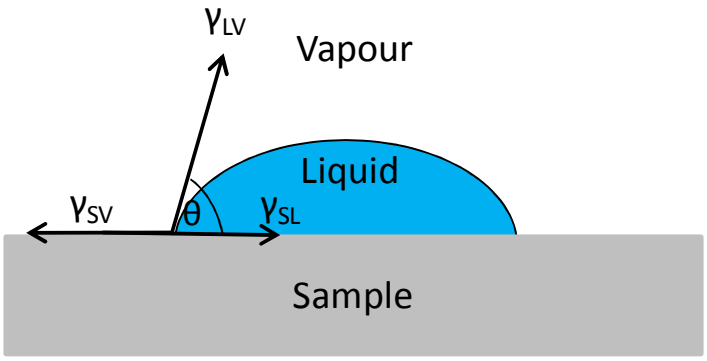

Figure 2.6 A droplet of water on a surface and its contact angle.

Although the contact angle is a macroscopic property, it is very useful for assessing the polarity of a surface and in certain cases it could be used to assess the quality of a monolayer. For instance, a high-quality n-alkyl monolayer on silicon will exhibit contact angles of greater than 105°.

2.6 Sum Frequency Generation Spectroscopy (SFG)

2.6.1 Second order nonlinear effect

Under exposure to a weak light source, the polarization field $\vec{P}$ of a material is linearly related to the electric field, $\vec{E}$

$$\vec{P} = \varepsilon_0 \chi^{(1)} \vec{E} \tag{1}$$

where ε_0 is dielectric constant in vacuum, and $\chi^{(1)}$ is the electrical susceptibility; a measure of how well the material responds to an electric field. This expression holds true until a strong electric field, such as a pulsed laser, is applied. In that case, the general expression for polarization must be considered [9]

$$\vec{P} = \varepsilon_0 \left(\chi^{(1)} \vec{E} + \chi^{(2)} \vec{E}\vec{E} + \chi^{(3)} \vec{E}\vec{E}\vec{E} + \cdots \right) \tag{2}$$

here the superscript represents n^{th} order susceptibility. It is clear from equation (2) that the non-linear terms contribute to the polarization. Since SFG is a second order non-linear process, the focus here will be on the second term of equation (2). As an example of a nonlinear process, consider interactions of two electric fields with frequencies ω_1 and ω_2 propagating in the direction of vector r at time t:

$$\vec{E}_1(r,t) = \vec{E}_1(r)\cos(\omega_1 t) \qquad \vec{E}_2(r,t) = \vec{E}_2(r)\cos(\omega_2 t) \tag{3}$$

The second order polarization of the material, given that $\chi^{(2)}$ is nonzero, is then expressed as [10]

$$\vec{P}^{(2)} = \varepsilon_0 \chi^{(2)} \vec{E}_1 \vec{E}_2$$

$$\vec{P}^{(2)} = \varepsilon_0 \chi^{(2)} \vec{E}_1(\mathbf{r})\cos(\omega_1 t)\vec{E}_2(\mathrm{r})\cos(\omega_2 t)$$

$$\vec{P}^{(2)} = \frac{1}{2}\varepsilon_0 \chi^{(2)} \vec{E}_1(\mathbf{r})\vec{E}_2(\mathbf{r})[\cos(\omega_1 + \omega_2)t + \cos(\omega_1 - \omega_2)t] \quad (4)$$

Equation (4) implies that the molecule excited by $\vec{E}_1$ and $\vec{E}_2$ possesses oscillating dipoles at $\omega_1 + \omega_2$ and $\omega_1 - \omega_2$ which will produce sum-frequency and difference-frequency generation. In the case where $\omega_1 = \omega_2$, equation (4) simplifies to

$$\vec{P}^{(2)} = \frac{1}{2}\varepsilon_0 \chi^{(2)} \vec{E}_1(\mathbf{r})\vec{E}_2(\mathbf{r})[1 + \cos(2\omega t)] \quad (5)$$

The term 2ωt represents the second-harmonic generation (SHG). The ability to change the frequency of the light is one of the unique effects of the non-linear terms in equation (2).

One of the important characteristics of $\chi^{(2)}$, the term which dictates the strength of second order optical effect, is the requirement for the media to be noncentrosymmetric. Indeed, this is the reason why the second-order non-linear effect is only active at the interface and is intrinsically sensitive to molecular groups without an inversion symmetry. For instance, consider a second-order polarization field in the material where inversion center is symmetric in all directions:

$$\vec{P}^{(2)} = \varepsilon_0 \chi^{(2)} \vec{E}^2 \quad (6)$$

Then the following relation must be valid in the media with an inversion center:

$$-\vec{P}^{(2)} = \varepsilon_0 \chi^{(2)}(-\vec{E})^2$$

$$-\vec{P}^{(2)} = \varepsilon_0 \chi^{(2)}(\vec{E})^2 \quad (7)$$

Equations (6) and (7) are only equivalent when $\chi^{(2)} = 0$. For this reason, all the even-ordered susceptibility terms in equation (2) are interface specific.

2.6.2 Sum frequency generation (SFG) process

The SFG process is induced by spatially overlapping two beams at a sample surface. In order to analyze the vibrational frequencies of surface species, typically visible (ω_{VIS}) and tunable infrared (ω_{IR}) beams are employed. One of the advantage of using ω_{VIS} and ω_{IR} is that the produced sum frequency is in the visible region and therefore can be readily amplified by a photomultiplier tube.

The intensity of SFG, I_{SFG}, is expressed as follow: [10]

$$I_{SFG} = \frac{8\pi^3 \omega_{SFG}{}^2 (\sec\theta_{SFG})^2}{c^3 n_1(\omega_{SFG}) n_1(\omega_{VIS}) n_1(\omega_{IR})} \left|\chi^{(2)}_{eff}\right|^2 I(\omega_{VIS}) I(\omega_{IR}) \quad (8)$$

where

$$\chi^{(2)}_{eff} = [\hat{e}(\omega_{SFG}) \cdot F(\omega_{SFG})] \cdot \chi^{(2)} : [\hat{e}(\omega_{VIS}) \cdot F(\omega_{VIS})] \cdot [\hat{e}(\omega_{IR}) \cdot F(\omega_{IR})] \quad (9)$$

Here θ_{SFG} is the angle of emission of SFG, c is the speed of light in vacuum, $n_1(\omega)$, $\hat{e}(\omega)$ and $F(\omega)$ are the index of refraction of medium 1, unit electric field vector and Fresnel factor at frequency ω, respectively.

The macroscopic second-order nonlinear susceptibility, $\chi^{(2)}$, is a third rank tensor with 27 individual elements and can be expressed in terms of Cartesian coordinates in the laboratory reference (i, j, and k):

$$\boldsymbol{\chi}^{(2)}_{i,j,k} = \boldsymbol{N_s} \langle \boldsymbol{\beta}^{(2)}_{i,j,k} \rangle \tag{10}$$

N_s is the number of interfacial molecules, $\langle \beta_{i,j,k} \rangle$ is the average orientational distribution of molecular hyperpolarizability tensor. When only electric dipole transitions are considered (i.e. ω_{VIS} or ω_{SFG} is not in resonance with an electronic transition of the material) β is described as [11]

$$\boldsymbol{\beta}^{(2)}_{i,j,k} = \frac{\mathbf{1}}{\mathbf{2}\hbar} \frac{\boldsymbol{\mu_k}\, \boldsymbol{\alpha_{ij}}}{\boldsymbol{\omega_{IR}} - \boldsymbol{\omega} - \boldsymbol{i\Gamma}} \tag{11}$$

where Γ is the Lorentzian width of the vibrational band, μ_k is the IR transition dipole, and α_{ij} is the Raman polarizability. Two noteworthy consequences arise from equation (11). Firstly, when the ω is at the vibrational transition of the molecules ω_{IR}, the β maximize and accordingly the I_{SFG} is enhanced (from equation 8-10). Secondly, β is effective only when both the Raman and the IR transition probabilities are non-zero. SFG active vibrational mode must be both Raman and IR active.

The macroscopic resonant susceptibility, $\chi^{(2)}_R$ is represented as: [10-12]

$$\boldsymbol{\chi}^{(2)}_{\mathbf{R}} = \frac{\boldsymbol{A}}{\boldsymbol{\omega_{IR}} - \boldsymbol{\omega} - \boldsymbol{i\Gamma}} \tag{12}$$

where A is the SFG amplitude. In reality, the produced SFG signal is a product of the sum of all the resonant and nonresonant contributions of the substrate, $\chi^{(2)}_{NR}$: [10-14]

$$\chi^{(2)} = \sum_{n} \chi^{(2)}_{R,n} + \chi^{(2)}_{NR}$$

$$\chi^{(2)} = \sum_{n} \frac{A}{\omega_{IR} - \omega - i\Gamma} + \chi^{(2)}_{NR} \tag{13}$$

The fitting procedure for SFG spectrum is described in Appenix II.

2.6.3 Fresnel factor

The $\chi^{(2)}_{eff}$ term depends on the polarization and geometry (angle of incidence of lights relative to the position of a surface). There are four nonvanishing components of $\chi^{(2)}$ in the azimuthally isotropic interface as shown [10-12]

$$\begin{aligned} &\chi_{zzz} \\ \chi_{xxz} &= \chi_{yyz} \\ \chi_{zxx} &= \chi_{zyy} \\ \chi_{xzx} &= \chi_{yzy} \end{aligned} \tag{14}$$

in which the z-axis is defined as the surface normal and the x-axis in the incident plane. By using the polarization combinations ssp, sps, pss and ppp (each letter representing a polarization of SFG, visible, and infrared, respectively), the four nonvanishing component can be deduced:

$$\boldsymbol{\chi_{eff,ssp} = F_{yy}(\omega_{SFG})F_{yy}(\omega_{VIS})F_{yy}(\omega_{IR})\sin\theta_{IR}\,\chi_{yyz}} \quad (15)$$

$$\chi_{eff,sps} = F_{yy}(\omega_{SFG})F_{zz}(\omega_{VIS})F_{yy}(\omega_{IR})\sin\theta_{VIS}\,\chi_{yzy} \quad (16)$$

$$\chi_{eff,pss} = F_{zz}(\omega_{SFG})F_{yy}(\omega_{VIS})F_{yy}(\omega_{IR})\sin\theta_{SFG}\,\chi_{zyy} \quad (17)$$

$$\begin{aligned}\chi_{eff,ppp} = {} & -F_{xx}(\omega_{SFG})F_{xx}(\omega_{VIS})F_{zz}(\omega_{IR})\cos\theta_{SFG}\cos\theta_{VIS}\sin\theta_{IR}\,\chi_{xxz} \\ & -F_{xx}(\omega_{SFG})F_{zz}(\omega_{VIS})F_{xx}(\omega_{IR})\cos\theta_{SFG}\sin\theta_{VIS}\cos\theta_{IR}\,\chi_{xzx} \\ & +F_{zz}(\omega_{SFG})F_{xx}(\omega_{VIS})F_{xx}(\omega_{IR})\sin\theta_{SFG}\cos\theta_{VIS}\cos\theta_{IR}\,\chi_{zxx} \\ & +F_{zz}(\omega_{SFG})F_{zz}(\omega_{VIS})F_{zz}(\omega_{IR})\sin\theta_{SFG}\sin\theta_{VIS}\sin\theta_{IR}\,\chi_{zzz}\end{aligned} \quad (18)$$

where F_{xx}, F_{yy} and F_{zz} are given by

$$\boldsymbol{F_{xx}(\omega_i) = \frac{2n_1(\omega_i)cos\,\theta_2}{n_1(\omega_i)cos\,\theta_2 + n_2(\omega_i)cos\,\theta_1}} \quad (19)$$

$$F_{yy}(\omega_i) = \frac{2n_1(\omega_i)cos\,\theta_1}{n_1(\omega_i)cos\,\theta_1 + n_2(\omega_i)cos\,\theta_2} \quad (20)$$

$$F_{zz}(\omega_i) = \frac{2n_2(\omega_i)cos\,\theta_1}{n_1(\omega_i)cos\,\theta_2 + n_2(\omega_i)cos\,\theta_1}\left(\frac{n_1(\omega_i)}{n'(\omega_i)}\right)^2 \quad (21)$$

It is shown here that the Fresnel factors are functions of the refractive indices of the beam approaching the interface and therefore, according to equation (9), the SFG intensity is greatly influenced by these terms. The Fresnel factors, F_{xx}, F_{yy}, and F_{zz} are the diagonal elements of $F(\omega_i)$. The beam with ω_i is approaching from media with index of refraction

n_1 into the material with index of refraction n_2; $n'(\omega_i)$ is the refractive index of the interfacial layer, θ_1 and θ_2 are the incidence angle and the refracted angle of the light. The calculation of Fresnel factors are described in Appendix III.

2.7 Bibliography

(1) Rothen, A. *Rev. Sci. Instruments* **1945**, *16*, 26.

(2) Vedam, K. *Thin Solid Films* **1998**, *313*, 1.

(3) Drude, P. *Ann. Phys.* **1887**, *32*, 584.

(4) Tompkins, H. G.; McGahan, W. A. *Spectroscopic Ellipsometry and Reflectometry, A User's Guide*. Wiley-VCH: Weinheim, Germany, **1999**.

(5) Tompkins, H. G. *A User's Guide to Ellipsometry*. Academic Press: San Diego, United States, **1993**.

(6) Seah, M.P.; Briggs, D. *Practical Surface Analysis by Auger and X-ray Photoelectron Spectroscopy*. Wiley & Sons: New York, United States, **1983**.

(7) Binnig, G.; Quate, C. F.; Gerber, Ch. *Phys. Rev. Lett.* **1986**, *56*, 930-933.

(8) Young, T. *Phil. Trans. R. Soc.* **1805**, *95*, 65.

(9) Baldwin, G. C. *An Introduction to Nonlinear Optics*. Plenum Press: New York, United States, **1974**.

(10) Zhuang, X.; Miranda, P.B.; Kim, D.; Shen, Y. R. *Phys. Rev. B* **1999**, *59*, 12632-12640.

(11) Lambert, A.G.; Davies, P. B. *Appl. Spectrosc. Rev.* **2005**, *40*, 103.

(12) Miranda, P. B.; Shen, Y. R. *J. Phys. Chem. B* **1999**, *103*, 3292.

(13) Shen, Y. R.; Ostroverkhov, V. *Chem. Rev.* **2006**, *106*, 1140.

(14) Gopalakrishnan, S.; Liu, D.; Allen, H. C. *Chem Rev.* **2006**, *106*, 1155.

(15) Richmond, G. L. *Chem. Rev.* **2002**, *102*, 2693.

Chapter 3. Structure and reactivity of ester-terminated monolayers on silicon

Carboxylic acid-terminated monolayers on crystalline silicon surfaces can be readily modified with biological macromolecules for the fabrication of semiconductor-based biosensing devices. They were prepared by acid-catalyzed hydrolysis of alkoxycarbonyl (ester)-terminated monolayers, and studied by vibrational sum frequency generation (SFG) spectroscopy. The C-H vibration region of the SFG spectra consists of strong methyl bands with significant contributions from methylene stretching modes, indicating that the ester monolayers are generally ordered but with considerable gauche defects in the alkyl chains in comparison with n-alkyl monolayers. After hydrolysis, the methylene stretching modes prevail, with "residues" of the methyl modes, indicating incomplete hydrolysis and disruption of the monolayer structure.

This chapter is reproduced in part with permission from: Asanuma, H.; Noguchi, H.; Uosaki, K.; Yu, H.-Z. *J. Phys. Chem. B* **2006**, *110*, 4892–4899.

3.1 Introduction

Silicon is one of the most widely used semiconductors in modern technology; therefore, an understanding of the fundamental principles underlying its surface

chemistry is essential.[1] Organic monolayers covalently bonded to the silicon surface have gained much attention since their introduction about a decade ago,[2] because of their well-defined structure and the possibility to introduce diverse electrical and optical functionalities to the system.[3] The preparation of these monolayers are not sophisticated; they can be readily prepared from hydrogen-terminated silicon (H-Si) and diacyl peroxides, terminal olefins, or Grignard reagents.[2-7] Electrochemical reduction of aryldiazonium ions on silicon electrodes[8] and the reaction of alkylmagnesium or alkyllithium reagents with halogenated silicon surfaces,[9] have been also explored as alternative synthetic routes.

ω-Functionalized organic monolayers on silicon allow the immobilization of biomolecules and can therefore be used as platforms for the fabrication of biochips.[10-14] The ease of further derivatization makes carboxy (-COOH) one of the most versatile functional groups for surface modification.[5a,6b,15] Because of the reactivity of carboxylic acids toward hydrogen-terminated silicon,[5a,16] carboxy-terminated monolayers are most frequently prepared by acid- or base-catalyzed ester hydrolysis.[15] In the past, such surface hydrolysis reactions have been mainly investigated by attenuated total reflectance (ATR)-FTIR, ellipsometry, and wetting measurements.[5a,6b,15] Unfortunately these techniques provide limited information on the extent of ester hydrolysis and the conformational change of the monolayer structure. In the present study, we have explored the feasibility of using sum frequency generation (SFG) spectroscopy, a novel and powerful spectroscopic technique, to elucidate these fundamental issues, which are critical for proficient immobilization of biological macromolecules.

SFG spectroscopy is based on a second-order nonlinear optical effect of a photon generated at a frequency equal to the sum of the frequencies of two incident light beams.[17] It is not observed in media exhibiting inversion symmetry under the electric dipole approximation. Infrared-visible SFG has been utilized most commonly as it provides information on molecular interactions and orientations.[17b,c] Unparalleled surface sensitivity and the ability to detect specific vibrations at buried interfaces along with short time-scale resolution are its main advantages over conventional infrared (FTIR and Raman) techniques. Another unique feature of SFG is its selection rule: to be detectable the vibrational modes must be both Raman- and IR-active. Furthermore, the polarization combination of SFG, visible, and IR beams determines the SFG intensity observed. Particularly, the ssp (s-polarized SFG, s-polarized visible, and p-polarized IR) combination probes surface vibrational modes with a dipole moment perpendicular to the interface, while the sps and pss combinations detect vibrational modes with a dipole moment parallel to the surface. The ppp combination has no vanishing components, thus it depends on all tensor elements, i.e., ppp-polarized SFG spectra exhibit vibrational modes with both perpendicular and parallel components. All these features make SFG spectroscopy a highly sensitive, surface-specific technique for studying molecular conformations.[18-24] Shen and co-workers pioneered SFG studies of molecular interfaces, initially by examining monolayers of coumarin 504 molecules spin-coated on quartz,[18a] and later by monitoring the C-H stretching modes of methanol and pentadecanoic acid adsorbed on glass and water.[18b] The polarization characteristics of the SFG signals revealed the molecular orientation changes in a Langmuir film of pentadecanoic acids when the surface density was varied.[20c] At the methanol vapour/liquid interface, the

terminal methyl groups were found to point away from the liquid with a very broad orientational distribution.[18d]

The study of octadecyltrichlorosilane (OTS) monolayers on silica by Guyot-Sionnest et al. revealed that the alkyl chains were oriented normal to the surface.[19] Liu et al. examined the adsorption of OTS at silica/solvent interfaces, particularly the role of water in the cross-linking chemistry.[20] Ye et al. investigated the interactions between water and OTS-modified quartz and found that water molecules flipped at the quartz/OTS interface while those at the OTS surface maintained their orientation upon changing the pH from neutral to acidic.[21] Chen et al. detected different molecular structures at polymer/silane interfaces, i.e., the silane molecules adopted different conformations at the interface depending on the surface structure of the polymer.[22] Recently, Voges et al. characterized ω-ester-siloxane monolayers on glass before and after hydrolysis;[23] they observed significant differences between their spectra and those of silica/glass substrates modified with simple long-chain alkyl molecules.[24] All these previous studies demonstrate the capabilities of SFG spectroscopy to gain a better understanding of surface chemistry at the molecular level.

SFG investigations of organic monolayers directly bonded to silicon surfaces are limited to date.[25-27] Ye et al. have investigated the stability of hydrogen-terminated Si (111) surfaces by monitoring the Si-H stretching mode, and reported wavelength-dependent photo-oxidation processes involving adsorbed water molecules.[25] Ishibashi et al. have communicated an SFG study of n-alkyl monolayers on Si (111) surfaces two years ago, and suggested that the molecular conformations are chain-length dependent.[26] Nihonyanagi *et al.* have recently confirmed the epitaxial arrangement and high

conformational order of organic monolayers on silicon.[27] In particular, all-trans conformation of the methylene groups of octadecyl monolayers on Si(111), and a tilt angle of the methyl group of about 85ºwere reported.[27] Now we are extending the scope of our research to the characterization of ω-functionalized organic monolayers on silicon from both the structure and reactivity perspectives.

The following features make SFG spectroscopy particularly suitable for this investigation:[17] (1) SFG is sensitive to non-centrosymmetric structures such as methyl groups, which means that the progress of ester hydrolysis on a surface can be readily monitored by the disappearance of the methyl C-H bands. ATR-FTIR is not sensitive for this task due to the strong IR signals from both methylene and methyl stretches which are usually overlapping. (2) SFG can provide information about the order and molecular orientation in the monolayers, particularly the possible structural disturbances caused by hydrolysis. We believe that this SFG study could resolve the controversy involving the interpretation of the hydrolysis products on silicon surfaces,[5a, 6b, 15] and contribute to a better understanding of the structure-reactivity correlation in molecular films.

3.2 Experimental section

3.2.1 Materials.

All chemicals were of reagent-grade quality and used as received, unless otherwise stated. Milli-Q water (>18.3 MΩ·cm) was used throughout the experiments. 1-Dodecene (98%), 10-undecylenic acid (98%), and 1,1,1-trichloroethane (99.5%) were purchased from Aldrich; tetrahydrofuran (THF), methanol (99.0%), ethanol (99.0%),

propanol (99.0%), sulfuric acid (96%), and hydrogen peroxide (30%) from Wako Chemicals; ammonium fluoride (40%) from Morita Chemical Industries.

3.2.2 Synthesis.

The long-chain ester molecules, methyl 10-undecenoate (**Me-UD**), ethyl 10-undecenoate (**Et-UD**), and propyl 10-undecenoate (**Pr-UD**), were prepared according to the method of Sieval et al.[5a] In brief, a mixture of 10-undecylenic acid (45.6 g) and the desired alcohol (50 mL) was allowed to reflux for 3 h with a few drops of sulfuric acid. For the preparation of **Pr-UD**, the reaction was carried out in a Dean-Stark setup and 40 mL toluene was added. After removal of alcohols and solvents via vacuum distillation, the crude product was dissolved in diethyl ether. It was then washed with saturated sodium bicarbonate solution, water and potassium chloride solution, and dried over magnesium sulfate. The product was obtained upon vacuum distillation, and its structure was confirmed by ^{1}H NMR spectroscopy.[5a]

1-Dodecene was distilled from sodium under reduced pressure (20-30 Torr); **Me-UD**, **Et-UD**, and **Pr-UD** were further purified by passing through an activated Al_2O_3 column.

3.2.3 Sample preparation.

Silicon (111) wafers (3.0-5.0 Ω·cm, n-type, donated by Shin-Etsu Semiconductors) were cut into pieces (1.5 × 2 cm^2), and cleaned in "piranha" solution (3:1 mixture of concentrated H_2SO_4 and 30% H_2O_2) at 90° C for 30 min. CAUTION: *"Piranha" solution reacts violently with organic materials; it must be handled with extreme care.* After copious rinsing with deionized water, the wafers were etched in

deoxygenated NH_4F (40 % aqueous solution) to remove the native oxide and obtain hydrogen-terminated silicon (H-Si). Attenuated total reflectance (ATR) silicon crystals ($25 \times 5 \times 1$ mm^3, Harrick Scientific Inc.) for FTIR measurements were cleaned by the standard RCA procedure,[28] prior to the etching steps outlined above.

The fresh H-Si samples were transferred under argon into Schlenk tubes containing 2-3 mL of deoxygenated modification reagents, and heated to 160 °C for 4 h. The modified silicon samples were then rinsed at room temperature with THF and 1,1,1-trichloroethane before characterization. The hydrolysis of ester-terminated monolayers on silicon was carried out by immersion in 2.0 M HCl at 70º C for 2 h.

3.2.4 Surface characterization.

The SFG system employed a picosecond Nd: YAG laser (PL2143B, Ekspla) to pump an optical parametric generation / optical parametric amplification / difference frequency generation (OPG/OPA/DFG) system, which generates tunable infrared radiation in the range of 2.3 to 8.5 μm.[27] The second harmonic output of the YAG (yttrium-aluminum-garnet) laser (532 nm) was used as the visible light source. The two beams were loosely focused onto the sample located on a rotational stage, at the incident angle of 70º for visible and of 50º for infrared light. Thus produced SFG beam at an angle of 70.2º was filtered through irises and a monochromator (Oriel Instruments, MS257), and detected by a photomultiplier tube (PMT: Hamamatsu, R3896). The SFG signal is normalized to the intensities of visible and infrared light. The SFG, visible, and IR beams were all p-polarized (abbreviated as ppp). All measurements were carried out in air at

room temperature (22 ± 2 ºC). The Si (111) sample was placed on the stage with [$2\bar{1}\bar{1}$] direction set in the plane of the incident beams.

The following equations are utilized to express the SFG intensity (I_{SFG}), and to fit the spectra:

$$I_{SFG} = \frac{8\pi^3 \omega_{SFG}^2 \sec^2 \theta_{SFG}}{c^3} \left| \chi_{eff}^{(2)} \right|^2 I_{Vis} I_{IR} \qquad \textbf{(1)}$$

$$\chi_{eff}^{(2)} = \left| \chi_{NR}^{(2)} \right| e^{i\phi_n} + \sum \frac{A_n}{\omega_{IR} - \omega_n + i\Gamma_n} \qquad (2)$$

where $\chi_{eff}^{(2)}$ and $\chi_{NR}^{(2)}$ are the effective second-order nonlinear susceptibilities of the resonant and the non-resonant component, respectively; ϕ_n is the phase angle between the resonant and the non-resonant component; c, A_n, and Γ_n are the speed of light in vacuum, amplitude, and the damping constant width of the surface vibration mode (n) corresponding to frequency ω_n, respectively. The quality of the fit is judged by r^2 values that was at least 0.800 and above. The best r^2 fit was approximately 0.7 for the SFG spectrum of methyl ester monolayer (Figure 3.5a top) which had relatively low signal-to-noise ratio, however the peak positions were confirmed multiple times from different set of samples. The detailed description of fitting routine and the fitting parameters are described in Appendix II.

ATR-FTIR spectra were recorded on a Nicolet Nexus-IR 560 spectrometer equipped with an MCT (mercury cadmium telluride) detector cooled with liquid nitrogen. The ATR crystals were mounted in a dry air-purged sample chamber with the IR beam

focused normal to one of the 45º bevels. The spectra were collected for 1000 scans at a 2.0 cm^{-1} resolution, and the background files were obtained with freshly prepared oxidized silicon surfaces. All the spectra were measured in the 4000-1500 cm^{-1} range that is limited by the high absorbance of silicon ATR crystals below 1500 cm^{-1}. No corrections were made for either water vapour or atmospheric CO_2. In most cases, a linear baseline correction was applied.

Wetting measurements were performed on an AST Optima contact angle system at ambient conditions (18-22ºC, 30-35% relative humidity) using a horizontal light beam to illuminate the water droplet. Contact angles were measured for at least three independent samples (4-5 readings at different spots per sample) with 2.0-µL drops of deionized water.

3.3 Results and Discussion

3.3.1 ATR-IR and wetting measurements.

Wetting measurements showed that the water contact angles of the three ester-terminated monolayers (Table 3.1) rise in the following order: **Me-UD < Et-UD < Pr-UD** monolayer, i.e., the hydrophobicity increases with the chain length of the alkoxy group. Upon treatment with dilute hydrochloric acid (2.0 M HCl) for 2 h at 70 °C, the water contact angles dropped significantly. This increase in hydrophilicity is attributed to the formation of carboxylic acid groups upon hydrolysis (Figure 3.1). However, the values obtained for the hydrolyzed surfaces (in the range of 50 to 57°) were substantially higher than those of carboxylic acid-terminated monolayers on gold prepared by direct

Monolayer	before hydrolysis	after hydrolysis
Me-UD	67 ±1°	52 ± 2°
Et-UD	74 ± 2°	53 ± 2°
Pr-UD	77 ± 1°	57 ± 1°

Table 3.1 Water contact angles on silicon surface modified with ester-terminated monolayers before and after hydrolysis.

adsorption of $HS(CH_2)_nCOOH$, which are essentially zero.[29] The relatively low hydrophilicity of the carboxylic acid-terminated monolayers on silicon prepared via ester hydrolysis may be attributed to the presence of unreacted ester groups. However, this conclusion is not obvious, as the density of the alkanethiolate monolayers on gold is significantly higher, which makes a direct comparison difficult. The changes of wetting properties among these monolayers may be due to either different hydrolysis efficiencies, or to variations in surface coverage/morphology.

To clarify this question, we also examined the three ester-terminated monolayers by ATR-FTIR measurements. Before hydrolysis, the most evident bands observed in the 3200-2700 cm^{-1} region are the CH_2 symmetric stretch (d^+, 2851-2 cm^{-1}) and asymmetric stretch (d^-, 2920-1 cm^{-1}) (Figure 3.2). The wavenumbers of the d^- modes are comparable (Table 3.1), suggesting that they are of similar quality in terms of packing density and molecular orientation, i.e., they are ordered and closely packed monolayers even compared to unfunctionalized alkyl monolayer.[30] However, these bands are broader than those obtained for *n*-alkyl monolayers, which is possibly due to contributions from different types of CH_2 groups, e.g., the propoxy group has two methylene groups in addition to those linked to the silicon (Figure 3.3).

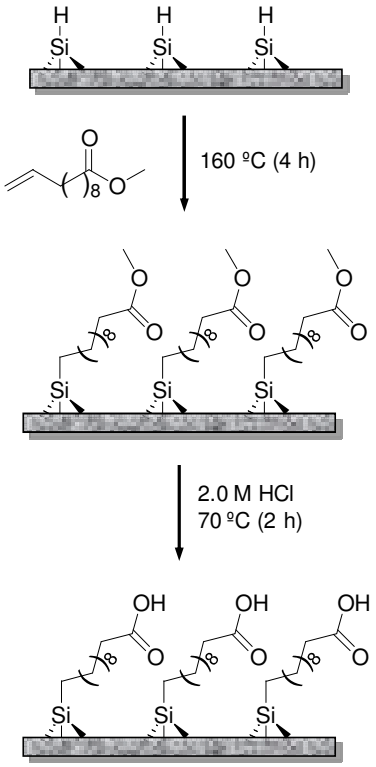

Figure 3.1 Schematic illustration of the preparation of ester-terminated monolayers on silicon and the subsequent hydrolysis reaction. A methyl 10-undecenoate (Me-UD) monolayer is shown as example.

The carbonyl stretches were observed at 1740-2 cm^{-1} (Figure 3.2); upon hydrolysis this band shifts to 1715 cm^{-1}, accompanied by a shoulder at 1740-2 cm^{-1}. The intensities of the shoulder peaks differ from each other: smallest and least discrete for the **Me-UD** monolayers, but well-defined at 1740 cm^{-1} for **Pr-UD** (insets of Figure 3.2). The assignment of the bands at 1715 cm^{-1} is unambiguous: they are attributed to hydrogen-bonded carboxy groups in which carboxy group situated adjacent to each other is forming a dimer.[15,31] The shoulder band at 1740 cm^{-1} may be due to unreacted

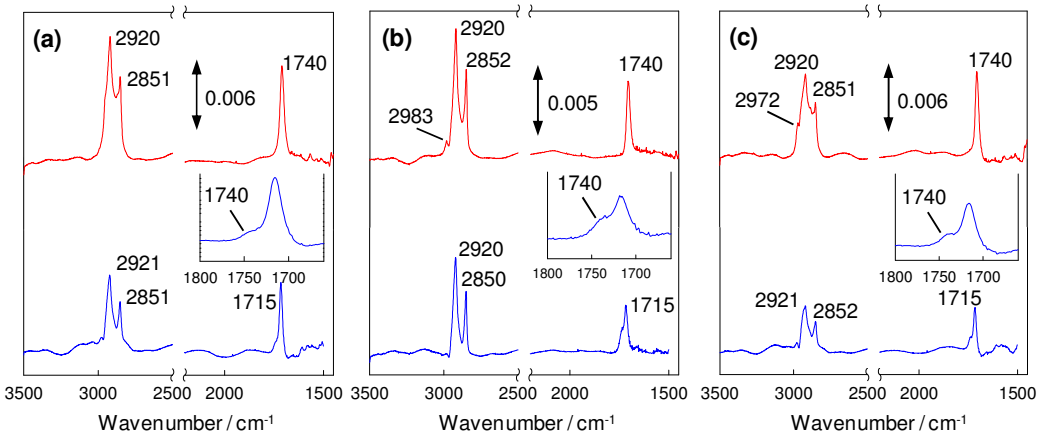

Figure 3.2 ATR-FTIR spectra of the ester-terminated monolayers on silicon: (a) Me-UD, (b) Et-UD, and (c) Pr-UD. In each panel, the top trace (in red) shows the spectrum obtained from the monolayer before, the bottom trace (in blue) after hydrolysis; the inset shows the enlarged carbonyl region.

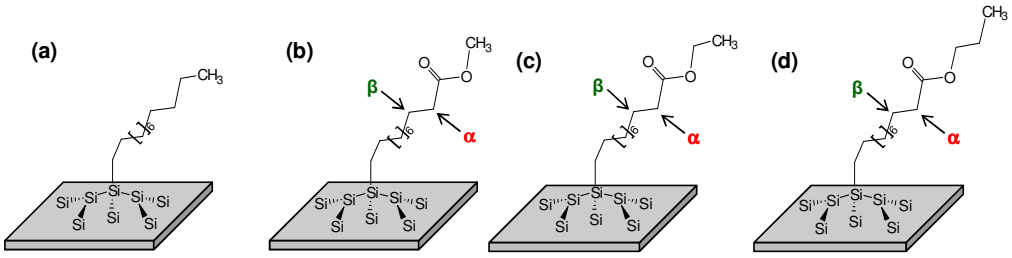

Figure 3.3 Schematic representations of (a) dodecyl monolayers and ester-terminated monolayers on silicon formed from (b) Me-UD, (c) Et-UD, and (d) Pr-UD.

ester groups or free (non-hydrogen-bonded) carboxy groups (or a combination of both).[5a,6b,15] The former interpretation would indicate incomplete hydrolysis, the latter a completely hydrolyzed surface with different surface-bonding properties. The bands at 2983 and 2973 cm^{-1} for the **Et-UD** and **Pr-UD** monolayers are assigned to the CH_3 asymmetric stretch (r^-); their low intensities do not allow further interpretation of the hydrolysis reaction.

	Vibrational modes	Monolayer		
		Me-UD	**Et-UD**	**Pr-UD**
before hydrolysis	υ_s (CH_2), d^+	2851	2852	2851
	υ_{as} (CH_2), d^-	2920	2920	2920
	υ_{as} (CH_3), r^-	~	2983	2972
	υ (C=O)	1742	1740	1740
after hydrolysis	υ_s (CH_2), d^+	2851	2850	2852
	υ_{as} (CH_2), d^-	2921	2920	2921
	υ_{as} (CH_3), r^-	~	~	~
	υ (C=O)	1715	1715	1715
	υ (C=O)	1740[a)]	1740[a)]	1740[a)]

a) A shoulder band besides the peak at 1715 cm^{-1}.

Table 3.2 Peak assignments and positions (cm^{-1}) of the ATR-FTIR spectra for the ester-terminated monolayers on silicon (before and after hydrolysis).

While ATR-FTIR and wetting measurements provide some information about the monolayer structure and reactivity, they do not reveal details about the hydrolysis efficiency and potential structural changes.[15] Therefore, SFG studies of the three ester-terminated monolayers before and after hydrolysis were carried out. The spectrum of dodecyl monolayers was also obtained for comparison, while the spectrum of the monolayers prepared from 10-undecylenic acid was included for peak assignment purposes. The qualities of SFG spectra were comparable to those reported in the literature.[25-27]

3.3.2 Peak assignments and structure evaluation.

Because SFG vibrational modes must be both IR- and Raman-active,[32] conventional IR and Raman band assignments are often used as references for the interpretation of SFG spectra.[33] The most widely characterized alkyl groups, CH_3 and CH_2, show strong SFG bands in the 2800-3000 cm^{-1} region. The peaks in this range are

generally assigned to C-H symmetric (2862-82 cm^{-1} for CH_3, 2843-63 cm^{-1} for CH_2) and asymmetric stretching (2952-72 cm^{-1} for CH_3, 2916-36 cm^{-1} for CH_2). These bands are often accompanied by Fermi resonance (FR) peaks, and there are significant overlaps between CH_3 and CH_2 stretches. The polarization settings of the laser system add another dimension of difficulty to the interpretation of SFG spectra. All the above factors lead to ambiguities so that the spectral assignments reported in the literature do not always agree.[34]

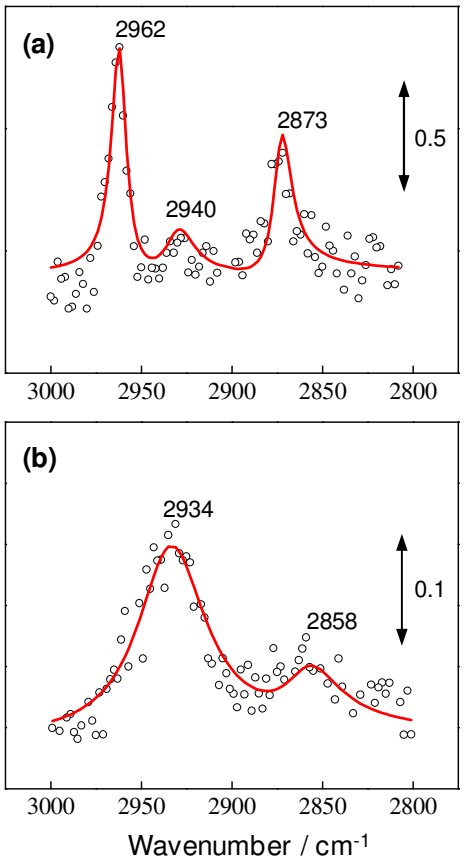

Figure 3.4 SFG spectra of monolayers prepared from the reaction of (a) 1-dodecene and (b) 10-undecylenic acid with hydrogen-terminated silicon (111). The solid lines (red) are the best fits based on equations (1) and (2).

The interpretation of the spectrum of 1-dodecyl monolayers on silicon is simple (Figure 3.4a). The three major bands are due to vibrations of the terminal CH_3 groups: C-H symmetric stretch (r^+, 2873 cm^{-1}), Fermi resonance between r^+ and the C-H bending overtone (FR, 2940 cm^{-1}), and C-H asymmetric stretch (r^-, 2962 cm^{-1}).[26-27] Although the contributions from CH_2 groups were also considered, they are negligible in the optimized fitting results (solid line in Figure 3.4a). The fact that only terminal CH_3 contributes to the SFG signal indicates that essentially all CH_2 groups adopt the all-trans configuration, which is consistent with our SFG study of octadecyl monolayers on silicon reported previously.[27] Ishibashi et al. have observed weak contributions from CH_2 stretches (broad bands around 2914 cm^{-1} and 2850 cm^{-1}), particularly for the n-alkyl monolayers that contain odd numbers of carbons.[26]

The peak assignments for ester-terminated monolayers on silicon are challenging because their SFG spectra contain several discernible peaks (Figures 3.5). At least five bands can be distinguished: 2850-5 cm^{-1}, 2885-90 cm^{-1}, 2902-5 cm^{-1}, 2930 cm^{-1}, and 2960-63 cm^{-1}. By analogy to the spectrum of dodecyl monolayers, which is dominated by CH_3 stretching modes, the 2885-90 cm^{-1} band can be assigned to r^+, and 2960-3 cm^{-1} to r^- modes from the terminal methyl groups, respectively. There are few possibilities for the other three bands: 2853-7 cm^{-1} may be either a C-H symmetric stretch of CH_2 (d^+) or r^+, 2902-5 cm^{-1} a C-H asymmetric (d^-) stretch or Fermi resonance of CH_2 (d^- or FR), and 2930 cm^{-1} could be either d^- or FR(CH_3). The deconvoluted peaks are shown in Figure 3.5 in red line. Deconvolution was carried out by individually plotting a peak considering A_n, ω_{IR}, and Γ_n (Appendix II, parameters A, B and C) and without other parameters $\chi^{(2)}_{NR}$ and ϕ_n (Appendix II, parameters D and F).

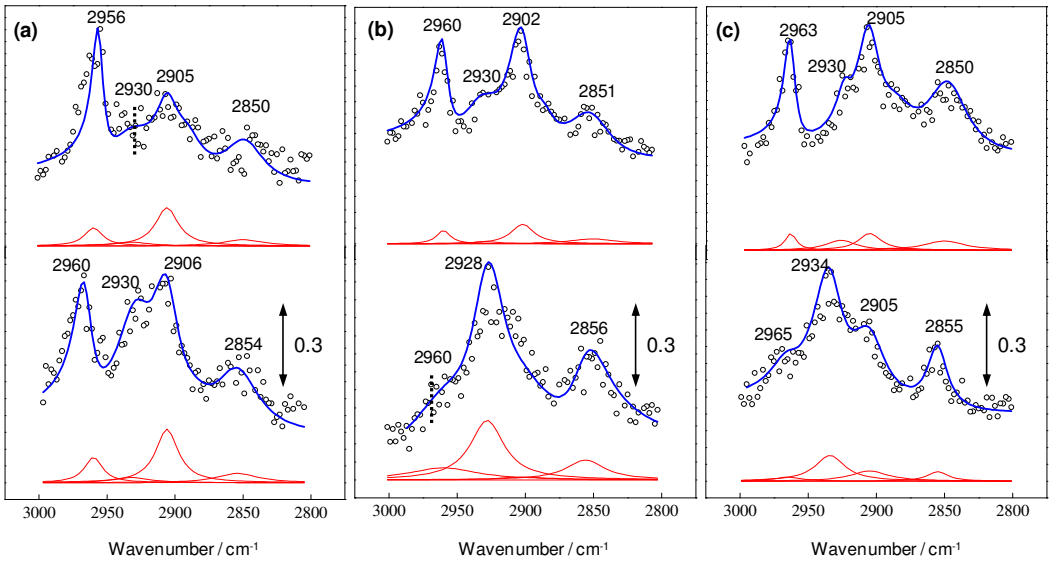

Figure 3.5 SFG spectra of the ester-terminated monolayers on silicon: (a) Me-UD, (b) Et-UD, and (c) Pr-UD. In each panel, the top trace shows the spectrum obtained from the monolayers before, and the bottom one after hydrolysis. The solid lines (in blue) are the best fits based on equation (1) and (2) judging by the r^2 value. The deconvoluted peaks are shown in red at the bottom of each SFG spectrum.

Under carefully controlled irradiation conditions, carboxylic acid-terminated monolayers were prepared by the reaction of 10-undecylenic acid with H-Si.[35-36] Their SFG spectrum was recorded (Figure 3.4b) to assist the band assignments of the ester-terminated monolayers. Broad peaks were found at 2934 and 2858 cm^{-1} and can be assigned to d^- and d^+, respectively, since the monolayer formed from 10-undecylenic acid does not contain methyl groups. Accordingly, the bands at 2930 cm^{-1} and 2853-7 cm^{-1} of ester-terminated monolayers should be assigned to d^- and d^+. The band at 2902-5 cm^{-1} is particularly distinct for the **Et-UD** and **Pr-UD** monolayers (Figure 3.5b and 3.5c), and most difficult to assign. It is possible to attribute this band to FR(CH_2), but this would violate the selection rule.[34] We are cautiously attributing this band to the asymmetric stretch of CH_2 (d^-_{ω}) instead, consistent with the assignment of the C-H stretching

vibrations of octadecylsiloxane on glass by Chow et. al.[24] In our case, there are two different types of d^- stretches, 2930 cm^{-1} and 2902-5 cm^{-1}; the former can be attributed to trans-gauche defects in the backbone chains, which have been observed by Ishibashi et al.[36] Since no 2902-5 cm^{-1} band was observed for n-alkyl monolayers on silicon,[26-27] this peak must be related to CH_2 groups adjacent to the carboxyl group (Figure 3.3). All peak assignments for the ester-terminated monolayers on silicon before and after hydrolysis are summarized in Tables 3.3 and 3.4.

The spectrum of dodecyl monolayers on silicon (Figure 3.4a) is composed of three major bands, 2873 cm^{-1} (r^+), 2940 cm^{-1} (FR), and 2962 cm^{-1} (r^-). The contributions from methylene groups are negligible, suggesting densely packed, all-trans configurations of the alkyl chains. For the ester-terminated monolayers, the methyl-related bands are still very strong (Figure 3.5), but accompanied with significant contributions from CH_2 stretches (d^+ and d^-). It has been proposed by Ishibashi et al. that gauche defects (particularly the "twisted stems" near the silicon substrate) in the alkyl chains play an important role, since a gauche conformation breaks the local symmetry of the backbone and thereby increases the intensity of the CH_2 stretching modes. This indicates that the alkyl chains of ester-terminated monolayers are less ordered than those of n-alkyl monolayers on silicon, i.e., the torsional angles of some C-C bonds deviate from the ideal value for all-trans conformations. The less prominent CH_3 signals also support this hypothesis: structural defects disturb the orientational order of the terminal (methyl) groups (thus weakening their SFG signals). All of these observations suggest that the ester groups induce distorted structures by prohibiting perfect packing of the alkyl chains, an effect not evident in conventional IR spectra.[15]

Although the number of gauche defects per alkyl chain cannot be calculated quantitatively, the ratio of the CH_3 and CH_2 signal intensities serves as a reasonable measure of the relative order within the backbone alkyl chains: it increases as a monolayer becomes more oriented.[37] The calculated r^- / d^- ratios (~2930 cm^{-1} / ~2960 cm^{-1}) decrease from 2.8 for **Me-UD** to 1.7 for **Et-UD** and 1.4 for **Pr-UD** monolayers,

Vibrational modes	Monolayer		
	Me-UD	**Et-UD**	**Pr-UD**
υ_s (CH_2), d^+	2853	2857	2856
υ_{as} (CH_2), d^-_{ω}	2905	2902	2905
υ_{as} (CH_2), d^-	2930	2930	2930
υ_s (CH_3), r^+	2890	2885	2885
υ_{as} (CH_3), r^-	2960	2960	2963

Table 3.3 SFG vibrational frequencies (cm^{-1}) and their proposed resonant modes for the ester-terminated monolayers.

Vibrational modes	Monolayer		
	Me-UD	**Et-UD**	**Pr-UD**
υ_s (CH_2), d^+	2854	2856	2855
υ_{as} (CH_2), d^-_{ω}	2906	2901	2905
υ_{as} (CH_2), d^-	2930	2928	2934
υ_s (CH_3), r^+	~	~	~
υ_{as} (CH_3), r^-	2964	2960	2965

Table 3.4 SFG vibrational frequencies (cm^{-1}) and their proposed resonant modes for the hydrolyzed ester-terminated monolayers.

indicating that methyl ester-terminated monolayers (**Me-UD**) are the most ordered (minimum gauche defects) among the three. This means that the presence of the ester-groups plays an important role: the bulkier the ester group, the more disordered the monolayer becomes.

3.3.3 Hydrolysis efficiency

The SFG spectra of the hydrolyzed monolayers are shown at the bottom of each panel in Figure 3.5. The most significant feature of these spectra is that all CH_3 bands are still discernible, but their intensities have decreased significantly upon hydrolysis. This confirms that the hydrolysis reaction under acidic conditions is not complete, therefore, removes the previous uncertainty about the assignment of the shoulder peak near 1740 cm^{-1} in the IR spectra (Figure 3.2): it is definitely and unambiguously due to unreacted ester groups. Steric hindrance is the most likely cause of incomplete acid-catalyzed hydrolysis, which is initiated by protonation of the carbonyl oxygen, followed by nucleophilic attack of water to yield a tetrahedral intermediate. Subsequent proton transfer and elimination of alcohol complete the reaction.[38] The hydrophobic end-groups (alkoxy chains) may limit the accessibility of the carbonyl carbon to water, and the well-packed monolayer structure may be unfavourable for the generation of tetrahedral intermediates. In contrast, SFG studies by Voges et. al. have shown that ω-ester-siloxane monolayers on glass are completely hydrolyzed upon acid treatment (the CH_3 bands disappeared completely).[23] This difference may be attributed to the less ordered, amorphous structure of those monolayers on glass in comparison to the close-packed organic monolayers formed on crystalline silicon.

Another equally important feature of the spectra is the increase of the relative intensities of the methylene asymmetric stretching modes (d^-, ~2930 cm^{-1}) upon ester hydrolysis. As mentioned above, the d^- mode is related to gauche defects in the alkyl chains. The observed intensity increase indicates a significant disruption of the monolayer structure, which may be induced by the bulky tetrahedral intermediate formed

during the hydrolysis or by damage to the monolayers upon acid treatment (removal of some alkyl chains). However, the relative intensities of the 2902-5 bands (d^-) of the **Et-UD** and **Pr-UD** monolayers substantially decreased upon hydrolysis (Figures 3.5b and 3.5c), indicating that this band is associated with the CH_2 groups in the alkoxy chains.

3.3.4 Rotational Anisotropy

The dependence of the SFG intensity on the azimuthal angle (angle between the incidence plane of the probe beams and the [1 $\bar{2}$ 1] direction of the Si(111) surface) was examined for the three ester-terminated monolayers. A threefold pattern of the rotation anisotropy was observed for each of the monolayers at the r^- frequency (2960-5 cm^{-1}, the asymmetric CH_3 stretching mode) (Figure 3.6), suggesting the existence of lateral symmetry in these monolayer systems. A similar pattern was observed for a non-resonant frequency (e.g., 2700 cm^{-1}), but differed from that of r^- mode by 60°. The rotation anisotropies of these monolayers after hydrolysis are also depicted in Figure 3.6; they possess significant contributions from both non-resonant and resonant components.

Analogous results have been reported for octadecyl monolayers on Si(111) in our previous studies.[27] In that case, the threefold feature was attributed to the orientation of the tilted alkyl chains, based on a comparison with H-Si surfaces and alkanethiolate monolayers on gold.[27] This interpretation provides further insights into the structure and reactivity of the ω-functionalized organic monolayers on silicon. The similarity of the observed rotation anisotropies indicates that the ester-terminated monolayers possess molecular conformations similar to those of octadecyl monolayers, i.e., they are reasonably ordered with high packing density. However, in the presence of ester groups with longer alkoxy chains (e.g., for the **Pr-UD** monolayers shown in Figure 3.6, top

panels), the non-resonance component becomes more evident, i.e., the structure becomes less oriented.

Upon hydrolysis, the rotation anisotropies of these monolayers exhibit both r^- and non-resonance contributions (with different relative intensities, as shown in Figure 3.6, middle panels), indicating the existence of residual ester groups. When the system is dominated by r^-, the non-resonance contributions are negligible (Figure 3.6, top panels). This permits a comparison of hydrolysis efficiencies for the three systems. The **Me-UD**

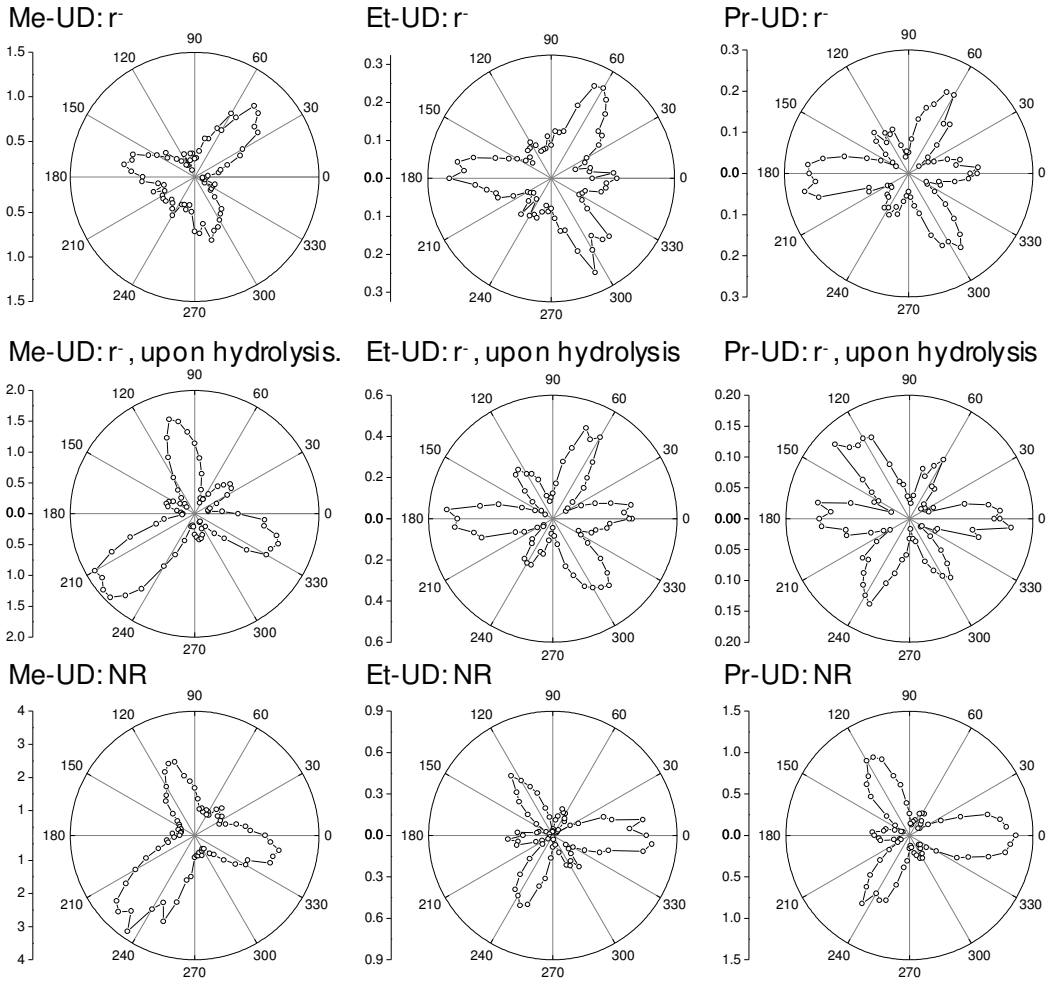

Figure 3.6 Rotation anisotropy of the SFG intensity of the r- mode (asymmetric CH3 stretch) of the three ester-terminated monolayers on silicon before (top) and after hydrolysis (middle). The non-resonance (NR) signals (bottom) are shown for comparison.

monolayer upon hydrolysis has the weakest r^- band, but a strong non-resonant signal; in contrast, the hydrolyzed **Et-UD** and **Pr-UD** monolayers seem to have signal contributions of comparable intensities at the r^- and non-resonance (NR) frequencies. Assuming that the r^-/NR ratio reflects the relative number of molecules exhibiting the signal for rotation anisotropy at the r^- frequency, the equation

$$\textbf{\textit{hydrolysis efficiency}} = \frac{\left(r^-/NR\right)_{prior\ to\ hyd.} - \left(r^-/NR\right)_{upon\ hyd.}}{\left(r^-/NR\right)_{prior\ to\ hyd.}} \qquad \textbf{(3)}$$

gives the following approximate hydrolysis efficiencies: 97 ± 1 % for **Me-UD**, 77 ± 3 % for **Et-UD**, and 72 ± 5 % for **Pr-UD** monolayers; these are relative values among Me-UD, Et-UD and Pr-UD. This is consistent with the relative intensity changes for the methyl stretches (r^- and r^+) and provides a quantitative measure of the extent of surface reactions on silicon.

3.4 Conclusion

The SFG studies have shown that ester-terminated monolayers on silicon are generally closely packed and ordered, although they have significant gauche defects compared to n-alkyl monolayers: the longer the alkoxy chain, the less ordered the monolayer becomes. It has been confirmed that the acid-catalyzed hydrolysis of ester-terminated monolayers is incomplete, and its efficiency depends on the bulky ester group. The hydrophobic ends of the alkoxy groups appear to limit the accessibility of the carbonyl carbon to the nucleophile (water), and a well-packed monolayer structure renders the generation of tetrahedral intermediates unfavourable.

3.5 Bibliography

(1) For recent reviews, see (a) Whitesides, G. M. *MRS Bulletin* **2002**, *27*, 56. (b) Carroll, R. L.; Gorman, C. B. *Angew. Chem., Int. Ed.* **2002**, *41*, 4378.

(2) (a) Linford, M. R.; Chidsey, C. E. D. *J. Am. Chem. Soc.* **1993**, *115*, 12631. (b) Linford, M. R.; Fenter, P.; Eisenberger, P. M.; Chidsey, C. E. D. *J. Am. Chem. Soc.* **1995**, *117*, 3145.

(3) (a) Sieval, A. B.; Linke, R.; Zuilhof, H.; Sudhölter, E. J. R. *Adv. Mater.* **2000**, *12*, 1457. (b) Wayner, D. D. M.; Wolkow, R. A. *J. Chem. Soc., Perkin Trans.* **2002**, *2*, 23. (c) Buriak, J. M. *Chem. Rev.* **2002**, *102*, 1271.

(4) (a) Wagner, P.; Nock, S.; Spudich, J. A.; Volkmuth, W. D.; Chu, S.; Cicero, R. L.; Wade, C. P.; Linford, M. R.; Chidsey, C. E. D. *J. Struct. Biol.* **1997**, *119*, 189. (b) Cicero, R. L.; Linford, M. R.; Chidsey, C. E. D. *Langmuir* **2000**, *16*, 5688.

(5) (a) Sieval, A. B.; Demirel, A.L.; Nissink, J. W. M.; Linford, M. R.; Van der Maas, J. H.; De Jeu, W. H.; Zuilhof, H.; Sudhölter, E. J. R. *Langmuir* **1998**, *14*, 1759. (b) Sieval, A. B.; Vleeming, V.; Zuilhof, H.; Sudhölter, E. J. R. *Langmuir* **1999**, *15*, 8288.

(6) (a) Boukherroub, R.; Morin, S.; Bensebaa, F.; Wayner, D. D. M. *Langmuir* **1999**, *15*, 3831. (b) Boukherroub, R.; Wayner, D. D. M. *J. Am. Chem. Soc.* **1999**, *121*, 11513.

(7) Fidélis, A.; Ozanam, F.; Chazalviel, J. -N. *Surf. Sci.* **2000**, *444*, L7.

(8) (a) Henry de Villeneuve, C.; Pinson, J.; Bernard, M. C.; Allongue, P. *J.*

Phys. Chem. B **1997**, *101*, 2415. (b) Allongue, P.; Henry de Villeneuve, C.; Pinson, J.; Ozanam, F.; Chazalviel, J. N.; Wallart, X. *Electrochim. Acta* **1998**, *43*, 2791.

(9) (a) Bansal, A.; Li, X.; Lauermann, I.; Lewis, N. S. *J. Phys. Chem. B* **1996**, *118*, 7225. (b) Bansal, A.; Lewis, N. S. *J. Phys. Chem. B* **1998**, *102*, 1067.

(10) (a) Strother, T.; Cai, W.; Zhao, X.; Hamers, R. J.; Smith, L. M. *J. Am. Chem. Soc.* **2000**, *122*, 1205. (b) Lin, Z.; Strother, T.; Cai, W.; Cao, X.; Smith, L. M.; Hamers, R. J. *Langmuir* **2002**, *18*, 788. (c) Lasseter, T. L.; Clare, B. H.; Abbott, N. L.; Hamers. R. J. *J. Am. Chem. Soc.* **2004**, *126*, 10220.

(11) Willner, I.; Katz, E. *Angew. Chem. Int. Ed.* **2000**, *39*, 1180.

(12) Pike, A. R.; Lie, L. H.; Eagling, R. A.; Ryder, L. C.; Patole, S. N.; Connolly, B. A.; Horrocks, B. R.; Houlton, A. *Angew. Chem. Int. Ed.* **2002**, *41*, 615.

(13) (a) Pike, A. R.; Patole, S. N.; Murray, N. C.; Ilyas, T.; Connolly, B. A.; Horrocks, B. R.; Houlton, A. *Adv. Mater.* **2003**, *15*, 254. (b) Pike, A. R.; Ryder, L. C.; Horrocks, B. R.; Clegg, W.; Connolly, B. A.; Houlton, A. *Chem. Eur. J.* **2005**, *11*, 344.

(14) (a) Wei, F.; Sun, B.; Guo, Y.; Zhao, X. S. *Biosensors and Bioelectronics* **2003**, *18*, 1157. (b) Wei, F.; Sun, B.; Liao, W.; Ouyang, J.; Zhao, X. S. *Biosensors and Bioelectronics* **2003**, *18*, 1149.

(15) Liu, Y.-J.; Navasero, N. M.; Yu, H.-Z. *Langmuir* **2004**, *20*, 4039.

(16) Lee, E. J.; Bitner, T. W.; Ha, J. S.; Shane, M. J.; Sailor, M. J. *J. Am. Chem. Soc.* **1996**, *118*, 5375.

(17) (a) Shen, Y. R. *The Principle of Nonlinear Optics*, John Wiley & Sons: New York, **1984**, p.67. (b) Shen, Y. R. *Nature* **1989**, *337*, 519. (c) Richmond, G. L. *Chem. Rev.* **2002**, *102*, 2693.

(18) (a) Zhu, X. D.; Suhr, H.; Shen, Y. R. *Phys Rev. B* **1987**, *35*, 3047. (b) Hunt, J. H.; Guyot-Sionnest, P.; Shen, Y. R. *Chem. Phys. Lett.* **1987**, *133*, 189. (c) Guyot-Sionnest, P.; Hunt, J. H.; Shen, Y. R. *Phys. Rev. Lett.* **1987**, *59*, 1597. (d) Superfine, R.; Huang, J.Y.; Shen, Y. R. *Phys. Rev. Lett.* **1991**, *66*, 1066.

(19) Guyot-Sionnest, P.; Superfine, R.; Hunt, J. H.; Shen, Y. R. *Chem. Phys. Lett.* **1988**, *144*, 1.

(20) Liu,Y.; Wolf, L. K.; Messmer, M. C. *Langmuir* **2001**, *17*, 4329.

(21) Ye, S.; Nihonyanagi, S.; Uosaki, K. *Phys. Chem. Chem. Phys.* **2001**, *3*, 3463.

(22) Chen. C.; Loch, C. L.; Wang, J.; Chen, Z. *J. Phys. Chem. B* **2003**, *107*, 10440.

(23) Voges, A. B.; Al-Abadleh, H. A.; Musorrafiti, M. J.; Bertin P. A.; Nguyen, S. T.; Geiger, F. M. *J. Phys. Chem. B* **2004**, *108*, 18675.

(24) Chow, B. C.; Ehler, T. T.; Furtak, T. E. *J. Appl. Phys. B* **2002**, *74*, 395.

(25) Ye, S.; Saito, T.; Nihonyanagi, S.; Uosaki, K.; Miranda, P. B.; Kim, D.; Shen, Y.-R. *Surf. Sci.* **2001**, 476, 121.

(26) Ishibashi, T.; Ara, M.; Tada, H.; Onishi, H. *Chem. Phys. Lett.* **2003**, *367*, 376.

(27) Nihonyanagi, S.; Miyamoto, D.; Idojiri, S.; Uosaki, K. *J. Am. Chem. Soc.* **2004**, *126*, 7034.

(28) Kern, W.; Puotinen, D. A. *RCA Rev.* **1970**, *31*, 188.

(29) Bain, C. D.; Troughton, E. B.; Tao, Y. T.; Evall, J.; Whitesides, G. M.; Nuzzo, R. G. *J. Am. Chem. Soc.* **1989**, *111*, 321.

(30) (a) Snyder, R. G.; Strauss, H. L.; Elliger, C. A. *J. Phys. Chem.* **1982**, *86*, 5145. (b) MacPhail, R. A.; Straws, H. L.; Snyder, R. G.; Elliger, C. A. *J. Phys. Chem.* **1984**, *88*, 334.

(31) Cheng, S. S.; Scherson, D. A.; Sukenik, C. N. *Langmuir* **1995**, *11*, 1190.

(32) Shen, Y. R. *Pure Appl. Chem.* **2001**, 73, 1589.

(33) Colthup, N. B.; Daly, L. H.; Wiberley, S. E. *Introduction to Infrared and Raman Spectroscopy,* 3rd Ed., Academic Press: San Diego, **1990**, Chapter 5.

(34) (a) Lu, R.; Gan, W.; Wu, B.-H.; Chen, H.; Wang, H.-F. *J. Phys. Chem. B* **2004**, *108*, 7297. (b) Lu, R.; Gan, W.; Wu, B.-H.; Zhang, Z.; Guo, Y.; Wang, H.-F. *J. Phys Chem. B* **2005**, *109*, 14118.

(35) Voicu, R.; Boukherroub, R.; Bartzoka, V.; Ward, T.; Wojtyk, J. T. C.; Wayner, D. D. M. *Langmuir* **2004**, *20*, 11713.

(36) Asanuma, H.; Lopinski, G. P.; Yu, H.-Z. *Langmuir* **2005**, *21*, 5013.

(37) (a) Messmer, M. C.; Conboy, J. C.; Richmond, G. L. *J. Am. Chem. Soc.* **1995**, *117*, 8039-8040. (b) Conboy, J. C.; Messmer, M. C.; Richmond, G. L. *J. Phys. Chem.* **1996**, *100*, 7617.

(38) McMurry, J. *Organic Chemistry*, *5th ed.*, Brooks/Cole: California, **2000**, 866.

Chapter 4. Kinetic control of the photochemical reactivity of silicon toward bifunctional molecules

Chapter 3 revealed issues related to the hydrolysis of ester groups to prepare COOH-terminated monolayers on silicon; the reaction is incomplete and introduces significant structural disruption to the originally ordered alkyl chains. In this chapter, an alternative route to carboxy-terminated monolayers on silicon will be explored. The feasibility of direct attachment of bifunctional molecules (e.g., ω-alkenoic acids) to hydrogen-terminated silicon crystal (H-Si) via Si-C linkages was assessed by comparing the photoreactivities of the alkene (–CH=CH_2) and carboxy (–COOH) terminal groups of 1-dodecene, undecanoic acid and undecylenic acid toward H-Si. The alkene terminus was found to react substantially faster than the carboxy terminus under UV irradiation (at 350 nm). By controlling the reaction time, high-quality carboxy-terminated monolayers, comparable to those formed by ester hydrolysis, can be obtained by the direct, one-step photochemical reaction of H-Si with undecylenic acid.

4.1 Introduction

The modification of semiconductor surfaces with ω-functionalized organic monolayers has enormous potential for biotechnological applications, such as the fabrication of silicon-based DNA chips, since it would permit the covalent immobilization of chemical and biological functions to solid-state devices. However, most of the methods mentioned above only produce chemically inert, methyl-terminated surfaces, which is adequate for passivation but not suitable for further surface derivatization.[1, 2, 3] In order to implement biochemical functions, e.g., the immobilization of DNA or proteins,[3-8] silicon surfaces terminated with functional groups such as carboxy (-COOH), –(amine) NH_2, or hydroxyl (–OH) are needed. To prepare ω-functionalized monolayers, the reactivities of various functional groups toward silicon must be considered. For example, carboxylic acids, alcohols, amines, and aldehydes have been reported to react with hydrogen-terminated silicon.[1b, 8-9] For the reaction between bifunctional molecules (e.g., ω–alkenoic acids) and a silicon surface, it could presumably result in two different orientations on the substrate (Figure 4.1). To ensure a monolayer with the desired orientation, various protecting/deprotecting protocols have been examined.[4, 10, 11-14] For example, the reaction of phthalimide- or acetamide-protected ω-amino-1-alkenes with silicon followed by deprotection successfully creates amino-terminated monolayers.[11] Similarly, carboxy-terminated surfaces can be prepared by hydrolyzing ester-terminated monolayers. The hydrolysis is facilitated by either hydrochloric acid[10, 12] or potassium tert-butoxide.[4, 13-15] Nevertheless, the acid-catalyzed reaction is usually incomplete, and the strongly basic potassium tert-butoxide severely

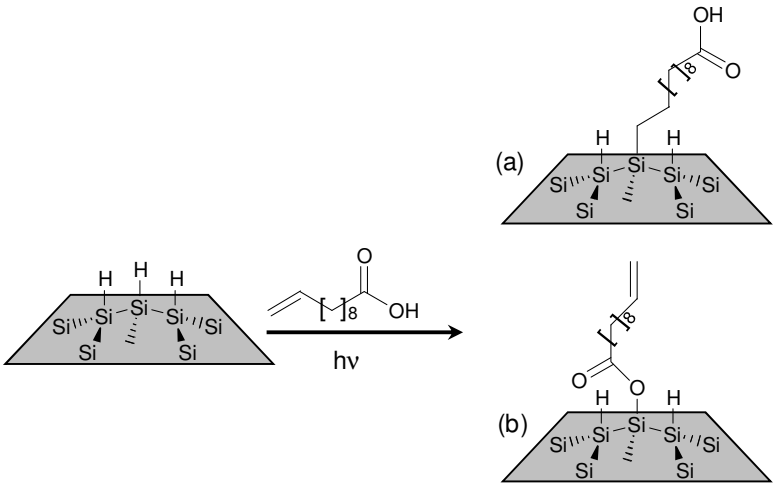

Figure 4.1 Schematic illustration of the two possible orientations when undecylenic acid reacts with hydrogen-terminated silicon (H-Si): (a) $–CH=CH_2$ has reacted, (b) –COOH has reacted.

damages the monolayer structure.[14] In the past, both methods have been commonly used for the preparation of carboxy-terminated silicon and for the fabrication of DNA microchips.[3, 4, 13, 16]

In this chapter, we report the results of our investigation of the photoreactivity of 1-dodecene ($CH_3(CH_2)_9CH=CH_2$), undecanoic acid ($CH_3(CH_2)_9COOH$) and undecylenic acid ($CH_2=CH(CH_2)_8COOH$) with hydrogen-terminated silicon (Si-H) under varied experimental conditions, in order to explore the feasibility of preparing high-quality carboxy-terminated silicon surfaces via one-step photochemical reaction. According to recent reports by Boukherroub et al.,[17-18] the thermal or microwave-assisted reactions of bifunctional molecules (e.g., undecylenic acid) with hydrogen-terminated *porous* silicon occurs selectively at the alkene terminus. The mechanism of microwave activation probably resembles that of thermally induced reactions, with the polarity of the molecules playing a major role.[19] Since the chemistry of *porous* silicon is generally similar to that of

flat silicon crystals,[20-22] we reasoned that the preparation of high-quality carboxy-terminated monolayers might be possible via a one-step photoreaction of undecylenic acid with Si-H under optimized reaction conditions.[23]

4.2 Experimental section

4.2.1 Materials

All chemicals were of reagent or the highest available commercial grade quality and used as received, unless otherwise stated. Deionized water (>18.3 MΩ·cm) was obtained from a Barnstead EasyPure UV/UF compact water system (Dubuque, IA). 1-Dodecene (98%), undecylenic acid (98%), undecanoic acid (99%), and ethyl undecylenate (97%) were purchased from Aldrich (Milwaukee, WI); tetrahydrofuran (THF) and 1,1,1-trichloroethane (99.5%) from Caledon Laboratories Ltd. (Georgetown, ON); ammonium fluoride (40%), sulfuric acid (96%), and hydrogen peroxide (30%) from GEM Microelectronic Materials Inc. (Chandler, AZ). 1-Dodecene was redistilled from sodium under reduced pressure (20-30 Torr); ethyl undecylenate was purified by passing through an activated Al_2O_3 column.

4.2.2 Sample preparation

Silicon (111) wafers (0.5-5.0 Ω·cm, n-type, Virginia Semiconductor Inc.) and Attenuated total reflectance (ATR) silicon crystals (25 × 5 × 1 mm^3, Harrick Scientific Inc.) were cleaned and etched as previously mentioned (Chapter 3.2.3). The fresh H-Si

samples were transferred under argon into Schlenk tubes containing 2-3 mL of deoxygenated neat 1-dodecene, ethyl undecylenate, undecylenic acid, or undecanoic acid. They were irradiated in a UV photoreactor (350 nm, 112W, model LZC-TIM300, Luzchem Research Inc., Ottawa, ON) for the desired period of time. The undecanoic acid (m.p. 26°C) was kept in the liquid state by moderate heating during the irradiation.

The modified silicon samples were then rinsed at room temperature with THF, trifluoroacetic acid solution in THF (1%), and finally with 1,1,1-trichloroethane before characterization. The carboxy-terminated samples were further rinsed with diluted HCl before characterization to avoid possible deprotonation. The hydrolysis of ester-terminated monolayers (formed from the reaction of ethyl undecylenate with H-Si) was carried out by immersion in 2.0 M HCl at 70º C for 2 hours.

4.2.3 Surface characterization

ATR-FTIR and wetting measurements were performed as described in Chapter 3.2.4. Contact angles were measured for three independent samples (4-5 readings at different spots per sample) with 2.0-μL drops of deionized water. Ellipsometric measurements were performed with a Gaetner variable angle ellipsometer (model L116B) using a helium-neon laser at an incident angle of 70°. The thickness of the monolayers on silicon were determined by assuming an index of refraction of 1.46.

A custom-made atomic force microscope (AFM) with a silicon nitride tip (Triangular D of MSCT-AUHW, Veeco Metrology group, force constant 0.03 N/m, resonance frequency 15 kHz) was used in contact mode to obtain the topographic image

of the silicon surfaces modified with different monolayers. High-resolution electron energy loss spectroscopy (HREELS) was carried out at NRC-SIMS in an ultrahigh vacuum system equipped with an LK3000 spectrometer (LK technologies, Bloomington, IN) operating at a nominal resolution of 35 cm^{-1}.

4.3 Results and Discussion

4.3.1 Photoreactivity of different terminal groups: Alkene versus Carboxy

Ultraviolet (UV) irradiation of freshly prepared H-Si (111) crystals in the presence of n-alkenes results in the formation of alkyl monolayers covalently bound to silicon via Si-C bonds.[25] Reactions were typically carried out under inert atmosphere, and the irradiation time has been arbitrarily set as 3 to 5 hours, as no dependence of the film quality was discernible under these typical experimental conditions. It has also been reported that carboxylic acids react with both porous silicon and silicon crystals under UV irradiation and anodic polarization.[9, 26] To provide a direct comparison between the photoreactivities of these two functional groups (particularly in case of bifunctional molecules, e.g., ω-alkenoic acids, were used for the modification) toward H-Si, we examined the monolayers formed from undecylenic acid, undecanoic acid and 1-dodecene under the typical reaction conditions, i.e., 4 hours under UV irradiation at 350 nm.

As shown in Figure 4.2(a), the major peaks of the monolayer formed from undecylenic acid in the region between 3500-2500 cm^{-1} can be assigned to the

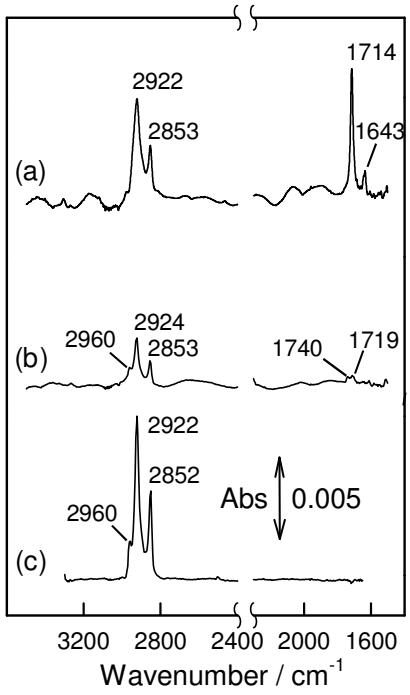

Figure 4.2 ATR-FTIR spectra of H-Si (111) crystals after reactions with neat (a) undecylenic acid, (b) undecanoic acid, and (c) 1-dodecene, under UV irradiation (350 nm) for 4 hours.

asymmetric ($\nu_{as}(CH_2)$ at 2922 cm^{-1}) and symmetric ($\nu_s(CH_2)$ at 2853 cm^{-1}) methylene stretches, respectively. As the rigidity of the material increases, it has been suggested that the wavenumber of $\nu_{as}(CH_2)$ shifts from 2928 (liquid state) to 2919 cm^{-1} (crystal phase);[27] the above value ($\nu_{as}(CH_2)$ at 2922 cm^{-1}) is comparable to that reported for alkyl monolayers on silicon.[1, 10, 14] This result indicates that the monolayer formed from undecylenic acid is relatively closely packed, although it is clearly not as ordered and compact as long-chain alkanethiolate monolayers on gold (for which the $\nu_{as}(CH_2)$ would appear at a much shorter wavenumber, 2917-9 cm^{-1}).[28] The other strong band at 1714 cm^{-1} in the spectrum of Figure 4.2(a) is due to the carbonyl stretch arising from either –COOH at the surface or from an ≡Si-O-C(O)-R ester vibration (Figure 4.1).[29] Of

particular interest to us was the alkene (-CH=CH_2) stretch at 1634 cm^{-1},[30] which suggests that both ends of the molecule are reactive toward H-Si (Figure 4.1). However, the intensity and appearance of this peak varied from sample to sample, indicating that the reaction depends sensitively on the exact experimental conditions.

The IR spectrum of the monolayer obtained from undecanoic acid under the same reaction conditions, Figure 4.2(b), features three CH stretching bands (CH_3 at 2960 cm^{-1}, CH_2 at 2924 and 2853 cm^{-1}) and a split band (1740 and 1719 cm^{-1}) for the carbonyl stretch that is weak but discernible. In comparison to the silicon surface modified with undecylenic acid (Figure 4.2a), the absolute absorbances of the CH_2 bands are much weaker in Figure 4.2(b), indicating a low surface density of this monolayer. The broadened peak shapes and higher wavenumbers further support this hypothesis. The -C=O vibration is probably due to ≡Si-O-C=O ester, although the low signal-to-noise ratio in this region makes this assignment ambiguous. Figure 4.2(c) shows that under identical conditions (irradiation at 350 nm for 4 hours) 1-dodecene yields closely packed monolayers, as indicated by the sharp and intense CH_2 stretches. Besides serving as a control experiment, it shows that neither undecylenic acid nor undecanoic acid can form monolayers of the same high quality on silicon under UV irradiation. Using the intensity of the CH_2 asymmetric stretch modes as a quantitative measure of surface coverage, we can estimate that reaction with undecylenic acid results in a monolayer with ~75% of the coverage obtained with 1-dodecene. In contrast, reaction with undecanoic acid results in a monolayer with only ~35% of that obtained with 1-dodecene.

Wetting measurements provide valuable information about surface polarity and they are very useful and convenient for monitoring surface modifications. As shown in

Table 4.1, the water contact angle decreases significantly (from 78 ± 5° to 64 ± 2°) upon reacting the silicon surface with undecylenic acid under UV irradiation, although this surface is more hydrophobic than that prepared via ester hydrolysis (54 ± 2°), i.e., the formation of ester-terminated monolayers on silicon followed by hydrolysis under acidic conditions.[4, 10, 12-14] This may be due to the reaction of this bifunctional molecule with H-Si from either end, as shown in Figure 4.1, with some alkene groups protruding to the surface. In comparison, the value of 52 ± 2° for silicon modified with undecanoic acid indicates that the resulting surface is more hydrophilic, which is surprising because it suppose to be terminated with methyl groups (and therefore hydrophobic, as a result of the reaction between the carboxy terminus and H-Si). In fact, our ellipsometric measurements also showed irregularity in this system; the film thickness was determined to be 14.3 ± 1.0 Å, which is unreasonably high with respect to the molecular length. In contrast, monolayers made from undecylenic acid and from 1-dodecene have more reasonable thicknesses (Table 4.1).[10, 14]

AFM images revealed characteristic differences in the morphologies of the silicon

System	Contact Angle / degree	Thickness / Å
H-Si (111)	78 ± 5	n/a
Undecylenic acid	64 ± 3	11.6 ± 1.0
Undecanoic acid	52 ± 5	14.3 ± 1.0
1-Dodecene	104 ± 2	14.2 ± 1.0

Table 4.1 Water contact angles and optical elllipsometric thicknesses of the monolayers formed on silicon by UV irradiation (4 hours).

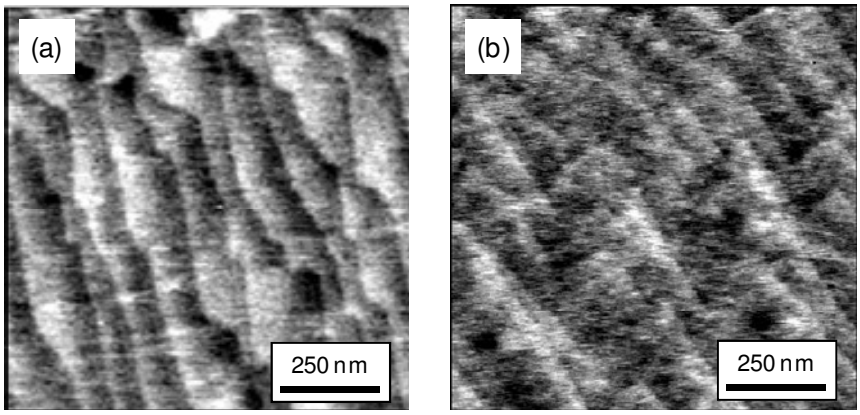

Figure 4.3 Contact mode AFM images of H-Si (111) after reaction with (a) undecylenic acid and (b) undecanoic acid under UV irradiation for 4 hours.

surfaces modified with the three different molecules. As shown in Figure 4.3(a), the reaction with undecylenic acid did not change the microscopic topography from that of the hydrogen-terminated surface: atomically flat terraces with monoatomic steps. In contrast, the surface modified with undecanoic acid, Figure 4.3(b), shows the disappearance of some of the step definitions but also higher surface roughness. This generally indicates incomplete reaction and oxidation / contamination.[31] Together with the IR data which showed a low coverage of alkyl chains on the surface in this case, we can conclude that the reaction with undecanoic acid results in considerable oxidation of the surface, accounting for the high hydrophilicity and excess film thickness observed on these surfaces. HREELS spectra (not shown) also indicate substantial oxidation of the surface.

4.3.2 Kinetic control of the reaction of H-Si with bifunctional molecules

The ATR-FTIR data (Figure 4.2) clearly demonstrate that both alkene and carboxy functional groups react with H-Si (111), and that bifunctional molecules (e.g., undecylenic acid) react at either end (Figure 4.1). However, the photoreactivitities of the two functional groups under equilibrated experimental conditions (4 hours of reaction time) are very different: the reaction of H-Si (111) with n-alkenes and their derivatives yields closely packed monolayers, while alkanoic acids react slowly and incompletely, resulting in partial oxidation of the substrate. To explore the possibility of preparing carboxy-terminated monolayers on silicon from ω-alkenoic acids via direct photochemical reaction, we initiated kinetic studies by monitoring the water contact angle changes as a function of the time of UV irradiation.

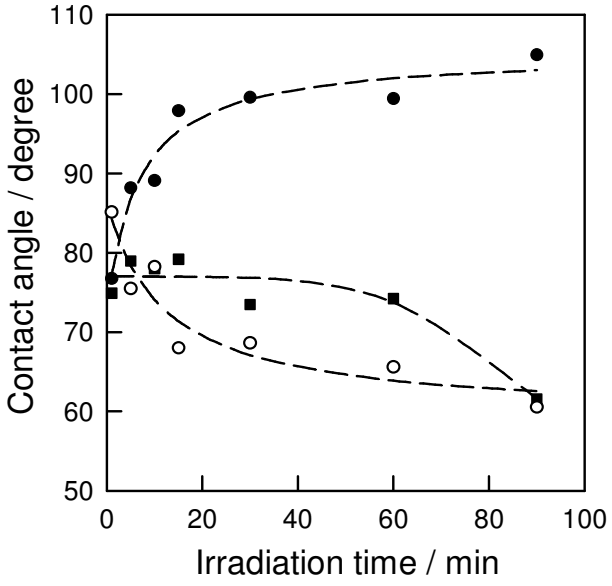

Figure 4.4 Water contact angles on H-Si (111) as a function of the time of UV irradiation upon reaction with neat 1-dodecene (●), undecanoic acid (■), and n-octane (○). The dashed lines are to direct the eye only.

As shown in Figure 4.4, the changes of water contact angles on H-Si (111) surfaces after reactions with 1-dodecene and undecanoic acid follow very different trends. For the former, the angle initially increases with increased UV irradiation time and reaches a maximum after approximately 60 min. The time scales are similar to those observed by Cicero et al. for the photoreactions of various alkenes, although the experimental conditions are quite different in terms of the UV wavelength, distance, and power.[25] In contrast, the contact angle on silicon surface after reaction with undecanoic acid remained almost constant for the first 60 min and then decreased gradually. When the H-Si (111) surface was irradiated in the presence of n-octane for control purposes, the contact angle was found to drop immediately and reach a constant value after 90 min. It has been confirmed by Mitchell that H-Si can be oxidized under UV irradiation at 185/254 nm,[32] while Ye et al. reported that the photooxidation also happens at higher wavelengths (532nm and 1064nm).[33] We hypothesize that initially the reaction of undecanoic acid with silicon competes with oxidation (by the trace amount of O_2/water present in the reactants); therefore, the contact angle should not decrease significantly. When the irradiation time is prolonged, oxidation becomes dominant and the contact angle decreases as the silicon surface becomes more hydrophilic upon oxidation. The kinetic data shown in Figure 4.4 indicate that the reaction of H-Si with alkene groups is much faster than that with carboxy groups; the time scale for the formation of the monolayers is much shorter than the irradiation time conventionally used (3 to 5 h).[12, 14]

A different approach was taken with undecylenic acid whose reaction with H-Si does not lead to significant contact angle changes (see Table 1.1). We monitored this reaction by IR spectroscopy and plotted the wavenumber of $\nu_{as}(CH_2)$ as a function of UV

irradiation time (Figure 4.5). As mentioned previously, this band is an indication of the molecular packing of the monolayers: the shorter the wavenumber, the more closely packed the monolayers (i.e. the more rigid the organic film). Following an initial decrease, the wavenumber reached a minimum after about 90 min (Figure 4.5), indicating that the reaction time can be substantially shortened without sacrificing the quality of the monolayers. More importantly, the shortened reaction time also limits the reaction at the carboxy terminus of the bifunctional molecule.

Considering the above observations, the optimal duration of UV irradiation for the reaction of H-Si with ω-alkenoic acids appears to be between 90 min and 3 h. Figure 4.6 compares the ATR-FTIR spectra of the carboxy-terminated surfaces prepared by direct

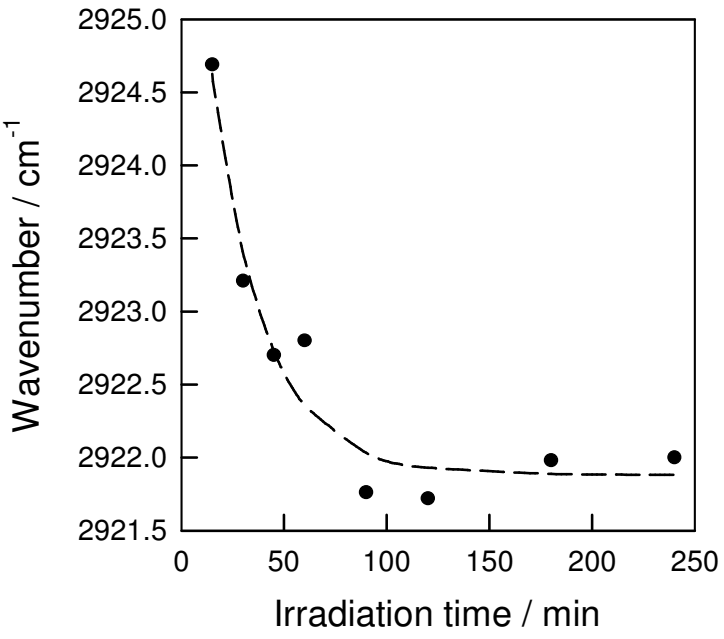

Figure 4.5 Wavenumber of methylene asymmetric stretch as a function of reaction time. The data points are from the ATR-FTIR spectra of H-Si (111) crystals reacted with undecylenic acid under UV irradiation for the indicated period of time.

reaction with undecylenic acid under controlled conditions (3 hours UV irradiation) prepared via the hydrolysis route, indicating that the multi-step reactions (particularly the hydrolysis using acids) may remove some of the alkyl chains from the surface.[14] We also observed a sharp peak for the carbonyl stretch at 1712 cm^{-1} for Figure 4.6(a), in contrast to the relatively weaker and split band at 1715 cm^{-1} (with a shoulder peak at 1743 cm^{-1}) in Figure 4.6(b). More importantly, no alkene stretch (~1640 cm^{-1}) is discernable; indicating that reaction of the carboxy terminus with the silicon surface is negligible when the UV irradiation time is shortened. This demonstrates that monolayers with exclusive carboxy termination can be prepared from ω-alkenoic acids in one step by optimizing the UV irradiation time. As noted previously, the potential of direct attachment of ω-alkenoic acids is significant, as it does not require the additional reaction

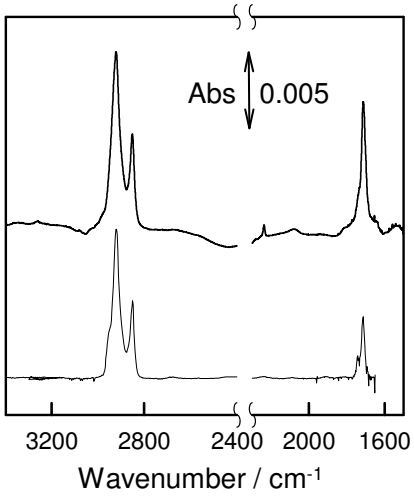

Figure 4.6 ATR-FTIR spectra of carboxy-terminated monolayers on silicon prepared via (a) photoreaction of H-Si(111) with undecylenic acid after 3.5 hours of UV irradiation; (b) hydrolysis of $\equiv Si\text{-}(CH_2)_{10}COOCH_2CH_3$.

step (e.g., hydrolysis). This finding shortens the process en route to a biofunctionalized semiconductor surface.

We further examined the quality of the ω-carboxy monolayers formed from the photochemical reaction of undecylenic acid with H-Si by HREELS (High resolution electron energy loss spectroscopy). Figure 4.7(a) shows the spectrum obtained with controlled UV irradiation time (3.5 hours). The key bands corresponding to the ω-carboxy groups, i.e., C=O stretching (1715 cm^{-1}) and O-H bending vibrations (940 cm^{-1}) are evident.[34] A very weak residual Si-H stretch at 2080 cm^{-1} indicating minimal oxygen insertion into Si-Si back-bonds. The absence of large peaks between 1060 and 1100 cm^{-1} further confirms that the oxidation of the samples was not significant. We also found that UV irradiation will induce unfavourable changes to the monolayers. As shown in Figure 4.7 (b), the spectra obtained after irradiation for 12 hours indicates substantial differences in the structure compared with shorter irradiation time. Most notable is the new peak at 1250 cm^{-1} (likely corresponding to the Si-O-C stretch)[29-30] and the decrease in the intensity of C-H stretch mode (at 2920 cm^{-1}). These observations are consistent with those of Uosaki and co-workers who have reported degradation of alkyl monolayers on silicon upon prolonged exposure to UV.[35]

The reaction mechanisms may be the key to answering the question of why the kinetics of photochemical reactions of H-Si(111) with different functional groups (alkene vs. carboxy) are substantially different. Boukherroub et al. proposed the addition of aldehydes to H-Si surfaces may be initiated by a nucleophilic attack,[36] which is different from the generally accepted, radical mechanism for the addition of alkenes.[25, 31, 37] It is likely that the addition of the carboxy group to H-Si resembles that of the aldehyde.

However, the mechanisms underlying these surface reactions remain perplexing and they are still under intensive investigations / discussions.[38-39] Recently, Zuilhof and co-workers have reported the successful attachment of unsaturated compounds to H-Si

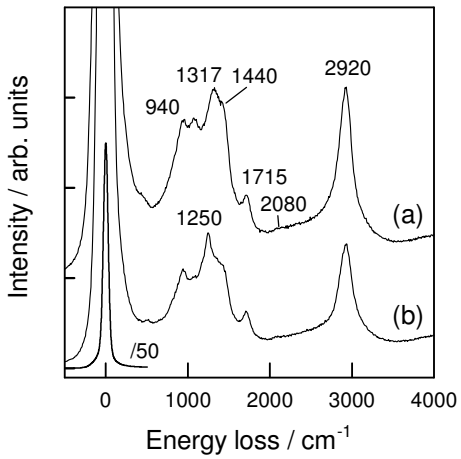

Figure 4.7 HREELS spectra of carboxy-terminated monolayers on silicon prepared via photoreaction of H-Si(111) with undecylenic acid under UV irradiation for 3. 5 (a) and 12 hours (b), respectively. The incident energy was 6 eV and the inelastic losses have not been normalized to the elastic peak.

Energy loss (cm^{-1})	**Assignments**
940	C-O-H bending (dimeric)
1317	CH_2 wagging, C-OH stretching
1440	CH_2 scissoring, C-O-H bending
1715	C=O stretching
2080	Si-H stretching
2920	C-H stretching

Table 4.2 Energy loss (cm^{-1}) and assignments of the major bands in the HREELS spectra of hydrogen-terminated silicon reacted with undecylenic acid under UV irradiation.

utilizing visible light (447 nm),[40-41] a much higher wavelength than the required 354 nm to excite and break a Si-H bond.[25, 31] They have hypothesized an alternative mechanism involving surface Plasmon for the reaction between alkenes and H-Si.[40] Nevertheless, all above investigations suggests that the reaction mechanisms under different initiation conditions (photochemical, thermal, or microwave irradiation) may also be different from each other.[42]

4.4 Conclusion

The photoreactivities of undecylenic acid, undecanoic acid, and 1-dodecene toward hydrogen-terminated silicon were investigated by ATR-FTIR, wetting measurements, ellipsometry, AFM, and HREELS. Both termini of the bifunctional molecule (e.g., undecylenic acid) were found to be reactive, but the alkene reacts substantially faster than the carboxy group. By optimizing the UV irradiation time, it is possible to prepare high quality ω-carboxy functionalized silicon surface by minimizing the reaction between the carboxy terminus and H-Si. More importantly, carboxy-terminated monolayers prepared by this one-step photochemical process are comparable in term of surface coverage and molecular packing to those obtained by the reaction between H-Si and ethoxy undecanoate and subsequent hydrolysis.

4.5 Bibliography

(1) (a) Linford, M. R.; Chidsey, C. E. D. *J. Am. Chem. Soc.* **1993**, *115*, 12631. (b) Linford, M. R.; Fenter, P.; Eisenberger, P. M.; Chidsey, C. E. D. *J. Am. Chem. Soc.* **1995**, *117*, 3145.

(2) (a) Liu, Y. J.; Yu, H. Z. *ChemPhysChem* **2002**, *3,* 799-801. (b) Liu, Y. J.; Yu, H. Z. *ChemPhysChem* **2003**, *4*, 335. (c) Liu, Y. J.; Yu, H. Z. *J. Phys. Chem. B* **2003**, *107*, 7803.

(3) Lin, Z.; Strother, T.; Cai, W.; Cao, X.; Smith, L. M.; Hamers, R. J. *Langmuir* **2002**, *18*, 788.

(4) Strother, T.; Cai, W.; Zhao, X.; Hamers, R. J.; Smith, L. M. *J. Am. Chem. Soc.* **2000**, *122*, 1205.

(5) Willner, I.; Katz E. *Angew. Chem. Int. Ed.* **2000**, *39*, 1180.

(6) Lasseter, T. L.; Clare, B. H.; Abbott, N. L.; Hamers. R. J. *J. Am. Chem. Soc.* **2004**, *126*, 10220.

(7) Pike, A. R.; Lie, L. H.; Eagling, R. A.; Ryder, L. C.; Patole, S. N.; Connolly, B. A.; Horrocks, B. R.; Houlton, A. *Angew. Chem. Int. Ed.* **2002**, *41*, 615.

(8) Pike, A. R.; Patole, S. N.; Murray, N. C.; Ilyas, T.; Connolly, B. A.; Horrocks, B. R.; Houlton, A. *Adv. Mater.* **2003**, *15*, 254.

(9) Effenberger, F.; Götz, G.; Bidlingmaier, B.; Wezstein, M. *Angew. Chem. Int. Ed.* **1998**, *37*, 2462.

(10) Sieval, A. B.; Demirel, A.L.; Nissink, J. W. M.; Linford, M. R.; Van der Maas, J. H.; De Jeu, W. H.; Zuilhof, H.; Sudhölter, E. J. R. *Langmuir* **1998**, *14*, 1759.

(11) Sieval, A. B.; Linke, R.; Heij, G.; Meijer, G.; Zuilhof, H.; Sudhölter, E. J. R. *Langmuir* **2001**, *17*, 7554.

(12) Boukherroub, R.; Wayner, D. D. M. *J. Am. Chem. Soc.* **1999**, *121*, 11513.

(13) (a) Wei, F.; Zhao, X. S. *Thin Solid Films* **2002**, *408*, 286. (b) Wei, F.; Sun, B.; Guo, Y.; Zhao, X. S. *Biosensors and Bioelectronics* **2003**, *18*, 1157. (c) Wei, F.; Sun, B.; Liao, W.; Ouyang, J.; Zhao, X. S. *Biosensors and Bioelectronics* **2003**, *18*, 1149.

(14) Liu, Y.-J.; Navasero, N. M.; Yu, H.-Z. *Langmuir* **2004**, *20*, 4039.

(15) Gassman, P. G., Schenk, W. N. *J. Org. Chem.* **1977**, *42*, 918.

(16) Strother, T.; Hamers, R. J.; Smith, L. M. N. *Nucleic Acids Res.* **2000**, *18*, 3535.

(17) Boukherroub, R.; Wojtyk, J. T. C.; Wayner, D. D. M.; Lockwood, D. J. *J. Electrochem. Soc.* **2002**, *149*, H59.

(18) Boukherroub, R.; Petit, A.; Loupy, A.; Chazalviel, J.-N.; Ozanam, F. *J. Phys. Chem. B* **2003**, *107*, 13459.

(19) Perreux, L.; Loupy, A. *Tetrahedron* **2001**, *57*, 9199.

(20) Lee, E. J.; Ha, J. S.; Sailor, M. J. *J. Am. Chem. Soc.* **1995**, *117*, 8295.

(21) Kim, N. Y.; Laibinis, P. E. *J. Am. Chem. Soc.* **1997**, *119*, 2297.

(22) Bateman, J. E.; Eagling, R. D.; Worrall, D. R.; Horrocks, B. R.; Houlton, A. *Angew. Chem. Int. Ed.* **1998**, *37*, 2683.

(23) Wayner and co-workers reported their independent study of photochemical preparation of carboxy-terminated monolayers from the reaction between undecylenic acid and hydrogen terminated silicon, (Voicu, R.; Boukherroub, R.; Bartzoka, V.; Ward, T.; Wojtyk, J. T. C.; Wayner, D. D. M. *Langmuir* **2004**, *20*, 11713-11720). In contrast to the kinetic studies reported herein, their paper was focused on the patterning and immobilization of DNA on silicon via simple surface activation reactions. It is different in nature but it adds to the field where our work also strengthens.

(24) Kern, W.; Puotinen, D. A. *RCA Rev.* **1970**, *31*, 188.

(25) Cicero, R. L.; Linford, M. R.; Chidsey, C. E. D. *Langmuir* **2000**, *16*, 5688.

(26) Lee, E. J.; Bitner, T. W.; Ha, J. S.; Shane, M. J.; Sailor, M. J. *J. Am. Chem. Soc.* **1996**, *118*, 5375.

(27) Snyder, R. G.; Strauss, H. L.; Elliger, C. A. *J. Phys. Chem.* **1982**, *86*, 5145.

(28) Ulman, A. *An Introduction to Ultrathin Organic Films, from Langmuir-Blodegett to Self-Assembly,* Academic Press: Boston, **1991**.

(29) Smith, A. L. *Analysis of Silicones*, John Wiley & Sons: New York, **1974**. p. 271.

(30) Silverstein, R. M.; Webster, F. X. *Spectrometric Identification of Organic Compounds,* 6th ed.; John Wiley & Sons, Inc.: New York, **1998,** pp. 84-85.

(31) Boukherroub, R.; Morin, S.; Bensebaa, F.; Wayner, D. D. M. *Langmuir* **1999**, *15*, 3831.

(32) Mitchell, S. A. *J. Phys. Chem. B* **2003**, *107*, 9388.

(33) Ye, S.; Saito, T.; Nihonyanagi, S.; Uosaki, K.; Miranda, P. B.; Kim, D.; Shen, Y.-R. *Surf. Sci.* **2001**, 476, 121.

(34) Magnée, R.; Maazouz, M.; Doneux, C.; Bodino, F.; Rudolf, P.; Teillet-Billy, D.; Pireaux, J. -J. *J. Phys. Chem. B.* **2003**, *107*, 4567.

(35) Uosaki, K.; Quayum, M. E.; Nihonyanagi, S.; Kondo, T. *Langmuir* **2004**, *20*, 1207.

(36) Boukherroub, R.; Morin, S.; Sharpe, P.; Wayner, D. D. M. *Langmuir* **2000**, *16*, 7429.

(37) Bateman, J. E.; Eagling, R. D.; Horrocks, B. R.; Houlton, A. *J. Phys. Chem. B* **2000**, *104*, 5557.

(38) Cucinotta, C. S.; Ruini, A.; Caldas, M. J.; Molinari, E. *J. Phys. Chem. B* **2004**, *108*, 17278.

(39) Takeuchi, N.; Kanai, Y.; Selloni, S. *J. Am. Chem. Soc.* **2004**, *126*, 15890.

(40) Sun, Q.-Y.; de Smet, L. C. P. M.; van Lagen, B.; Wright, A.; Zuilhof, H.; Sudhölter, E. J. R. *Angew. Chem. Int. Ed.* **2004**, *43*, 1352.

(41) de Smet, L. C. P. M.; Stork, G. A.; Hurenkamp, G. H. F.; Sun, Q.-Y.; Topal, H.; Vronen, P. J. E.; Sieval, A. B.; Wright, A.; Visser, G. M.; Zuilhof, H.; Sudhölter, E. J. R. *J. Am. Chem. Soc.* **2003**, *125,* 13916.

(42) Eves, B. J.; Sun, Q.-Y.; Lopinski, G. P.; and Zuilhof, H. *J. Am. Chem. Soc.* **2004**, *126*, 14318.

Chapter 5. Preparation and structural evaluation of DNA monolayers on silicon

Building upon the finding presented in Chapter 4, herein the preparation of DNA monolayers on silicon and the subsequent structural characterization will be described. Since nucleic acids possess charged phosphate groups in their backbones, the presence of counter-ions to reduce the repulsive Coulombic interactions between the strands is vital. It is important to evaluate how different mono- and divalent metal cations influence the molecular orientations of DNA molecules on silicon surfaces upon immobilization and hybridization. Sum-frequency generation (SFG) spectroscopy studies demonstrated that the degree of conformational variation of DNA self-assembled monolayers on silicon depends on the type of metal cations present. The molecular orientation change of immobilized single-stranded oligonucleotides correlates with DNA-cation affinity ($Mg^{2+} > Ca^{2+} > K^{+} \sim Na^{+}$): metal cations with the strongest affinity disrupt the structure of the underlying linker-monolayer the most. Upon hybridization the trend is reversed, which may be due to the greater ability of divalent cations (e.g., Mg^{2+}) to mask the negative charges on the DNA backbone. These findings provide useful information for the construction of more sensitive DNA biosensors, and particularly for the optimization of on-chip hybridization performance.

5.1 Introduction

DNA helices are negatively charged polyelectrolytes that will associate with cations to reduce the repulsive Coulombic interactions between the phosphate groups within and between the strands. The cations may induce deformation (bending, twisting, and changing of groove-widths) as well as condensation of DNA strands even at short length.[1-3] The type, concentration and degree of hydration of the cations will affect their affinities for the binding sites and play a crucial role in governing the structure, stability and reactivity of nucleic acids (DNA/RNA).[2-12] Extensive experimental and theoretical investigations have been carried out with solvated and crystalline DNA,[1-14] but little is known to date about the influence of different cations on the molecular conformations and on the hybridization reactivity of oligonucleotide strands immobilized on solid surfaces .

DNA monolayers on various substrates (e.g., gold[15] and silicon[16-21]) prepared via self-assembly are the basis for the fabrication of chip-based DNA biosensors.[22-24] The attachment of oligonucleotides onto oxide-free silicon has attracted considerable attention in the past several years because crystalline semiconductors are atomically flat and their surface structures are well-defined. The use of common commercially available semiconductors will eventually permit the use of existing microelectronics technology for

the fabrication of these semiconductor-based biochips.[25, 26] According to the protocol reported by Strother et al.,[18] single-stranded DNA (ssDNA) can be electrostatically immobilized onto silicon using cross-linker molecules on ω-carboxyl monolayers. Covalent anchoring has also been proposed, either via the formation of amide linkages to amine-functionalized DNA,[16, 20-21] or via on-chip DNA synthesis starting from an ω-undecanol monolayer.[17] These pioneering studies have focused on DNA attachment strategies, surface patterning methods, and detection techniques.[16-21] In contrast, the structure and physical behaviour of DNA strands and their interactions on silicon surfaces have not yet been thoroughly investigated. The results would be of practical importance for the optimization of DNA hybridization arrays[23] and the design of other types of DNA-based biosensors.[24]

In order to investigate the conformations of immobilized DNA strands on microarray chips, surface-sensitive techniques capable of probing the molecular order must be employed. Herein, we explore the application of sum frequency generation (SFG) spectroscopy to probe the structure and behaviour of DNA self-assembled monolayers (SAMs) on silicon, in particular the effect of metal cations on the immobilization and hybridization processes. SFG spectroscopy is based on a second-order nonlinear optical effect of a photon generated at a frequency equal to the sum of the frequencies of two incident light beams, often infrared and visible, to induce specific vibrations at buried interfacial sites. According to the electric dipole approximation, second-order optical effects are prohibited in media exhibiting inversion symmetry, therefore, SFG is an extremely sensitive technique capable of revealing molecular conformations at interfaces.[27-29] Stokes et al. have recently communicated their pioneered

investigation of DNA monolayers on glass by SFG,[30] in which DNA strands rich in thymine (e.g., poly-AT) were used in the measurements. In such cases, the investigation of cation-DNA interactions is not feasible because the binding of counter-ions is sequence-specific.[1]

Our approach is to monitor the underlying linker layer instead of the rather weak signals generated by the DNA strands, which allows us to probe any sequence of interest. In particular, a carboxyl-terminated linker monolayer was prepared by reacting hydrogen-terminated silicon (≡Si-H) with a mixture of 1-decene (CH_2=CH(CH_2)$_7$$CH_3$) and undecylenic acid ($CH_2$=CH($CH_2$)$_8$COOH), to which amino-terminated DNA strands were attached via amide coupling.[19] Because SFG is extremely sensitive to methyl groups at the surface, e.g., it can be used to monitor the surface hydrolysis reactions of ester-terminated monolayers.[31] In the mixed monolayer, the n-alkyl chains will essentially act as excellent "molecular probes". We expected that the structure of this underlying mixed monolayer would be disturbed if the immobilized DNA strands experienced substantial conformational changes. In other words, by examining the molecular order of the alkyl chains in the linker monolayer, we would be able to reveal the structural properties of DNA SAMs on silicon upon immobilization and after hybridization.

5.2 Experimental

5.2.1 Materials

All chemicals were of ACS reagent grade quality and used as received, unless otherwise stated. Deionized water (Milli-Q, >18.3 MΩ·cm) was used throughout the

experiments. 1-Decene (94%), undecylenic acid (98%), N-hydroxysuccinimide (NHS), 1-ethyl-3-(3-dimethylaminopropyl)-carbodiimide hydrochloride (EDC) and 1,1,1-trichloroethane (99.5%) were purchased from Aldrich Japan (Tokyo, Japan); tetrahydrofuran (THF), methanol (99.0%), ethanol (99.0%), propanol (99.0%), sulfuric acid (96%), and hydrogen peroxide (30%) from Wako Pure Chemical Industries (Osaka, Japan); ammonium fluoride (40%) from Morita Chemical Industries (Osaka, Japan); the amine-functionalized oligonucleotide (5'-NH_2-$(CH_2)_6$-TCGATCTGACGTCAGTC-AAA-3') and the complementary strand (3'-AGCTAGACTGCAGTCAGTTT-5') were ordered from Sigma Genosys Japan (Tokyo, Japan). 1-Decene was distilled from sodium under reduced pressure (20-30 Torr); undecylenic acid was purified by passing through an activated Al_2O_3 column.

5.2.2 Surface preparation

The procedure for the surface preparation (the attachment of linker layer, surface activation, and the immobilization of single-stranded DNA) is shown in Figure 5.1. Silicon (111) wafers (3.0-5.0 Ω·cm, n-type, donated by Shin-Etsu Semiconductors, Tokyo, Japan) were cleaned and etched as previously mentioned (Chapter 3.2.3).. The fresh ≡Si-H samples were transferred under argon into Schlenk tubes containing 2-3 mL of a deoxygenated mixture of 1-decene and undecylenic acid (9:1 molar ratio) and heated at 160 °C for 3.5 h. The modified silicon samples were then rinsed at room temperature with THF and 1,1,1-trichloroethane. Esterification of the carboxyl groups with NHS was carried out by exposing the sample to a phosphate buffer (pH 6.5) containing 0.2 M NHS and 0.6 M EDC for approximately 2 h; the surface was then rinsed with water.

Amine-functionalized DNA (20 μM; 5'-NH_2-C_6-TCGATCTGACGTCAGTCA AA-3') in 50 mM HEPES (4-(2-hydroxyethyl)-1-piperazineethanesulfonic acid) buffer and 20 mM saline solution (NaCl, KCl, $CaCl_2$ or $MgCl_2$) was reacted with NHS-terminated monolayers on silicon for 4 h. After immobilization, the surface was washed with 2% Tween 20 in HEPES and water. Hybridization was carried out with 20 μM complementary DNA (3'-AGCTAGACTGCAGTCAGTTT-5') in the same buffer overnight at room temperature. After the hybridization, the surface was washed thoroughly with the HEPES buffer and water.

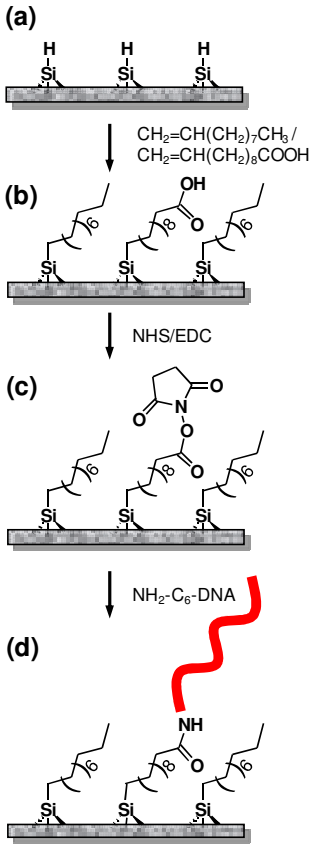

Figure 5.1 Schematic illustration of the preparation of DNA SAMs on silicon.

5.2.3 Surface characterization

The description of SFG setup is available in Chapter 3.2.4. All the spectra were obtained under ppp polarization. The equations presented previously (Chapter 3: equations 1 and 2) were used to express the SFG intensity. The obtained amplitude of the vibration mode (A_n) was used to calculate peak intensity ratios, for which the uncertainty was derived from at least three individual spectra from independent samples. . The quality of the fit is judged by r^2 values that was at least 0.900 and above. The detailed description of fitting routine and the fitting parameters are described in Appendix II.

X-ray photoelectron spectroscopy (XPS) measurements were carried out with a Rigaku XPS-7000 spectrometer using an Mg K X-ray source (1253.9 eV). The take-off angle was 45° with respect to the sample surface. The pressure during analysis was ~ 5×10^{-7} Pa and all the peaks were normalized to the Si-2p peak (99.5 eV).

Wetting measurements were performed as described in Chapter 3.2.4. Ellipsometric measurements were made with an Uvisel spectroscopic ellipsometer (Horiba Jobin Yvon) over the range of 300 to 700 nm at an incident angle of 70°. All the experimental uncertainties reported for wetting, ellipsometric and SFG measurements are derived from at least three independent samples.

The surface densities of DNA were estimated by means of an electrochemical method that was developed in our laboratory.[32, 33] The procedure is based on the voltammetric response of surface-bound ruthenium hexamine, $[Ru(NH_3)_6]^{3+}$ (Figure 5.2); such redox molecules are incorporated into the negatively charged DNA monolayer through electrostatic interactions. The following equations were used for the estimation:

$$\boldsymbol{\Gamma_{Ru}} = \frac{\mathbf{Q}}{\mathbf{nF_cA_{electr}}} \quad (1)$$

$$\Gamma_{DNA} = \Gamma_{Ru}\left(\frac{z}{m}\right)N_A \quad (2)$$

in which Γ_{Ru} and Γ_{DNA} are the surface densities of the cationic complex and DNA, respectively; n is the number of electrons involved in the reaction, F_c is Faraday's constant, z is the charge of the cation, and m is the number of nucleotides per DNA. The surface area of the electrode, A_{electr}, is known and the charge, Q, is extracted from the area of the reduction peak.

Cyclic voltammetry was performed with an Autolab Electrochemical Analyzer (PGstat30, Eco Chemie BV, The Netherlands) in a Faraday cage. Silicon samples were pressed against an O-ring located at the bottom of a custom-designed three-electrode Teflon cell. The reference electrode was Ag/ AgCl/ 3M NaCl and the counter electrode was a Pt wire. Prior to the measurements, the samples were incubated with 2.5 μM $[Ru(NH_3)_6]^{3+}$ in 50 mM HEPES while degassed by argon gas for 15 min. The scan rate was 500 mV/s.

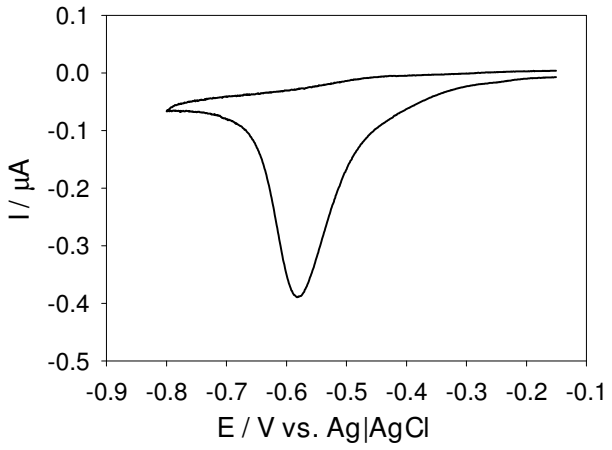

Figure 5.2 Representative cyclic voltammogram of $[Ru(NH_3)_6]^{3+}$ bound to ssDNA monolayer on silicon.

5.3 Results and Discussion

5.3.1 Structure of linker monolayer

To immobilize DNA probe strands on an oxide-free silicon surface, a linker monolayer terminated with carboxylic acid groups was prepared first (Figure 5.1). It has been shown that the monolayer prepared from a 9:1 binary mixture of 1-decene and undecylenic acid provides an optimal surface density (~2×10^{-11} mol/cm^2) of the acid groups for the immobilization of DNA probes,[37] if high hybridization efficiencies are desired.

It is essential to examine the structural properties of such linker monolayers before the surface activation and the subsequent attachment of DNA probes. Figure 5.3(a) shows the SFG spectrum of the linker monolayer prepared from the mixture of 1-decene and undecylenic acid (9:1), which resembles the spectral features of a densely packed and well oriented ≡Si-$(CH_2)_9CH_3$ monolayer (Figure 5.3b). [33, 34] Both spectra are

dominated by the characteristic peaks of the terminal methyl (-CH_3) groups: CH symmetric stretch (r^+), Fermi resonance between r^+ and CH bending overtone, and the CH asymmetric stretch (r^-) at ~2878 cm^{-1}, ~2940 cm^{-1}, and ~2964 cm^{-1}, respectively. The strong contributions from CH_3 groups and the absence of methylene (CH_2)-related peaks confirm that the mixed monolayer is well packed with an all-trans configuration of the alkyl chains.[33-36] Furthermore, the ellipsometric thickness of the mixed monolayer (11.9 ± 0.6 Å) is similar to that of ≡Si-$(CH_2)_9CH_3$ (11.8 ± 1.0 Å) alone, indicating comparable surface densities as well as average titling angles of Si-C bonded monolayers.[36] The presence of carboxyl groups on the mixed monolayer was confirmed by wetting measurements: it exhibited much lower water contact angles, 92.1 ± 1.3°, than the ≡Si-$(CH_2)_9CH_3$ monolayer, 108.6 ± 0.9° All the data for thickness and wetting measurements are summarized in Table 5.1 for direct comparison.

Upon NHS/EDC treatment to convert the carboxyl to NHS ester groups, weak symmetric (d^+) and asymmetric (d^-) CH_2 peaks arose at ~2850 cm^{-1}, ~2920 cm^{-1} and ~2902 cm^{-1} (Figure 5.3c). The former two bands are attributed to trans-gauche defects in the overall ordered alkyl chains, and the latter to the CH_2 adjacent to the NHS ester group.[33] The appearance of trans-gauche CH_2 vibrations in the backbone alkyl chains indicates the introduction of structural disorder upon surface activation, which may be due to spatial crowding during NHS ester formation via a bulky intermediate,[39] or to the oxidation of silicon induced by prolonged incubation in an aqueous environment. In order to determine the origin of this structural change, we carried out a control experiment with a ≡Si-$(CH_2)_9CH_3$ sample that was treated with NHS/EDC for 2 h under the same conditions as the surface activation of mixed monolayers. The resulting SFG spectrum

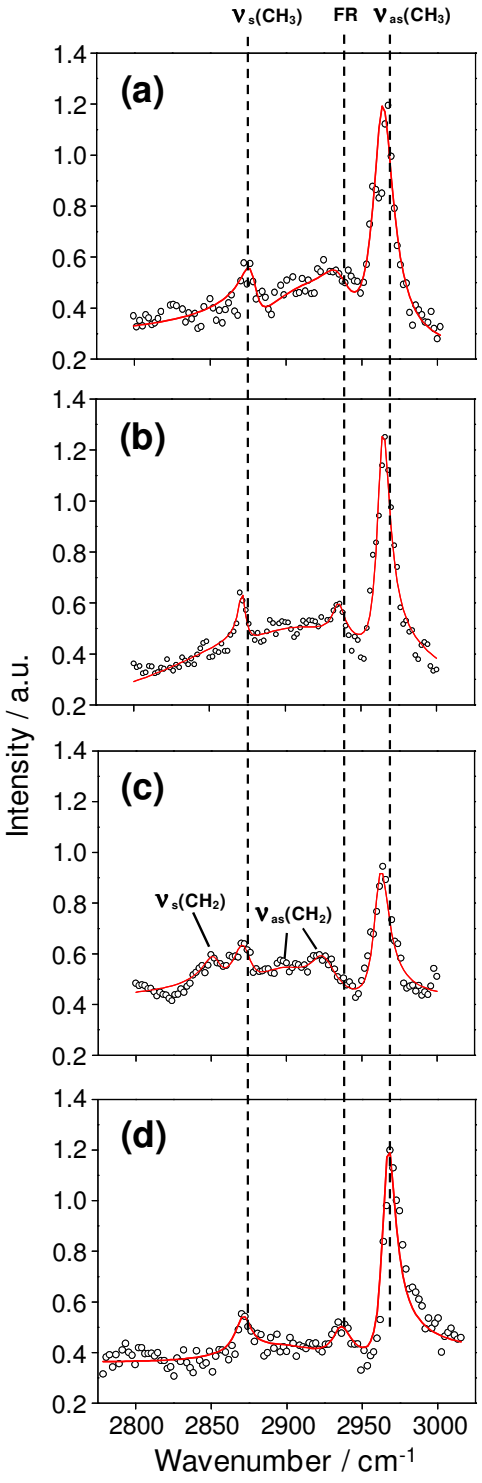

Figure 5.3 SFG spectra of (a) C10 monolayer, ≡Si-$(CH_2)_9CH_3$; (b) mixed monolayer, ≡Si-$(CH_2)_9CH_3$/ ≡Si-$(CH_2)_{10}$COOH; (c) mixed monolayer after formation of NHS ester; (d) C10 monolayer upon NHS/EDC treatment (control).

Sample	$\theta(H_2O)$	d_{ellips} (Å)
≡Si-$(CH_2)_9CH_3$ (C10)	108.6 ± 0.9	11.8 ±1.0
≡Si-$(CH_2)_9CH_3$/ ≡Si-$(CH_2)_{10}COOH$ (linker)	92.1 ± 1.3	11.9 ± 0.6
≡Si-linker-ssDNA (Na^+)	61.1 ± 3.4	32.9 ± 3.7
≡Si-linker-ssDNA (K^+)	64.7 ± 2.8	30.1 ± 2.8
≡Si-linker-ssDNA (Ca^{2+})	58.8 ± 2.4	27.0 ± 2.6
≡Si-linker-ssDNA (Mg^{2+})	54.7 ± 2.7	26.5 ± 0.7

Table 5.1 Thickness and wetting measurements for the control, linker and ssDNA monolayers on silicon and the effect of different metal cations.

(Figure 5.3d) shows that methylene-related peaks were negligible and the general features were virtually identical to those of ≡Si-$(CH_2)_9CH_3$ (Figure 5.3b). We have therefore confirmed that the disruption of the mixed monolayer structure upon activation is not due to oxidation or damage of the silicon substrate, rather it relates directly to the surface reactions of carboxyl groups.

5.3.2 Immobilization of DNA strands

Silicon surfaces upon immobilization of DNA strands were first analyzed by XPS to confirm the coupling reaction. Since phosphate (P) and nitrogen (N) peaks are typically not influenced by surface contamination, they (particularly P peaks) constitute good evidence for the presence of DNA strands on the surface. Samples prepared in the

presence of different cations all exhibited identical XPS profiles; representative high-resolution spectra in the Si-2p, N-1s and P-2p regions are shown in Figure 5.4. The P-2p peak observed at 134.3 eV is consistent with that reported for the phosphate backbone of DNA.[40, 41] The high-resolution spectrum of Si 2p exhibited a single peak at 99.5 eV. The slight deviation of Si 2p peak from Gaussian-shape may indicate slight surface oxidation; however, the lack of individual peak at a higher binding energy indicates that the passivation with organic monolayer was able to minimize the oxidation of silicon during the surface activation and DNA immobilization steps. The -NH- group in the linker as well as the non-conjugated nitrogen of DNA bases are represented by the N 1s peak at 400.2 eV, which has been reported to be the characteristic signal of non-conjugated nitrogen.[42] No N 1s peak corresponding to N-O (402.6 eV)[19] was observed, indicating the efficient amide-coupling of amine-functionalized DNA to the surface carboxyl groups (Figure 5.1).

The significant decrease in water contact angles and increase in the monolayer thickness (Table 5.1) observed upon DNA immobilization are additional evidence for the covalent anchoring of DNA strands on silicon surface, as they are intrinsically hydrophilic molecules. Our thickness data are comparable to those reported in the literature,[43] yet substantial differences among DNA SAMs prepared in the presence of different cations have been observed. Furthermore, the presence of DNA monolayer was confirmed by electrochemical method discussed in the experimental section; the surface densities of the ssDNA (Table 5.2) were comparable and within experimental uncertainty . These results are elaborated in the following section.

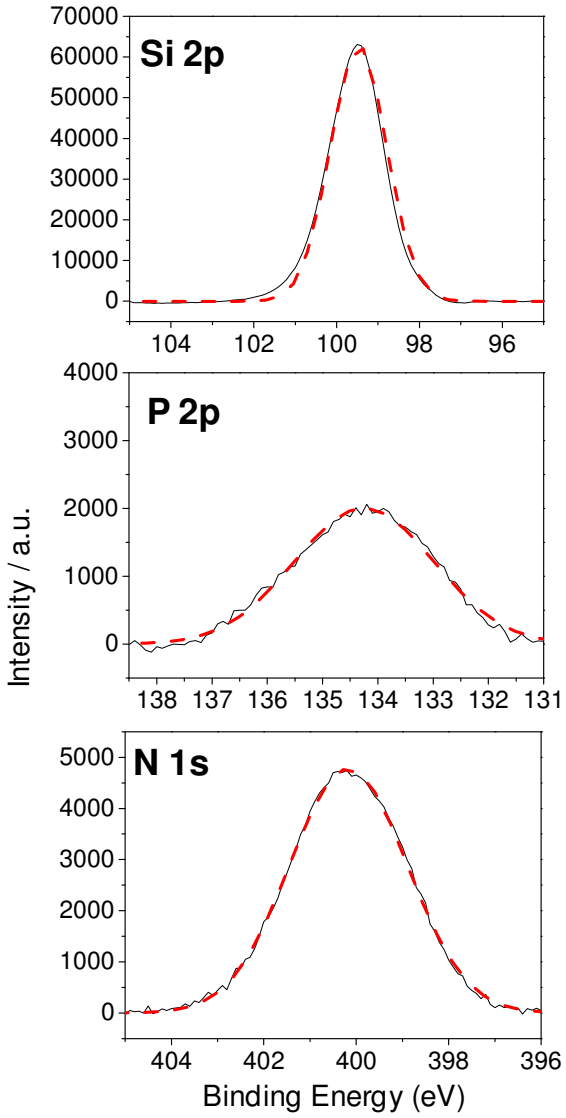

Figure 5.4 High resolution XPS spectrum of DNA SAMs on silicon prepared in the presence of 20 mM Na+. All peaks were fitted with Gaussian profiles that are shown as dash lines in red.

Sample	Γ_{DNA} ($\times 10^{12}$ molecule • cm^{-2})
≡Si-linker-ssDNA (Na^+)	2.21 ± 0.22
≡Si-linker-ssDNA (K^+)	2.45 ± 0.27
≡Si-linker-ssDNA (Ca^{2+})	2.00 ± 0.60
≡Si-linker-ssDNA (Mg^{2+})	2.51 ± 0.31

Table 5.2 Surface density of silicon modified with ssDNA SAMs immobilized under the presence of 20 mM NaCl, KCl, $CaCl_2$, or $MgCl_2$.

5.3.3 Structure of DNA SAMs and the Effect of Cations

In order to compare the effect of different cations on the formation and reactivity of DNA SAMs on silicon, 20 mM NaCl, KCl, $CaCl_2$ or $MgCl_2$ was added to the buffer used in the surface coupling and hybridization steps (50 mM HEPES, pH 7.2). The SFG spectra of the silicon surfaces upon DNA immobilization and subsequent hybridization are summarized in Figure 5.5. Trans-gauche defects are observed in all cases, i.e., methylene related peaks became evident, and methyl bands were considerably weakened. Nevertheless, several spectral features differ discernibly from each other for the four ssDNA samples prepared differently: in the presence of Na^+ (top of Figure 5.5a) or K^+ (top of Figure 5.5b), the linker monolayer is less disordered than those prepared with Ca^{2+} (top of Figure 5.5c), as indicated by the more pronounced methyl peaks. Mg^{2+} ions had the most significant effect (top of Figure 5.5d), i.e., the CH_3 bands became weaker in comparison with the CH_2 peak intensities.

A quantitative determination of the number of gauche defects in the alkyl chains could not be easily obtained; however, the CH_3/CH_2 peak intensity ratio (r^-/d^-) provides a good measure of the molecular order within an organic monolayer: the higher the ratio, the more ordered the alkyl chains.[27] Based on the spectra shown in Figure 5.5 (top spectrum of each panel), this value was found to be 1.8 ± 0.2 for a sample exposed to Na^+, 1.8 ± 0.1 for K^+, 1.4 ± 0.2 for Ca^{2+}, and 0.7 ± 0.3 for Mg^{2+}; therefore, the distortion of the linker monolayer decreased in the order $Mg^{2+} > Ca^{2+} > Na^+ \approx K^+$. Such a trend is strikingly akin to the affinities of metal cations for nucleic acids: divalent cations bind much more strongly than monovalent cations.[13] However, there are contradictory reports regarding the affinities of Mg^{2+} and Ca^{2+} for DNA.[13,14] We have, therefore, carried out XPS studies to further illustrate the differences between these two divalent cations. As shown in Figure 5.6, Ca^{2+} and Mg^{2+} were both observed in the ssDNA SAMs as evidenced by the Ca 2p (342 eV) and Mg 2p peaks, respectively. The Mg 2p spectrum had to be deconvoluted into two peaks at 52.0 and 55.0 eV to obtain the best fit (Figure 5.6a), indicating that there are at least two distinctive sites for Mg-DNA interactions: the negatively charged phosphate backbone (higher energy) surrounded by Mg^{2+} ions, and the nucleoside units (lower energy) hydrogen bonded to hydrated Mg^{2+} ions.[1] Compared to Ca^{2+}, Mg^{2+} existed more persistently within the monolayer as evidenced from the cation/phosphate signal ratio (normalized by the respective sensitivity factor of the XPS measurements): the value for Mg/P was estimated to be 1.45, which is much higher than that of Ca/P peaks (0.04). We believe that such a large difference is not due to the

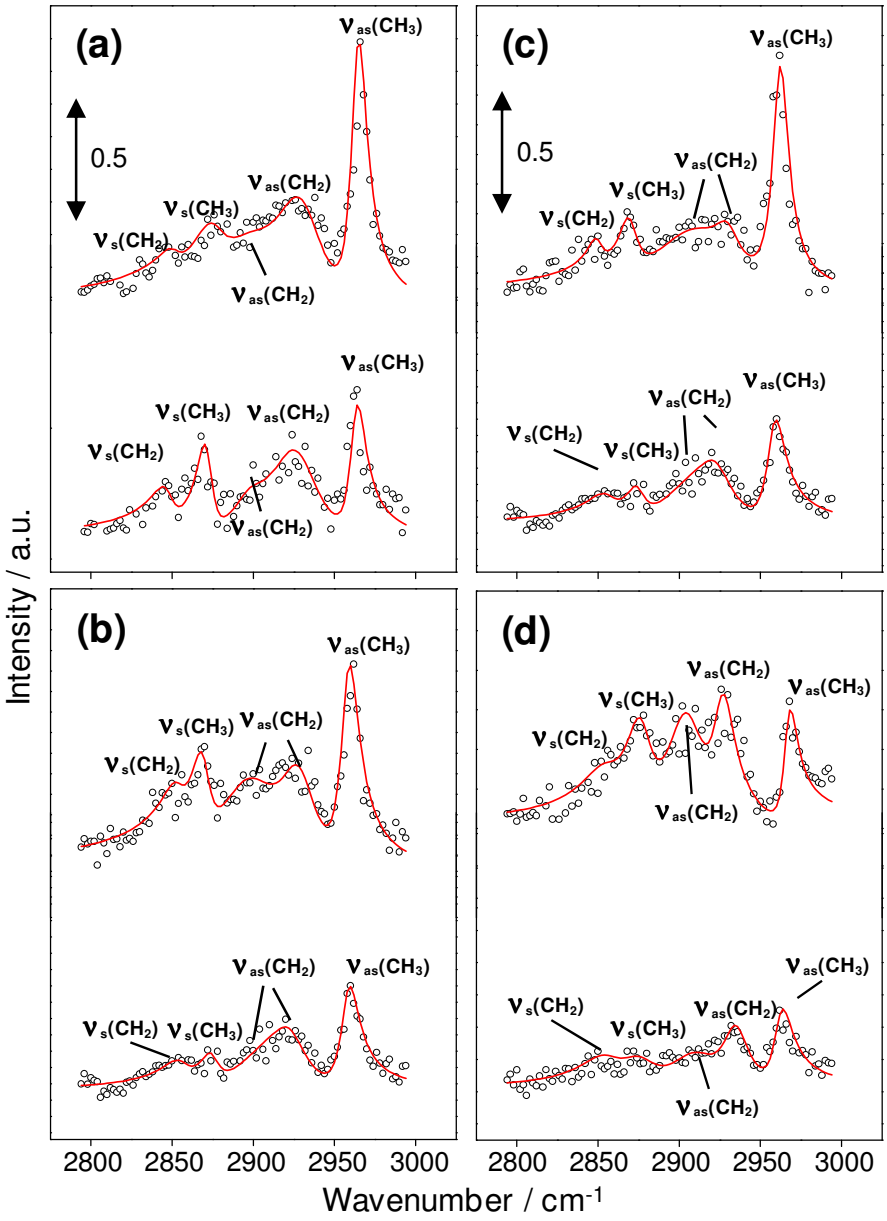

Figure 5.5 SFG spectra of silicon modified with DNA SAMs prepared in the presence of 20 mM (a) NaCl (b) KCl (c) $CaCl_2$, or (d) $MgCl_2$. In each panel, the top spectrum (red fitting line) is from the activated silicon surface upon immobilization of probe strands (ssDNA SAMs on silicon) and the bottom spectrum (blue fitting line) is that after hybridization (dsDNA SAMs on silicon).

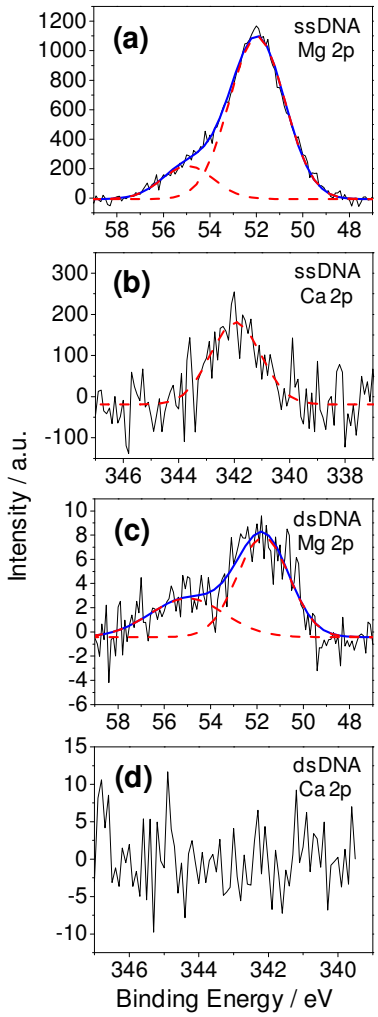

Figure 5.6 XPS spectra of silicon modified with DNA SAMs upon immobilization in the presence of 20 mM (a) $MgCl_2$, (b) $CaCl_2$; and after hybridization with complementary strands in the presence of 20 mM (c) $MgCl_2$, and (d) $CaCl_2$. All peaks were fitted with Gaussian profiles. Mg 2p spectrum was deconvoluted into two peaks (red dash lines) suggesting that there are two unique interaction sites within DNA.

difference in their binding constants[44] rather the different exchange rates with other cations present in the medium (i.e., washing buffer). Ray et al. have reported that the concentration of cations within DNA monolayers decreases quickly upon exchanging with protons.[43]

Upon hybridization with the complementary DNA strand, only a trace of the Mg signal was observed (Figure 5.6c), and the signal for Ca was negligible (Figure 5.6d). Monovalent cations were not observed in either single- or double-stranded DNA SAMs on silicon as previously reported;[43] the shortage of cations to neutralize the DNA may be compensated by the adsorption of protons. Furthermore, differences in persistency among cations are exhibited in wetting measurements (Table 5.1). The water contact angles of ssDNA SAMs prepared in the presence of different cations increased in the order Mg^{2+} ($54.7 \pm 2.7°$) < Ca^{2+} ($58.8 \pm 2.4°$) < Na^{+} ($61.1 \pm 3.4°$) < K^{+} ($64.7 \pm 2.8°$). Such a decrease in surface hydrophilicity can be explained by the difference in the number of cations trapped within the DNA monolayer on silicon.

To explain the correlation between degree of deformation of the linker monolayer and DNA-cation affinities ($Mg^{2+} > Ca^{2+} > Na^{+} \approx K^{+}$), the effect of the cations on the conformations of DNA strands must be considered. DNA is a locally stiff molecule but uneven "neutralization" of the phosphate backbone could be a significant driving force for conformational change.[3] Since the most frequent interactions between metal cations and DNA occur at the guanine bases, the distribution of cations around the DNA molecule is not uniform, causing DNA strands to curve and bend substantially on the surface. Deformation of the DNA SAMs is expected to be more significant as DNA-cation interactions become stronger, which would explain the fact that Mg^{2+} ions disrupt the SAM structure more effectively than sodium or potassium ions. If such distortion is significant enough, it will likely affect the lateral order of the underlying linker monolayer (Figure 5.7).

We therefore conclude that the perturbation to the structure of the linker monolayer results from the deformation (curvature and binding) of DNA strands on surface induced by their interactions with metal cations in solution: the r^-/d^- ratio reflects the degree of such structural deformation. Accordingly, the lowest r^-/d^- ratio (0.7 ± 0.3) measured in the presence of Mg^{2+} is an indication of substantially deformed DNA SAMs, while Ca^{2+} has a smaller effect. Our results show that the deformation of ssDNA SAMs caused by milimolar concentrations of Na^+ or K^+ is negligible, certainly insufficient to disrupt the underlying alkyl chains (Figure 5.7a). Prior to DNA immobilization, the r^-/d^- ratio was 1.9 ± 0.2 (Figure 5.3c) which is virtually identical to that of a DNA monolayer prepared in the presence of 20 mM Na^+ or K^+ (top spectra of Figures 5.5a and 5.5b).

The remarkable difference between the conformational orders of ssDNA SAMs prepared with different cations is also supported by ellipsometric measurements (Table 5.1). Layer thickness correlated well with DNA-cation affinity: Mg^{2+} (26.5 ± 0.7 Å) < Ca^{2+} (27.0 ± 2.6 Å) < Na^+ (32.9 ± 3.7 Å) ≈ K^+ (30.1 ± 2.8 Å). As the affinity increases, the layer thickness decreased. Bends and curvature will shorten the length of the DNA strands, thus the layer thickness should decrease accordingly as the deformation becomes more significant. The surface density of DNA monolayer prepared under different saline conditions were comparable and is within the magnitude to those reported for DNA on gold surface (Table 5.2).[31, 32] It appears that the conditions for all the four cases were sufficient to minimize the repulsive forces between DNA during immobilization.

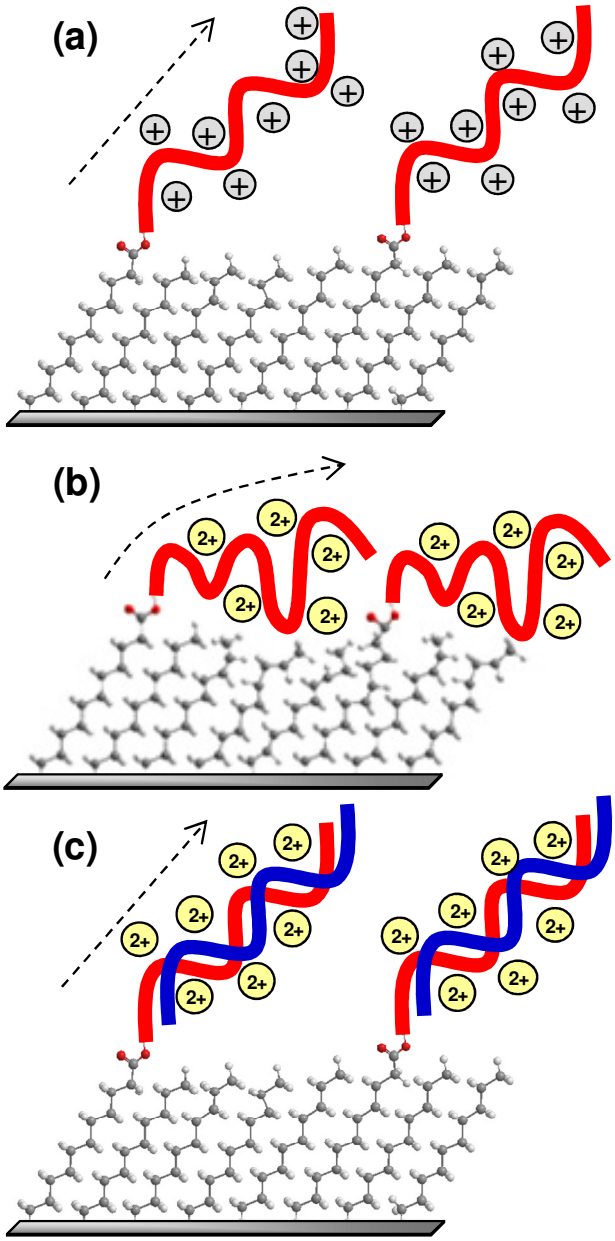

Figure 5.7 Hypothetic representation of cation-induced structural changes of DNA/linker monolayer on silicon surface. (a) In the presence of monovalent cations, the geometry of DNA is unaffected and the underlying linker monolayer keeps its ordered conformation. (b) Divalent cation-induced DNA deformation significantly perturbs the linker monolayer. (c) Hybridization in the presence of divalent cations does not introduce further disruption to the linker monolayer structure.

Upon hybridization in the presence of monovalent cations, the linker monolayer structure becomes more disordered (bottom of Figures 5.5a and 5.5b): the r^-/d^- value dropped to 1.2 ± 0.2 and 1.3 ± 0.1 for Na^+ and K^+, respectively. However, in this case the extent of further structural disruption is not as significant as in the immobilization step. Molecular dynamics simulations have indicated that DNA double helices tethered on chips have minimal contacts with the surface and point mostly into the solution,[45, 46] therefore the disruptions, most likely due to spatial restraints during incorporation of the complementary strands, are "transferred" to the underlying alkyl chains. In the presence of divalent cations, the r^-/d^- ratio was not affected as much (bottom of Figures 5.5c and 5.5d : 1.2 ± 0.3 and 0.8 ± 0.2 for Ca^{2+} and Mg^{2+}, respectively). There are mainly three regions where metal cations interact with double-stranded DNA: the phosphate backbone, the major grooves and the minor grooves.[11] Monovalent cations bind preferentially in the minor grooves of an AT-tract,[2] whereas Mg^{2+} and Ca^{2+} prefer to coordinate with both the major and the minor grooves.[45] While such preferential binding will induce structural deformation of both ssDNA and dsDNA SAMs, our experimental data support the view that it does not influence the conformation of dsDNA monolayers as significantly as that of ssDNA SAMs on silicon. DNA double helices are much stiffer than ssDNA and, once hybridized, they will maintain well-oriented conformations with minimum DNA-surface interactions,[45-46] which are not influenced significantly by the presence of divalent cations. In fact, the divalent cations would reduce the repulsion between the DNA strands,[4] thereby facilitating hybridization in a more confined space and minimizing disruption of the underlying linker layers. This view is further supported by hybridization efficiencies estimated for the samples where divalent cations hybridized at a higher rate; 66% and

Sample	Γ_{DNA} ($\times 10^{12}$ molecules $\cdot$ cm^{-2})	Hybridization Efficiency (%)
≡Si-linker-dsDNA (Na^+)	2.72 ± 0.41	23
≡Si-linker-dsDNA (K^+)	2.96 ± 0.32	21
≡Si-linker-dsDNA (Ca^{2+})	3.32 ± 0.46	66
≡Si-linker-dsDNA (Mg^{2+})	3.81 ± 0.16	52

Table 5.3 Surface density and hybridization efficiency of silicon modified with dsDNA SAMs hybridized under the presence of 20 mM NaCl, KCl, $CaCl_2$, or $MgCl_2$.

52% for Ca^{2+} and Mg^{2+} whereas 23% and 21% for Na^+ and K^+, respectively (Table 5.3). Overall, the hybridization process has a small influence on the lateral order of the linker monolayer (Figure 5.7c), although it does not revert to the original ordered packing. We have elaborated the influence of metal cations on the conformation of DNA strands on silicon and concluded that their effect on the hybridization process is the origin of the conformational changes in the linker monolayers. Our postulate is based on SFG data (Figure 5.5), showing that the extent of such distortion of the alkyl chains parallels the order of cation-DNA affinities. However, there is another possible cause: the interaction between positively charged ions, especially relatively soft ions such as Ca^{2+}, and underlying unreacted carboxyl groups may be strong enough to induce the observed deformation of the linker layer. To exclude this possibility, a control experiment was carried out with mixed monolayers formed from 1-decene and undecylenic acid (molar ratio 9:1) incubated in 20 mM NaCl, KCl, $CaCl_2$ or $MgCl_2$ overnight. None of the cations caused significant changes in the SFG spectra of monolayer-modified silicon surfaces. As

shown in Figure 5.8, even after prolonged incubation in Mg^{2+} solutions the features of a well-ordered linker monolayer are retained: strong intensity of methyl bands and negligible methylene peaks. Therefore, we can conclude that the disruption of linker monolayer structure is predominately induced by deformation of the DNA SAMs.

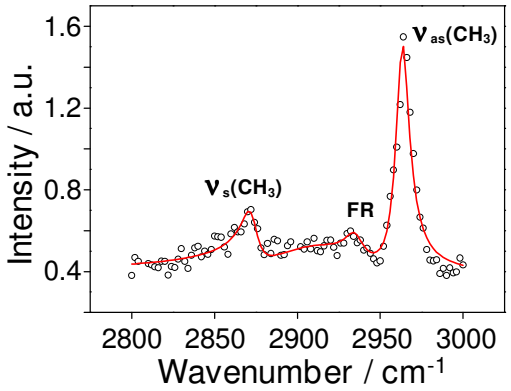

Figure 5.8 Representative SFG spectrum of the mixed monolayer on silicon prepared from 1-decene/undecylenic acid (9:1) treated with 20 mM $MgCl_2$ overnight.

5.4 Conclusion

The effect of metal cations on the formation of ssDNA SAMs on silicon and on the hybridization process is significant. Our SFG investigation confirms semi-quantitatively that the extent of structural distortion parallels the order of metal ion-DNA affinities. The trend was opposite during hybridization where further disruption of the underlying linker monolayer was greater for monovalent cations (Na^+ and K^+) indicating that divalent metal cations (in particular Mg^{2+}) are able to facilitate hybridization in a more spatially confined manner. We provided herein the first spectroscopic evidence for the cation-induced conformational changes of DNA strands on surfaces. Such information is critical

for the preparation of DNA microarrays with optimal probe density and molecular conformation, which dictates the on-chip hybridization efficiency.

5.5 Bibliography

(1) Hud, N. V.; Polak, M., *Curr. Opin. Struc. Bio.* **2001,** *11*, 293.

(2) McFail-Isom, L.; Sines, C. C.; Williams, L. D., *Curr. Opin. Struc. Bio.* **1999,** *9*, 298.

(3) Williams, L. D., *Annu. Rev. Biophys. Biomol. Struct.* **2000,** *29*, 497.

(4) Allahyarov, E.; Gompper, G.; Lowen, H., *Phys. Rev. E* **2004,** *69*, 041904.

(5) Allahyarov, E.; Lowen, H.; Gompper, G., *Phys. Rev. E* **2003,** *68*, 061903.

(6) Anderson, C. F.; Record, M. T., *Annu. Rev. Phys. Chem.* **1995,** *46*, 657.

(7) Andresen, K.; Das, R.; Park, H. Y.; Smith, H.; Kwok, L. W.; Lamb, J. S.; Kirkland, E. J.; Herschlag, D.; Finkelstein, K. D.; Pollack, L., *Phys. Rev. Lett.* **2004,** *93*, 248103.

(8) Cerda, B. A.; Wesdemiotis, C., *J. Am. Chem. Soc.* **1996,** *118*, 11884-11892.

(9) Korolev, N.; Lyubartsev, A. P.; Rupprecht, A.; Nordenskiold, L., *Biophys. J* . **1999,** *77*, 2736.

(10) Savelyev, A.; Papoian, G. A., *J. Am. Chem. Soc.* **2006,** *128*, 14506.

(11) Subirana, J. A.; Soler-Lopez, M., *Annu. Rev. Biophys. Biomol. Struct.* **2003,** *32*, 27.

(12) Tan, Z. J.; Chen, S. J., *Biophys. J* . **2006,** *90*, 1175.

(13) Korolev, N.; Lyubartsev, A. P.; Rupprecht, A.; Nordenskiold, L., *J. Phys. Chem. B* **1999,** *103*, 9008.

(14) Russo, N.; Toscano, M.; Grand, A., *J. Phys. Chem. A* **2003,** *107*, 11533.

(15) Herne, T. M.; Tarlov, M. J., *J. Am. Chem. Soc.* **1997,** *119*, 8916.

(16) Cai, W.; Peck, J. R.; Weide, D. W. v. d.; Hamers, R. J., *Biosensors and Bioelectronics* **2004,** *19*, 1013.

(17) Pike, A. R.; Lie, L. H.; Eagling, R. A.; Ryder, L. C.; Patole, S. N.; Connolly, B. A.; Horrocks, B. R.; Houlton, A., *Angew. Chem. Int. Ed.* **2002,** *41*, 615.

(18) Strother, T.; Cai, W.; Zhao, X. S.; Hamers, R. J.; Smith, L. M., *J. Am. Chem. Soc.* **2000,** *122*, 1205.

(19) Voicu, R.; Boukherroub, R.; Bartzoka, V.; Ward, T.; Wojtyk, J. T. C.; Wayner, D. D. M., *Langmuir* **2004,** *20*, 11713.

(20) Yin, H. B.; Brown, T.; Greef, R.; Wilkinson, J. S.; Melvin, T., *Microelectronic Engineering* **2004,** *73-74*, 830.

(21) Yin, H. B.; Brown, T.; Wilkinson, J. S.; Eason, R. W.; Melvin, T., *Nucleic Acids Res.* **2004,** *32*, e113.

(22) Pike, A.; Horrocks, B.; Connolly, B.; Houlton, A., *Aust. J. Chem.* **2002,** *55*, 191.

(23) Pirrung, M. C., *Angew. Chem. Int. Ed.* **2002,** *41*, 1276.

(24) Xiao, Y.; Piorek, B. D.; Plaxco, K. W.; Heeger, A. J., *J. Am. Chem. Soc.* **2005,** *127*, 17990.

(25) Boukherroub, R., *Curr. Opin. Solid State Mater. Sci.* **2005,** *9*, 66.

(26) Wagner, P.; Nock, S.; Spudich, J. A.; Volkmuth, W. D.; Chu, S.; Cicero, R. L.; Wade, C. P.; Linford, M. R.; Chidsey, C. E. D., *J. Struct. Bio.* **1997,** *119*, 189.

(27) Messmer, M. C.; Conboy, J. C.; Richmond, G. L., *J. Am. Chem. Soc.* **1995,** *117*, 8039.

(28) Richmond, G. L., *Chem. Rev.* **2002,** *102*, 2693.

(29) Shen, Y. R., *Nature* **1989,** *337*, 519.

(30) Stokes, G. Y.; Gibbs-Davis, J. M.; Boman, F. C.; Stepp, B. R.; Condie, A. G.; Nguyen, S. T.; Geiger, F. M., *J. Am. Chem. Soc.* **2007,** *129*, 7492.

(31) Asanuma, H.; Noguchi, H.; Uosaki, K.; Yu, H. Z., *J. Phys. Chem. B* **2006,** *110*, 4892.

(32) Yu, H. Z.; Luo, C. Y.; Sankar, C. G.; Sen, D. *Anal. Chem.* **2003**, *75*, 3902.

(33) Su, L.; Sankar, C. G.; Sen, D.; Yu, H. Z. *Anal. Chem.* **2004**, *76*, 5953.

(34) Ye, S.; Nihonyanagi, S.; Uosaki, K., *Phys. Chem. Chem. Phys.* **2001**, *3*, 3463.

(35) Nihonyanagi, S.; Miyamoto, D.; Idojiri, S; Uosaki, K. *J. Am. Chem. Soc.* **2004**, *126*, 7034.

(36) Ishibashi, T.; Ara, M.; Tada, H.; Onishi, H. *Chem. Phys. Lett.* **2003**, *367*, 376.

(37) Fabre, B.; Hauquier, F., *J. Phys. Chem. B* **2006,** *110*, 6848.

(38) Linford, M. R.; Fenter, P.; Eisenberger, P. M.; Chidsey, C. E. D., *J. Am. Chem. Soc.* **1995,** *117*, 3145.

(39) Sehgal, D.; Vijay, I. K., *Anal. Biochem.* **1994,** *218*, 87.

(40) Lee, C. Y.; Gong, P.; Harbers, G. M.; Grainger, D. W.; Castner, D. G.; Gamble, L. J., *Anal. Chem.* **2006,** *78*, 3316.

(41) Petrovykh, D. Y.; Kimura-Suda, H.; Tarlov, M. J.; Whitman, L. J., *Langmuir* **2004,** *20*, 429.

(42) Saprigin, A. V.; Thomas, C. W.; Dulcey, C. S.; Patterson, C. H.; Spector, M. S., *Surf. Interface Anal.* **2005,** *37*, 24.

(43) Ray, S. G.; Cohen, H.; Naaman, R.; Rabin, Y., *J. Am. Chem. Soc.* **2005,** *127*, 17138.

(44) Su, L.; Sen, D.; Yu, H.-Z., *Analyst* **2006**, *131*, 317.

(45) Wong, K.-Y.; Pettitt, M. B., *Theor. Chem. Acc.* **2001,** *106*, 233.

(46) Wong, K.-Y.; Pettitt, M. B., *Biopolymers* **2004,** *73*, 570.

(47) Minasov, G.; Tereshko, V.; Egli, M., *J. Mol. Biol.* **1999,** *291*, 83.

Chapter 6. Feasibility of conventional metal deposition methods to prepare metal contacts on organic monolayers on silicon

As mentioned in Chapter 1, DNA monolayers prepared on semiconductors can be used not only as biochips, but also as components of molecular electronics. There is a vast amount of interest in the conductivity of DNA; it has been speculated that DNA is a large-bandgap semiconductor and could possibly be utilized to tune the bulk properties of semiconductors.[1]

Ideally, a single DNA molecule can be characterized by forming a bridge between two electrodes.[1] However, the use of discrete molecules as working electronic units is challenging. From a technical standpoint, the electrical contacts formed to single molecules must be free of current leakage (by bypassing the molecules) and robust during extensive use; therefore, a better understanding of the physical aspects of molecule| electrode interfaces is needed.[2, 3]

A more realistic approach is the use of groups/clusters of molecules instead of single molecule(s). One of the most thoroughly explored methods is the incorporation of ultrathin organic films, such as self-assembled monolayers (SAMs) and Langmuir-Blodgett (LB) films.[4, 5] The molecular structure of these organic monolayers not only determines the rate of electron transfer across the interface,[6] but also allows fine-tuning of the bulk material properties. In this chapter, the feasibility of conventional deposition

methods, thermal deposition and sputtering coating, to prepare metal contact electrodes will be assessed. As a model system, alkyl monolayers on silicon were tested by placing gold contacts on top. The results suggest that the top gold contacts (overlayers) introduce significant gauche defects within the initially, highly oriented alkyl chains, although these n-alkyl monolayers directly attached to silicon apparently survived the deposition process under the conditions specified in this study. The estimated methyl tilt angles of the buried monolayers vary substantially depending on the deposition method (vacuum evaporation vs. sputtering) and on the alkyl chain length (from 1-decyl to 1-octadecyl). These observations are supported by solid-state electrical measurements and other structural characterizations.

6.1 Introduction

As the miniaturization of electronic devices progresses, the ability to fabricate nanoscale structures or molecular components has emerged in the past decades. There have been many reports on organic molecule(s) that act as either passive (i.e., tunnelling junctions, rectifiers) or active components (i.e., switches, transistors, and logic gates) in semiconductor devices.[7] In many cases, the organic molecules were assembled into monolayers that are buried at metal/metal or metal/semiconductor interfaces; the orientation and conformation of these molecules play a crucial role in the function of the molecular junctions formed upon them. Therefore, understanding of the structural and conformational details of organic monolayers at buried interfaces are of practical importance.

In the past few years, several spectroscopic studies of SAMs at metal/metal or metal/semiconductor interfaces have been reported.[8-13.] While Jun and Zhu developed their attenuated total reflection (ATR) setup to probe buried molecular interfaces by using their IR studies,[10] p-polarized backside reflection absorption infrared spectroscopy (pb-RAIRS) has been adapted successfully in the study of the interactions between deposited metal contacts and organic monolayers on silicon surfaces.[11-13] These pioneer investigations typically relied on the observed peak broadening, shifting, and changes in intensity; Jun and Zhu have suggested that the peak broadening observed for metal/OTS/silicon interface is due to the monolayer disordering and the peak attenuation to the loss of C-H bonds due to damage to the molecules.[10] Hacker et al. have reported the complete disappearance of methylene bands in the IR spectrum of 1-octadecyl monolayer on silicon upon the deposition of 5 nm gold film.[12] These observations may not be simply explained due to the facts that the dipoles of molecules can be "suppressed" by the metal overlayers, and that the roughness of metal layer may induce scattering of the infrared beam at the metal/molecule interfaces.[14] There are cases where new bands arise upon the deposition of metal atoms on top of the organic monolayer; Richter et al. assigned the new peak at ~2825 cm^{-1} from the metal/OTS/Si system to the methylene-metal interactions.[11]

Nevertheless, the above-mentioned spectral features are not easy to distinguish as they are typically broad, weak, and sometimes obscured. Therefore, the fundamental understanding of metal-molecule interactions is still needed. Herein, the effect of the chain length of n-alkyl monolayers on oxide-free silicon is examined, as well as the influence of the coating methods (thermal evaporation vs. sputtering deposition) for the

metal contacts will be investigated. Besides the possible changes of the vibrational bands related to the alkyl chains (CH_3 and CH_2 groups), we were able to monitor the direct Au-CH interactions based on our combined SFG and ATR-IR studies. SFG spectroscopy provide additional information to these IR studies, as it is intrinsically sensitive to the interfacial molecular conformation and exhibits submonolayer sensitivity.[15] Solid-state electrical measurements are also carried out on the formed Au/n-alkyl monolayer/Si junctions to augment the findings of the vibrational spectroscopic investigations.

6.2 Experimental

6.2.1 Materials

All chemicals were of ACS reagent grade and used as received unless otherwise mentioned. Deionized water (>18.3 MΩ·cm) was used throughout the experiments. 1-decene (94%), 1-dodecene (95%), 1-tetradecene (92%), 1-octadecene (90%), and 1,1,1,-trichloroethane (99.5%) were obtained from Aldrich; tetrahydrofuran (THF), sulfuric acid (96%), and hydrogen peroxide (30%) were purchased from Wako Chemicals; ammonium fluoride (40%) was from Morita Chemical Industries. 1-decene (94%), 1-dodecene (95%), 1-tetradecene (92%), and 1-octadecene (90%) were distilled from sodium under reduced pressure (20-30 Torr) followed by freeze-thaw cycles under vacuum/nitrogen.

6.2.2 Surface preparation

Silicon (111) wafers (0.5-5.0 Ω·cm, n-type, Virginia Semiconductor Inc.) and Attenuated total reflectance (ATR) silicon crystals (25 × 5 × 1 mm^3, Harrick Scientific Inc.) were cleaned and etched as previously mentioned (Chapter 3.2.3). The fresh ≡Si-H

samples were then introduced under argon into Schlenk tubes containing 2-3 mL of deoxygenated neat 1-alkenes and heated to 160 ºC for 4 h. Thus modified silicon samples (≡Si-C_nH_{2n+1}, n = 10, 12, 14, and 18; abbreviated as **C10**, **C12**, **C14**, and **C18**, respectively) were cleaned with THF, trifluororoacetic acid solution in THF (1%), and 1,1,1-trichloroethane sequentially, and blown dry with N_2 gas.

Gold deposition on freshly prepared silicon samples was performed via thermal evaporation or sputtering. Thermal evaporation was carried out in a vacuum evaporation apparatus (Ulvac, EBH-6). The chamber pressure is lowered to the base pressure of 10^{-6} Torr using a diffusion-pump; gold (99.99%) was then deposited at a rate of 0.1 nm/s until it reached the film thickness of 10 nm (measured by a calibrated quartz crystal oscillator). Gold sputtering was carried out with a Joel JFC-1200 sputtering coater in an argon purged chamber under reduced pressure (~2.0×10^{-2} Torr). The filament current was kept at approximately 15 mA until desired film thickness (~ 10 nm) was reached. The size of gold contacts was controlled by using an aluminum mask with 9 holes (3 mm in diameter).

6.2.3 SFG

A description of SFG system and setup is available in Chapter 3.2.4 and 5.2.3. The equations presented in Chapter 3.2.4 (equations 1 and 2) were used to express the SFG intensity. All the uncertainties were derived from at least three individual spectra from independent samples. The quality of the fit is judged by r^2 values that was at least 0.900 and above. The detailed description of fitting routine and the fitting parameters are described in Appendix II.

6.2.4 Electrical measurements

The solid-state electrical measurements were carried out with an Autolab Electrochemical Analyzer (Model: PGSTAT 30, Eco Chemie BV, Netherlands). All the measurements were performed in a Faraday cage while the contact to the gold pad was made by lowering a tungsten probe with a home-made micro-positioning system. The current-voltage (*I-V*) curves were recorded from +0.5 V to –0.5 V at a scan rate of 0.05 V/s. The Mott-Schottky plots (C^{-2} *vs. V*) were acquired by scanning the potential from + 1.0 V to –1.5 V at a frequency of 100 kHz.

The dominant electron transport mechanism was assumed to be a thermionic emission process:[16-18]

$$J = A^{*}T^{2}\exp\left(-\frac{q\phi_{eff}}{kT}\right)\left(\frac{qV}{nkT}\right)\left[1-\exp\left(-\frac{qV}{kT}\right)\right] \qquad \textbf{(1)}$$

where J is the current density, q is the electronic charge, V is the applied bias voltage, n is the ideality factor, k is the Boltzmann constant, T is the absolute temperature, ϕ_{eff} is the effective barrier height, and A^{*} is the Richardson constant; the value 110A cm^{-2} K^{-2} for n-type silicon was used for A^{*}.[16] In order to extract the ideality factor (n) and the effective barrier height (ϕ_{eff}), equation 1 was rearranged to:

$$\ln\left[\frac{J}{1-e^{-\frac{qV}{kT}}}\right] = \ln\left(A^{*}T^{2}\right) - \frac{q\phi_{eff}}{kT} + \frac{qV}{nkT} \qquad \textbf{(2)}$$

At the forward bias in the range of 0.05V to 0.25V, the plot of $\ln\{J/[1-\exp(-qV/kT)]\}$ versus V is linear; the n and ϕ_{eff} values can be derived from the slope and intercept, respectively.

The Mott-Schottky plot was used to estimate the doping density (N_d) and built-in potential (V_{D0}) of the silicon substrate:[17, 18]

$$C^{-2} = \frac{2(V_{D0} - V)}{\varepsilon\varepsilon_0 N_d} \quad \textbf{(3)}$$

where C is the differential capacitance of the space charge layer, ε is the dielectric constant of silicon, and ε_0 is the permittivity of free space. The reverse-bias capacitance measurements were made at a high frequency to eliminate the influence of interface states.

6.2.5 Other measurements

ATR-FTIR and wetting measurements were performed as described in Chapter 3.2.4. Ellipsometric measurements were carried out with an Uvisel spectroscopic ellipsometer (Horiba Jobin Yvon) as detailed in Chapter 5.2.3. All the reported experimental uncertainties were derived from at least three spots from three independent samples.

6.3 Results and Discussion

6.3.1 n-Alkyl monolayers on silicon

The Si-C bonded n-alkyl monolayers on silicon were examined first by SFG spectroscopy prior to the metal deposition (Figure 6.1). All the spectra exhibited features that correspond to densely packed and well oriented monolayers.[19-21] Specifically, there were negligible contributions from methylene (CH_2) stretching modes and the spectra features were dominated by the contributions from the methyl (CH_3) groups; methyl symmetric stretch (r^+) at ~2878 cm^{-1}, Fermi resonance (FR) between r^+ and CH bending overtone at ~2940 cm^{-1}, and the CH_3 asymmetric stretch (r^-) at ~2964 cm^{-1}. These are the features of well-ordered and closely packed molecular monolayers, for which the alkyl chains are in all-trans configurations. The ellipsometric thickness and the wetting measurements summarized in Table 6.1 also support the above observations. The monotonic increase of the thickness from C10 to C18 monolayers is in good agreement with the calculation based on an average tilt angle of 35° for the alkyl chains (which correspond to a CH_3-tilt angle of ~70°) (Table 6.1). The static water contact angles were approximately 110º for all four monolayer systems, which are comparable to previous reports for well-packed alkyl monolayers (as they are intrinsically hydrophobic).[22-25] In fact, ATR-IR studies showed additional evidence (e.g., strong CH_2 asymmetric and symmetric stretching bands) for high quality of Si-C bonded monolayers (Figure 6.2). The CH_2 symmetric stretching modes are in the range of 2850-2851 cm^{-1} and the asymmetric stretching bands are in between 2919-2920 cm^{-1} for all the samples. Therefore, they are of similar quality in terms of packing density and molecular orientation; the n-alkyl monolayers on silicon are ordered and closely packed.[26, 27]

Sample	H_2O contact angle / degree	d_{exp} / Å	d_{calc} / Å[(a)]
≡Si-$(CH_2)_9CH_3$ (C10)	109 ± 2	12.8 ±1.0	11.4
≡Si-$(CH_2)_{11}CH_3$ (C12)	108 ± 3	14.0 ± 1.2	13.5
≡Si-$(CH_2)_{13}CH_3$ (C14)	109 ± 2	15.4 ± 1.1	15.7
≡Si-$(CH_2)_{17}CH_3$ (C18)	106 ± 2	20.4 ± 1.3	20.0

Table 6.1 Thickness and wetting measurements of n-alkyl monolayers on silicon.

6.3.1 n-Alkyl monolayers at gold/silicon interfaces

In Figures 6.3 and 6.4, we have shown the SFG spectra of the C10, C12, C14, and C18 monolayers on silicon with deposited gold overlayers prepared by either thermal evaporation (Figure 6.3) or sputtering deposition (Figure 6.4). In contrast to Figure 6.1, the resonant bands appear as downward peaks because of the phase difference (destructive interference) between the non-resonant background (substrate) and the resonance signal.[28, 29] The deconvoluted peaks are shown in Figure 6.3 and 6.4 (red line) in order to consider the peak elements without influence of the non-resonat contribution. Deconvolution was carried out the method described in page 52. In general, upon gold deposition, strong CH_2 symmetric (d^+) and asymmetric (d^-) peaks appeared at ~2850 cm^{-1} and ~2920 cm^{-1} (Figures 6.3 and 6.4). The methylene groups of well-ordered alkyl chains are positioned in a symmetric manner, yet when gauche defects are introduced, such symmetry will be

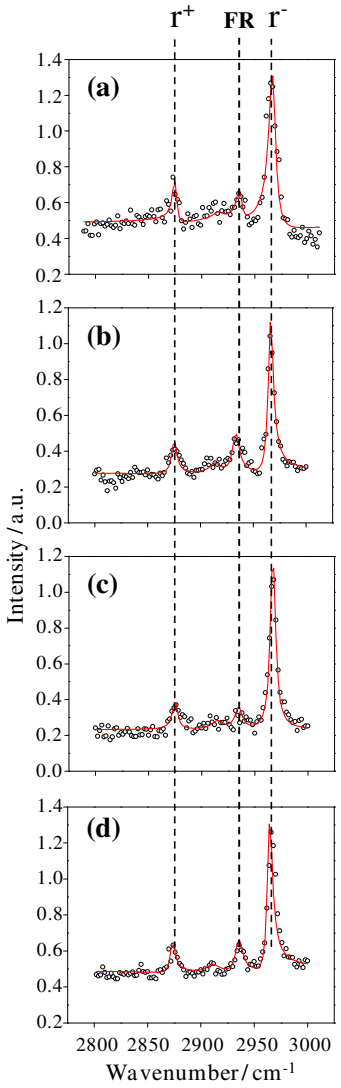

Figure 6.1 SFG spectra of (a) ≡Si-$(CH_2)_9CH_3$ (C10), (b) ≡Si-$(CH_2)_{11}CH_3$ (C12), (c) ≡Si-$(CH_2)_{13}CH_3$ (C14), and (d) ≡Si-$(CH_2)_{17}CH_3$ (C18). The solid lines (in red) showed the best fits based on eqs. (1) and (2) to the experimental data (open circles).

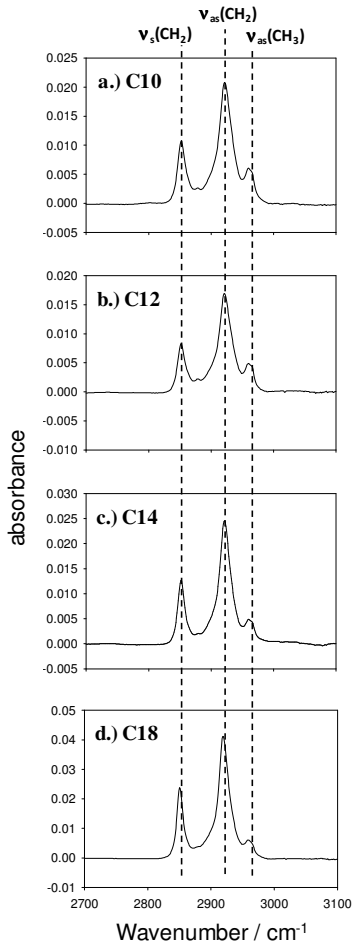

Figure 6.2 ATR-FTIR spectra of a) C10, b) C12, c) C14, and d) C18 monolayers on silicon.

broken and the SFG signal arises. Therefore, these new bands indicate that trans-gauche defects in the alkyl chain backbones were introduced upon metal deposition.[21, 30] Independent of the chain lengths of the monolayers, both thermal evaporation and sputtering deposition of gold contacts disrupted the molecular conformation of the SAMs significantly as evidenced by the substantial contributions of the methylene bands (d^+ and d^-). As shown by the deconvoluted peaks (Figure 6.3 and 6.4), stronger methylene contributions relative to methyl peaks are observed for samples prepared via sputtering in comparison with those prepared by thermal evaporation indicating that the sputtering

method is more destructive. Another important feature of the SFG spectra is the appearance of a new band at ~2900 cm^{-1}. Although a definite assignment of this band is not straightforward due to several factors such as the presence of d^+ Fermi resonance, we can cautiously assign this band to methylene (CH_2) groups that are interacting with gold, specifically to the CH bonds that are in the proximity of but not in the direct contact with gold atoms.[37] This means that upon metal deposition some regions of the alkyl chains are not directly in contact with gold. It has been suggested that gold will completely penetrate through n-alkyl monolayers on silicon.[12] Our SFG results have shown that, at least at the sub-monolayer scale, gold-penetration may indeed occur in a "patchy" manner.

Techniques such as FT-IR spectroscopy and time-of-flight secondary ion mass spectrometry (MOS-TOF) can help determine the presence of molecules and their chemical identities at buried interfaces.[8-11, 31] The present SFG investigations provide further insights in the molecular orientations; it was evident from the SFG spectra that the disordering of the originally highly oriented alkyl chains does occur, although the displacement of Si-C bonds has not been observed. The fact that the SFG spectra of n-alkyl monolayers at gold/silicon interfaces still exhibit strong methyl stretching bands, suggests that these organic monolayers are still relatively ordered after the formation of metal contacts on top.

This is seemingly different from the case of Haick et al. where the metal evaporation totally damaged the molecules and the decomposed residues did not remain at the interface.[32] Hacker et al. recently reported the displacement of entire monolayer

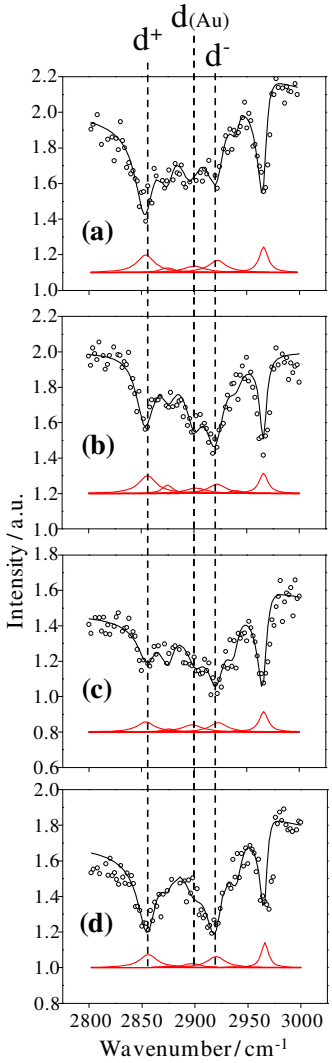

Figure 6.3 SFG spectra of (a) ≡Si-$(CH_2)_9CH_3$ (C10), (b) ≡Si-$(CH_2)_{11}CH_3$ (C12), (c) ≡Si-$(CH_2)_{13}CH_3$ (C14), and (d) ≡Si-$(CH_2)_{17}CH_3$ (C18) upon thermal evaporation of gold overlayers (10 nm thick). The solid lines (in black) showed the best fits based on eqs. (1) and (2) to the experimental data (open circles); and the deconvoluted peaks are shown in red at the bottom (see the main text for details).

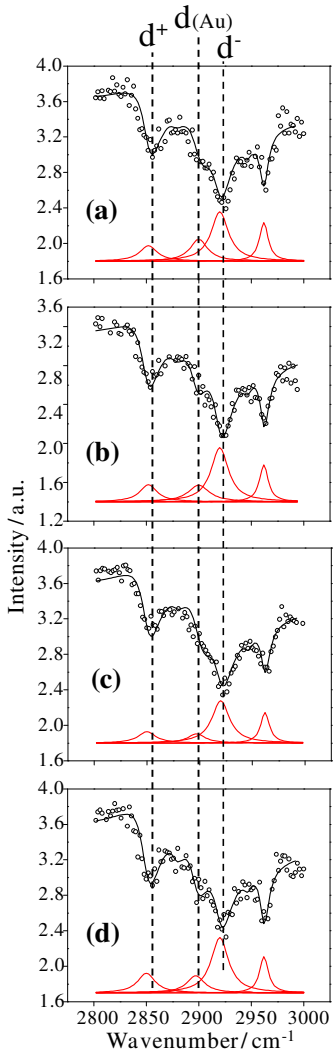

Figure 6.4 SFG spectra of (a) ≡Si-$(CH_2)_9CH_3$ (C10), (b) ≡Si-$(CH_2)_{11}CH_3$ (C12), (c) ≡Si-$(CH_2)_{13}CH_3$ (C14), and (d) ≡Si-$(CH_2)_{17}CH_3$ (C18) upon sputtering deposition of 10 nm-thick gold overlayers. The solid lines (in black) showed the best fits based on eqs. (1) and (2) to the experimental data (open circles); and the deconvoluted peaks are shown in red at the bottom (see the main text for details).

based on their p-polarized backside reflection absorption infrared spectroscopy (pb-RAIRS).[12] It should be noted that in the former system, the monolayers were prepared on GaAs; the stability and molecular orientation of those SAMs are evidently different from the n-alkyl monolayers on silicon as being studied herein. The latter case was regarding the same type, Si-C bonded 1-octadecyl (C18)monolayer on silicon, but prepared under different conditions (using 10 mM solution of 1-octadecene).[12] Although they seemingly contradict our findings, the different preparation conditions for the organic monolayers and metal contacts could lead to radically different results. Our ATR-IR and wetting measurements showed significant differences in the packing and molecular orientation between the n-alkyl monolayers prepared in our work (Table 6.1 and Figure 6.2) and the C18 monolayer reported in their research.[12] The morphology of the gold contacts deposited on top as revealed by our previous STM studies[17] is also different from that reported by Hacker et al.,[12] suggesting different interactions between the metal film on the organic monolayers could exist. While it is difficult at this stage to conclusively determine the cause of the discrepancy, it is important to note that our results mostly support the conclusion drawn by Hacker et al.,[12] as the deposited gold atoms penetrates the monolayer and directly contact the underlying silicon.

6.3.2 Effect of metal deposition methods

In order to provide further insights into how different metal coating methods influence the molecular conformation of SAMs at buried interfaces, the intensity ratio of the methyl symmetric and asymmetric stretches $A_q(r^-)/A_q(r^+)$ was used to estimate the average tilt angle using the following equation:[33-35]

$$\left|\frac{A_q(r^-)}{A_q(r^+)}\right| = \left|\frac{\beta_{caa}}{\beta_{aac}} \times \frac{(2F_{zzz} - F_{xxz})(\cos\theta - \cos^3\theta)}{\left(F_{zzz} + \frac{1}{2}F_{xxz}(1+r)\right)\cos\theta - F_{zzz} - F_{xxz}(1-r)\cos^3\theta}\right| \quad (4)$$

where θ is the angle between the main axis of the methyl group and the surface normal, F_{zzz}, F_{xxz} are the combination of Fresnel factors for the SFG, vis, and IR beams, β is the hyperpolarizability and r is the ratio of β_{ccc} / β_{aac} that equals to 0.25. The ratio β_{caa} / β_{aac} has a value of 4.21.[36] This model can be applied to the C_{3v} symmetry for the methyl groups under the assumption that zzz and xxz elements of the susceptibilities dominate the SFG signal (e.g., the case of gold/silicon interfaces).[37] The detailed description of such model is available in Appendix IV.

$$F_{zzz}, F_{xxz} >> F_{xzx}, F_{zxx} \quad (5)$$

Therefore, the tilt angle determined using Eq. (4) is not applicable to the silicon substrate; it is only valid after deposition of gold as the electric field of the z component will be significantly enhanced. Rather than a particular or an averaged tilt angle, it is more realistic to estimate the distribution of the methyl tilt angles for the each monolayer system. Generally, a Gaussian distribution can used to model the methyl orientation angles (Figure 6.5).[38-40]

$$f(\theta) = C\exp[-(\theta - \theta_0)/2\sigma^2)] \quad (6)$$

where θ_0 is the mean orientation angle, C is the normalization constant, and σ is the root-mean square width. For a direct comparison, the obtained methyl tilt angles and their

distribution from σ = 0º up to 30º for n-alkyl monolayers at gold/silicon interfaces are summarized in Table 6.2.

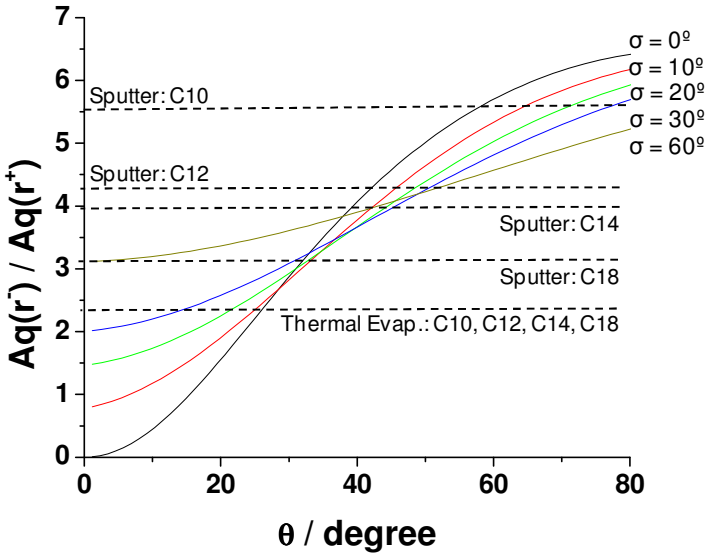

Figure 6.5 The plot of ($A_q(r^-)$/ $A_q(r^+)$) vs. tilt angle (θ) as calculated based on the eq. (4) in the main text.

Sample	Tilt Angles (Thermal evap.)	Tilt Angles (sputtering)
≡Si-$(CH_2)_9CH_3$ (C10)	18-28°	62-80°
≡Si-$(CH_2)_{11}CH_3$ (C12)	18-28°	46-66°
≡Si-$(CH_2)_{13}CH_3$ (C14)	18-28°	41-49°
≡Si-$(CH_2)_{17}CH_3$ (C18)	18-28°	33-36°

Table 6.2 Estimated methyl tilt angles (θ) of n-alkyl monolayers at gold / silicon interfaces; the range was determined based on the assumption of Gaussian Distributions (see text for details).

The average tilt angles of the alkyl chains in n-alkyl monolayers on silicon were reported to be 35-40º,[20, 22, 37] which correspond to the methyl tilt angles of 70-75º. This means that the alkyl molecules are becoming less tilted, i.e., "standing up" from the surface upon metal deposition (Table 6.2). We note that the absolute tilt angles of the monolayers are difficult to determine due to the existence of gauche defects and the wide range of possible orientations, rather we focused on the difference between the two sets of samples. As shown in Table 6.2, the distribution of methyl tilt angles for the samples prepared via thermal evaporation are much narrower than those prepared by sputtering deposition, and their values are within the range of 18-28º, disregarding the different alkyl chain lengths. On the other hand, the distribution of tilt angles of methyl groups for the samples prepared via sputtering deposition exhibited a chain length dependence; the tilt angles becomes smaller as the chain length increased from C10 to C18 (i.e., the tilt angle is larger for the shorter chain monolayer). Such variations likely arose from different structural changes induced by the sputtering deposition and thermal evaporation of the gold overlayers to the identically prepared n-alkyl monolayers on silicon.

In the case of thermal evaporation, the solid metal melts and evaporates in the crucible mounted at the bottom of a vacuum chamber; the metal vapour consequently condenses and deposits on to the sample; it is considered to induce a certain level of damage to the organic monolayer because of the high energy of the gradually condensed metal atoms.[41] The fact that the n-alkyl monolayers on silicon buried underneath these prepared gold contacts have an identical but small tilt angle, may be due to the thermal expansion of the monolayers during the gold evaporation process. It is known that the alkyl chains in relatively compact monolayers expand with the increasing substrate

temperature, consequently causing the decrease in the tilt angle of the monolayer (i.e., standing up from the substrate).[37, 42] This means that irrespective of the chain length, all the monolayers will stand up vertically on the substrate upon metal deposition, i.e., the methyl tilt angles of monolayers become much smaller in comparison with the value prior to the deposition. The heating effect may be due to the thermal radiation of the melting gold source, which makes the molecules more mobile (Figure 6.6, as evidenced by the new CH_2 vibration band).

In the case of sputtering deposition, gold atoms are "dislocated" from the source (target) as struck by the high-energy ions generated by magnetron assisted DC plasma. The "emitted" high-energy, neutral metal atoms then travel toward the sample situated on the opposite side of the chamber. Sputtering is considered to be a more energetic process compared to thermal evaporation, as the kinetic energy of ions are transferred to the metal atoms that are being ejected. The thermal expansion of monolayer

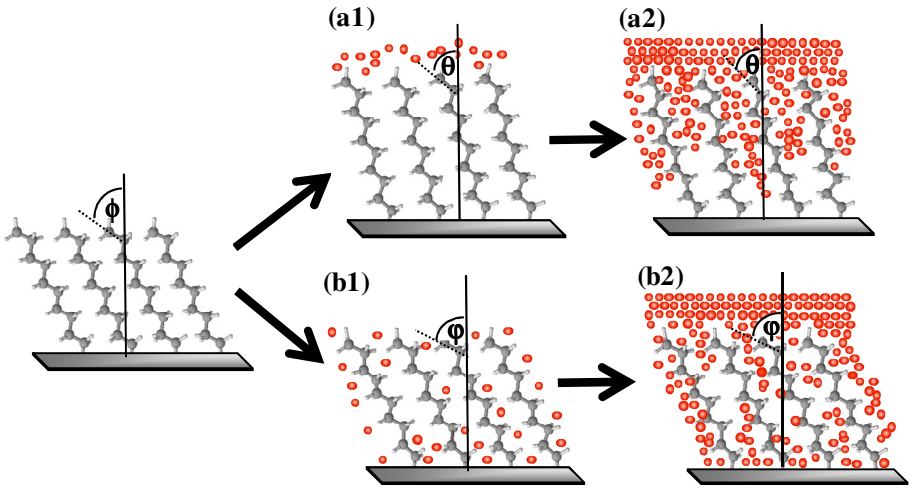

Figure 6.6 A hypothetical view of the monolayer-metal interaction during gold deposition via (a) thermal evaporation and (b) sputtering deposition.

will be minimized in this case as the source being kept cold; however, the high kinetic energies allow the metal atoms to penetrate through the monolayers more readily relative to the thermal evaporation process (Figure 6.6, b1). The different tilting angles upon sputtering gold on top of n-alkyl monolayers on silicon indicate that the monolayers respond to the bombarding by the high energy gold atoms differently; while the shorter chain monolayer (i.e., C10) will simply retain its original tilt angle, the longer alkyl chains may be reoriented upon metal penetration. As the gaps between molecules are slowly occupied by the metal atoms in this case, the molecules gradually stand up. The affinity between methylene groups and gold atoms has been demonstrated previously;[32] therefore longer alkyl chains would certainly limit the mobility of gold atoms within the monolayer.

6.3.3 Electrical measurements

It is evident that both deposition methods result in gold penetration into the monolayers and induce gauche defects within alkyl chain backbones (Figure 6.6). However, the structural deformation of the organic monolayers at the buried interfaces differs significantly as suggested by the above SFG investigations. These structural differences were also reflected in the electrical properties of the formed Au/n-alkyl monolayer/Si junctions; Figure 6.7 shows the representative current density (*J*) versus bias voltage (*V*) plots. All of the samples that were prepared via thermal deposition exhibited clear rectifying behaviour (Figure 6.7). The effective barrier heights and ideality factors were determined based on the thermoionic emission model (see 6.2.4) and

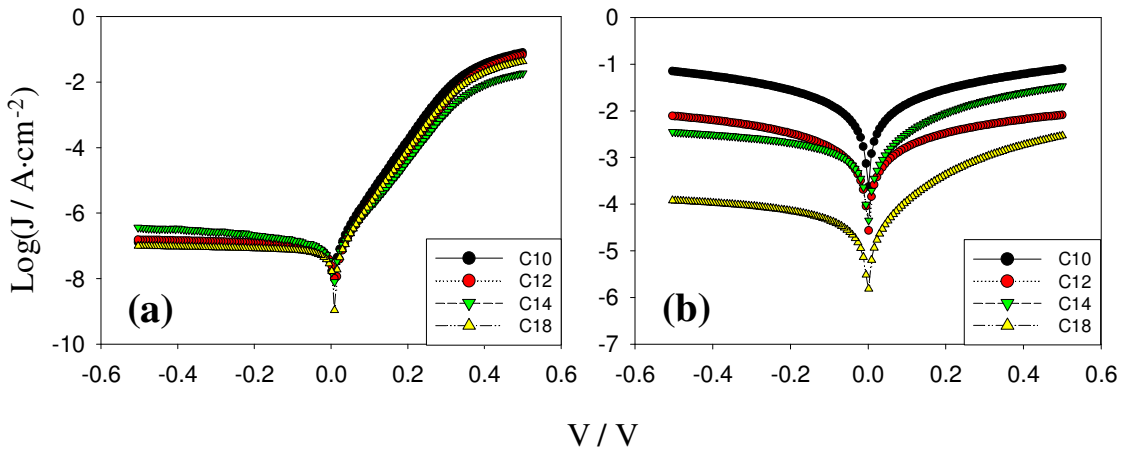

Figure 6.7 Current density-bias voltage (*J*-*V*) plots of Au/n-alkyl monolayer/Si junctions, for which the alkyl chain length was systematically varied. The gold contacts were prepared by (a) thermal evaporation and (b) sputtering deposition, respectively.

Sample	n	$q\phi_{eff}$ / eV	N_d / 10^{15} cm^{-3}	V_{D0} / V
≡Si-$(CH_2)_9CH_3$/Au (C10)	1.21 ± 0.29	0.83 ± 0.06	2.27 ± 0.41	–0.51 ± 0.03
≡Si-$(CH_2)_{11}CH_3$/Au (C12)	1.20 ± 0.26	0.87 ± 0.05	2.17 ± 0.87	–0.63 ± 0.08
≡Si-$(CH_2)_{13}CH_3$/Au (C14)	1.31 ± 0.21	0.89 ± 0.03	1.84 ± 0.29	–0.59 ± 0.01
≡Si-$(CH_2)_{17}CH_3$/Au (C18)	1.25 ± 0.38	0.86 ± 0.02	1.89 ± 0.32	–0.55 ± 0.03

Table 6.3 Solid-state electrical characterization of Au/n-alkyl monolayer/Si junctions.

summarized in Table 6.3. The average values for the four monolayer systems are slightly different, i.e., a marginal increase was observed for C10 to C14, but the value dropped for C18. Such an insignificant increase of $q\phi_{eff}$ may be due to the depth (extent) of gold penetration being dependent on the monolayer thickness; the drop in $q\phi_{eff}$ for C18 monolayer can be explained by its lower packing density that was indicated by the relatively smaller water contact angle (106 ± 2º). It is important to note that most of the $q\phi_{eff}$ values were equal within the experimental uncertainties; we have shown previously that there was no dependence on the alkyl chain length when the monolayers were prepared via an organometallic route and identical to the Au/H-Si junction.[17] In addition, the rather large uncertainties compared to those previous reported for Hg/ n-alkyl monolayer/Si junctions,[18] indicate the uneven lateral gold penetration. This is also consistent with our SFG observations, i.e., there are C-H bonds that are not in direct contact with the gold atoms.

In contrast, the junctions prepared via sputtering deposition were less rectifying and the current densities are clearly offset when the chain length was varied (Figure 6.7b). The semilog *J-V* curve for C10 is essentially symmetric, which means that such a junction is essentially an ohmic contact. Although the reproducibility of these junctions are not good as the Au contacts prepared from thermal deposition (Appendix VI), the trend was observed; as the chain length increases, the rectifying behaviour became more prominent (i.e., the current at forward bias becomes much higher than that at the revised bias). In principle, a direct Au/Si junction should be rectifying as has been shown in our previous report.[17] The ohmic behaviour of Au/H-Si contact has been previously observed by scanning tunnelling microscopic (STM) studies, which has been attributed to the

induced surface states in the band gap region as a result of direct bonding between gold and silicon.[43] The ohmic behaviour of sputtered samples indicates the strong interactions between gold atoms and the silicon substrates, i.e., high-energy gold atoms penetrate through monolayers and attack the silicon surface, possibly with shallow penetration into the silicon bulk. It is interesting to note that although the penetration occurs to a greater extent, the alkyl chains stay intact and relatively well-oriented; gold atoms are not displacing the surface silicon atoms since such damage will cause a dislocation of the monolayer. As the chain length increases, the degree of gold atom penetration seems to be less, however it is more significant in comparison with the case of thermal evaporation where all junctions showed clear rectifying behaviour. This result is supported by the SFG data which suggests that metal penetration occurs at a slower rate for the longer alkyl chains (reflected by the difference in the tilting angles of the buried monolayers). The loss of clear Au-(molecule)-Si interface was also supported by the fact that linear Mott-Schottky (M-S) curves were not obtained for sputtered samples, while M-S plots for samples prepared via thermal evaporation were linear over a large potential range (Figure 6.8) which is an indication of intact silicon substrates. In particular, the doping density (N_d) and the built-in potential at zero bias (V_{D0}) estimated from M-S plots (Table 6.3) are in good agreement with previously reported values.[17, 44]

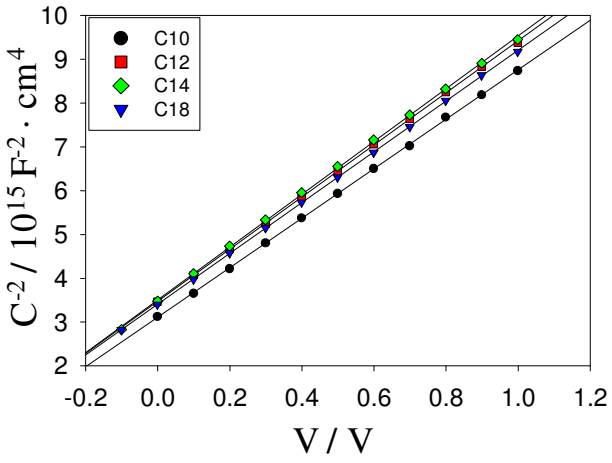

Figure 6.8 Mott-Schottky (M-S) plots of Au/n-alkyl monolayer/Si junctions, for which the gold contacts were prepared via thermal evaporation.

6.4 Conclusion

SFG has shown that gold penetration induces gauche defects to the n-alkyl monolayers prepared on silicon, but the monolayers surprisingly maintain relatively ordered configurations. The gold contact prepared via thermal evaporation and sputtering deposition showed different effects on the monolayer structure; the average tilt angle of methyl groups was similar (~28º) for all of the samples prepared via thermal evaporation, while for the sputtered samples the chain-length dependence was evident. In both cases, the monolayers seem to "stand up" upon gold deposition; for the thermal evaporation this can be explained by the "heating effect" of the radiation source. The sputtering process induces more permanent damages and disordering of the alkyl monolayers; these junctions lose even the rectifying property as a result of strong interactions between gold atoms and the silicon substrate underneath.

Although the extent of damages induced by the conventional metal deposition methods differ, both thermal deposition and sputtering cause enough damage to destroy the "molecular characteristic" of the system. Therefore, it is concluded here that these methods are not feasible for formation of metal contact on the n-alkyl monolayer on silicon.

6.5 Bibliography

(1) Porath, D.; Bezryadin, A.; de Vries, S.; Dekker, C. *Nature* **2000**, *403*, 635.

(2) Martin, C. R.; Baker, L. A. *Science* **2004**, *309*, 67.

(3) Zhirnov, V.V.; Cavin, R.K. *Nature Mater.* **2006**, *5*, 11.

(4) Carroll, R. L.; Gorman, C. B. *Angew. Chem. Int. Ed.* **2002**, *41*, 4378.

(5) Whitesides, G. M. *MRS Bulletin* **2002**, *27*, 56.

(6) Homlin, R. E.; Haag, R.; Chabinyc, M. L.; Ismagilov, R. F.; Cohen, A. E.; Terfort, A.; Rampi, M. A.; Whitesides, G. M. *J. Am. Chem. Soc.* **2001**, *123*, 5075, and references therein.

(7) Flood, A. H.; Stoddart, J. F.; Steuerman, D. W.; Heath, J. R. *Science* **2004,** *306*, 2055.

(8) de Boer, B.; Frank, M. M.; Chabal, Y. J.; Jiang, W. R.; Garfunkel, E.; Bao, Z. *Langmuir* **2004,** *20*, 1539.

(9) Walker, A. V.; Tighe, T. B.; Cabarcos, O. M.; Reinard, M. D.; Haynie, B. C.; Uppili, S.; Winograd, N.; Allara, D. L. *J. Am. Chem. Soc.* **2004,** *126*, 3954.

(10) Jun, Y. S.; Zhu, X. Y. *J. Am. Chem. Soc.* **2004,** *126*, 13224.

(11) Richter, C. A.; Hacker, C. A.; Richter, L. J. *J. Phys. Chem. B* **2005,** *109*, 21836.

(12) Hacker, C. A.; Richter, C. A.; Gergel-Hackett, N.; Richter, L. J. *J. Phys. Chem. C* **2007**, *111*, 9384.

(13) Scott, A.; Hacker, C. A.; Janes, D. B. *J. Phys. Chem. C* **2008**, *112*, 14021.

(14) Strunskus, T.; Grunze, M.; Kochendoerfer, G.; Woll, C. *Langmuir* **1996,** *12*, 2712.

(15) Shen, Y. R. *The Principles of Nonlinear Optics*. John Wiley & Sons: New York, 1984.

(16) Singh, J., *Semiconductor Devices, Basic Principles*. John Wiley & Sons, Inc.: New York, **2001**.

(17) Kuikka, M. A.; Li, W.; Kavanagh, K. L.; Yu, H.-Z. *J. Phys. Chem. C* **2008**, *112*, 9081.

(18) Liu, Y.-J.; Yu, H.-Z. *ChemPhysChem* **2002**, *3*, 799.

(19) Ishibashi, T.; Ara, M.; Tada, H.; Onishi, H. *Chem. Phys. Lett.* **2003,** *367*, 376.

(20) Nihonyanagi, S.; Miyamoto, D.; Idojiri, S.; Uosaki, K. *J. Am. Chem. Soc.* **2004,** *126*, 7034.

(21) Asanuma, H.; Noguchi, H.; Uosaki, K.; Yu, H.-Z. *J. Phys. Chem. B* **2006,** *110*, 4892.

(22) Linford, M. R.; Fenter, P.; Eisenberger, P. M.; Chidsey, C. E. D. *J. Am. Chem. Soc.* **1995,** *117*, 3145.

(23) Faber, E. J.; de Smet, L. C. P. M.; Olthuis, W.; Zuilof, H.; Sudholter, E. J. R.; Bergveld, P.; van den Berg, A. *ChemPhysChem* **2005,** *6*, 2153.

(24) Ishizaki, T.; Saito, N.; SunHyung, L.; Ishida, K.; Takai, O. *Langmuir* **2006,** *22*, 9962.

(25) Sieval, A. B.; Vleeming, V.; Zuilhof, H.; Sudholter, E. J. R. *Langmuir* **1999,** *15*, 8288.

(26) Snyder, R. G.; Strauss, H. L.; Elliger, C. A. *J. Phys. Chem.* **1982,** *86*, 5145.

(27) Macphail, R. A.; Strauss, H. L.; Snyder, R. G.; Elliger, C. A. *J. Phys. Chem.* **1984,** *88*, 334.

(28) Harris, A. L.; Chidsey, C. E. D.; Levinos, N. J.; Loiacono, D. N. *J. Electrochem. Soc.* **1988,** 135, C386.

(29) Tanaka, Y.; Lin, S.; Aono, M.; Suzuki, T. *Applied Physics B-Lasers and Optics* **1999,** *68*, 713.

(30) Messmer, M. C.; Conboy, J. C.; Richmond, G. L. *J. Am. Chem. Soc.* **1995,** *117*, 8039.

(31) Zhu, Z.; Daniel, T. A.; Maitani, M.; Cabarcos, O. M.; Allara, D. L.; Winograd, N. *J. Am. Chem. Soc.* **2006,** *128*, 13710.

(32) Backus, E. H. G.; Bonn, M. *Chem. Phys. Lett.* **2005**, *412*, 152.

(33) Nakamura, T.; Miyamae, T.; Yoshimura, D.; Kobayashi, N.; Nozoye, H.; Matsumoto, M. *Langmuir* **2005,** *21*, 5026

(34) Noguchi, H.; Ito, M.; Uosaki, K. *Chem. Lett.* **2005,** *34*, 950.

(35) Braun, R.; Casson, B. D.; Bain, C. D.; van der Ham, W. M.; Vrehen, Q. H. F.; Ellel, E. R.; Briggs, A. M.; Davies, P. B. *J. Chem. Phys.* **1999**, *110*, 4634.

(36) Watanabe, N.; Yamamoto, H.; Wada, A.; Domen, K.; Hirose, C. *Spectrochim. Acta, Part A* **1994,** *50A*, 1529.

(37) Zhang, L. Z.; Wesley, K.; Jiang, S. Y. *Langmuir* **2001,** *17*, 6275.

(38) Gautam, K. S.; Schwab, A. D.; Dhinojwala, A.; Zhang, D.; Dougal, S. M.; Yeganeh, M. S. *Phys. Rev. Lett.* **2000,** *85*, 3854.

(39) Wang, J.; Chen, C. Y.; Buck, S. M.; Chen, Z. *J. Phys. Chem. B* **2001,** *105*, 12118.

(40) Ye, S.; Morita, S.; Li, G. F.; Noda, H.; Tanaka, M.; Uosaki, K.; Osawa, M. *Macromolecules* **2003,** *36*, 5694.

(41) Haick, H.; Cahen, D. *Prog. Sur. Sci.* **2008**, *83*, 217.

(42) Salomon, A.; Shpaisman, H.; Seitz, O.; Boecking, T.; Cahen, D. *J. Phys. Chem. C* **2008,** *112*, 4169.

(43) Gheber, L. A.; Hershfinkel, M.; Gorodetsky, G.; Volterra, V. *Thin Solid Films* **1998,** *320*, 228.

(44) Asanuma, H.; Bishop, E. M.; Yu, H.-Z. *Electrochim. Acta* **2007,** *52*, 2913.

Chapter 7. Versatile portable device for solid-state electrical measurements of "soft" materials

It is clear from chapter 6 that the conventional metal deposition methods are not applicable for characterizing DNA monolayers on silicon. Therefore we had to devise a more gentle method to form a metal contact to the sample. In this chapter, a versatile and inexpensive portable prototype device for solid-state electrical measurements of "soft" materials is reported. It consists of a custom-made micromanipulator and a gas-tight syringe to hold a mercury mini-drop to make reliable and controllable metal micro-contacts. The electrical contact to the mercury is made by a platinum wire planted into the Teflon tip of the syringe plunger. Compared to the thermal deposition or sputtering, the proposed procedure is simpler, convenient to use, and, most importantly, it is less destructive. The device was tested on various samples, including organically modified silicon, conducting polymers, and thiolated-DNA monolayers on gold. Here, the emphasis is on the performance of the device rather than on the electric measurements performed.

7.1 Introduction

To determine the electrical properties of solid-state materials, it is vital to obtain a reliable and defined contact. An ideal electrical contact should be made of a highly conductive, stable material which is inert to the substrate. In the past, thin films (nanometer to micrometer thickness) of metals such as gold, aluminum, copper, platinum, silver, and tungsten, prepared by vapour deposition or sputtering under high vacuum,[1] were widely used to evaluate the dependence of current and capacitance on the bias voltage.

In recent years, the molecular properties of a new generation of "soft" materials, such as ultrathin organic films (self-assembled monolayers (SAMs) and Langmuir-Blodgett (LB) films), biomembranes and conducting polymers have been utilized for the fabrication of molecularly tunable, miniaturized electronic devices of unprecedented potential.[2,3] Of particular interest is the DNA monolayer on crystalline silicon, which is the focus of this dissertation. It is essential to accurately measure the electrical properties of these "soft" materials in a reproducible and reliable manner.

The electrical characterization of Langmuir-Blodgett (LB) films has been explored since the 1970s' by Mann and Kuhn with the traditional metal deposition protocol.[4] Aluminum, lead and gold were used to form contacts to fatty acid LB films deposited on aluminum substrates. Using a similar method, the conductivity of alkylsiloxane SAMs was investigated by Vuillaume *et al.*[5] In both cases, metal-molecule-metal junctions were successfully fabricated, and the expected electrical performance was observed. The unsolved problem is, as thoroughly investigated in chapter 6, the interaction of the highly reactive condensing metal atoms with the organic molecules

which damages the monolayers and/or alters the surface properties. There is also a high probability of electrical shorting due to defects in the topology of the organic film, i.e., defects or pinholes in the film presumably allow direct metal-to-metal contacts. Therefore, it is difficult to produce reliable and reproducible data for a molecular based system including DNA monolayer on silicon.

A more feasible method is to use a Scanning Tunnelling Microscope (STM) or conductive Atomic Force Microscope (AFM) tips for current-voltage measurements.[6-9] These methods are more reliable and provide high lateral resolution (down to the nanometer range), but the experimental procedures are relatively complex and require sophisticated apparatus. In addition, the interpretation of STM data is often ambiguous due to combined conductivity and topographical changes and the uncontrolled forces applied to the sample.[8] Conductive AFM is a better alternative, since it controls the position of a metal-coated tip with respect to the substrate using a force feedback. However, it is still a challenge to estimate the adhesion force between the surface and the tip (normally associated with contamination), since adhesion leads to hysteresis in the force-distance curve.[9] Furthermore, nanoscale characterization of these surfaces are, in general, not directly translatable into the macroscopic electrical behaviour of the system.

The deposition of silver paint on top of organic monolayers has been suggested to preserve the surface.[10] The silver paint, however, contains both a solvent and a polymer that may contribute to the insulating properties of the material tested. Another method to make metal contacts is the so-called “lift-off, float-on” technique, which consists of peeling a gold film off a glass substrate in dilute aqueous HF solution and then depositing

it on the substrate by "float-on".[11] Major drawbacks are the difficulty of removing solvent trapped between substrate and film.

In order to characterize molecular scale "soft" materials, it becomes vital to construct a simpler and more flexible system for the efficient and reproducible examination of their electronic properties. The use of mercury as metal contact resolves many complications mentioned above. The liquid nature of mercury at room temperature allows it to deform upon contact and conform to the topography of the surface. This allows formation of a contact between the two materials and minimizes the probability of shorting. In addition, the mercury surface is smooth with no grain boundaries, allowing the formation of densely packed, pinhole-free alkanethiolate SAMs that are molecularly tunable.[12] The use of mercury as metal contact was first proposed in the 1950s,[13] and its use as "soft" contact to investigate unique electron transport properties of organic films started more than 30 years ago;[4, 14] the method has recently regained popularity.[15-22] . The hanging mercury drop electrode (HMDE) designed by Guidelli *et al.*[23] consists of a micrometric head with a digital millesimal position sensor, piston, mercury reservoir with inlet, glass capillary and thermostats. It is equipped with monitoring systems which permits the extrusion of mercury droplets with highly reproducible surface areas. Majda and coworkers constructed Hg-Hg junctions from two vertically mounted HMDEs of this type, to investigate the properties of alkanethiolate Hg-SAM/SAM-Hg bilayers .[15-17] These HMDEs are in a glass cell allowing immersion in a desired solution or solvent. Similar electrodes were adopted by Cahen and co-workers for the study of metal-molecule-semiconductor junctions.[22] Aside from their operational complexity, maintenance is also a serious consideration as the capillary tube is easily clogged.

Rampi *et al.* utilized another approach to measure the electric properties of Hg-SAM/SAM-Hg.[18] In their setup, a Hg-column was positioned at the bottom of a microsyringe (for the formation of the first monolayer) , where another Hg drop forms a contact from the top of the solution-filled syringe. They also constructed a simple device for making mercury contacts to measure the electric properties of organic monolayers between two different metal substrates, Hg-SAM/SAM-M', where M' is silver, gold, or copper.[19-21] The set-up consists of a microsyringe, to form a hanging mercury droplet, and a micromanipulator to position the syringe.[19] The mercury drop and metal surface are immersed in alkanethiol solutions to stabilize the SAMs, particularly the monolayers formed on mercury. However, the operation of this apparatus is relatively complicated due to the use of solvent. Solvent may be trapped between the SAMs, and visual estimates of contact areas under a microscope are error-prone due to refraction.

Based on the above-mentioned pioneering studies, we have constructed a versatile prototype device for solid-state electrical measurements that is cost-effective, user-friendly, and applicable to molecular scale "soft" materials.

7.2 Device design

As shown in Figure 7.1, a custom-made micromanipulator and a gas-tight microsyringe are the major components of our device. A platinum wire planted into the Teflon tip of the syringe plunger connects the mercury with the potentiostat (or voltmeter). The approaching process and the x-y positioning of the mercury drop is controlled by the micromanipulator, which is adjusted to micrometer accuracy with the

aid of an optical microscope (modified microscope stand). The size of the mercury drop, which defines the contact area, is controlled by the syringe capacity (100 µL to 1 mL, depending on experimental requirements) and the force applied when the droplet is extruded from the syringe tip. Gas-tight syringes are commercially available at a very reasonable cost. The contact process and size are monitored with a digital microscope (40× to 100×) that is available in most chemistry/physics laboratories. The described modifications to the syringe and the microscope stand are straightforward and do not require special tools.

As will be demonstrated in the following sections, this prototype device permits the measurement of electrical properties of solid-state materials in a fast, routine and non-

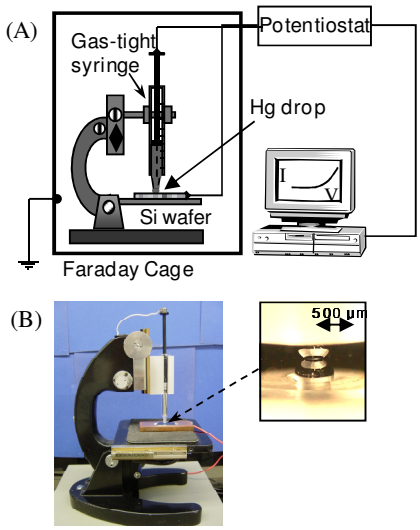

Figure 7.1 (A) Schematic illustration of the prototype device for solid-state electrical measurements. (B) Photographic illustration of the device and the contact (the mercury drop and its mirror image).

destructive fashion. No solvent is used, thus complications noticed in most previously designed systems are minimized. The procedure is simple enough to be performed by non-specialists.

Mercury probes[24-25] are commercially available (for $3500 to $9000); however, the design of our device is by far simpler, considerably less expensive (below $100), and much more convenient to use. In addition, the formation of alkanethiolate SAMs on mercury before the measurements protects the probe, which constitutes an especially advantageous capability of our device.

7.3 Testing

7.3.1 General experimental procedures

The device was tested by studying the electrical properties of organic monolayers and DNA monolayers on silicon. The mercury drop was modified to demonstrate the versatility of the device. Detailed information on the sample preparation can be found in the previous chapters as well as literatures.[26-31]

The microcontacts were made with a 1000-μL gas-tight syringe (Model# 1001, Hamilton Co., Reno, Nevada). The contact process and the area of the mercury drop were monitored with a 40× objective (Model: DM143, Micro-Optic Industrial Group Co., Hong Kong) and the Motic Images 2000 software from the manufacturer. . All current-voltage measurements were carried out with an Autolab Electrochemical Analyzer (Model: PGSTAT30, Eco Chemie BV, Netherlands) in a Faraday cage to minimize the

effects of room-light illumination and electrical noise. At the forward bias, negative voltage was applied to the sample, vice versa for the reverse bias.

7.3.2 Electrical properties of different soft materials

Semiconductor materials, i.e., unmodified and organically modified ("passivated") silicon surfaces (Figure 7.2), were tested first. The contact diameters of the mercury-silicon junctions were usually in the range of 400 μm to 600 μm , corresponding to contact areas of 1.2×10^{-3} to 2.8×10^{-3} cm^2. The typical uncertainty was 20 μm for a 500-μm diameter, which represents a relative uncertainty of less than 10% in the contact area. On unmodified (hydrogen-terminated) silicon, H-Si (a wafer etched in NH_4F to remove oxide layer), the contact size is normally larger than that on organically modified samples.

The current density-bias voltage (J-V) curve of Hg | H-Si exhibited a perfectly linear relationship, as shown on Figure 7.2a. This ohmic behaviour is due to the low barrier height and possible interaction of the mercury with the bare silicon at the interface, and is consistent with previously reported results.[26, 32] The Hg | $C_{10}H_{21}$-Si system (silicon modified with alkyl monolayer) , has a much higher barrier height at the interface and exhibits diode behaviour (Figure 7.2c). Rectifying behaviour is also observed when mercury is protected with an alkanethiolate monolayer (Hg-$SC_{16}H_{33}$ | H-Si(111) junction, see Figure 7.2b). The description of such metal/n-type silicon is available in Appendix V. The measured current density went as low as 10^{-9} A / cm^2 without significant noise, showing the high-sensitivity of our device. Parameters such as interfacial resistance and effective barrier height can be readily extracted from these

measurements. Other electrical tests of semiconducting samples (e.g., differential capacitance-voltage) were also carried out and have been described previously.[28-29]

Similarly, mercury contact on ssDNA-Si was tested. The sample was prepared with a method outlined in chapter 5.2.2 but with 100% undecylinic acid; not a mixed monolayer. The contact area of Hg | ssDNA-Si varied 1.6×10^{-3} to 3.8×10^{-3} cm^2 (450 μm to 700 μm diameter), and the resulting J-V curve is shown in Figure 7.3. The junction shows rectifying behaviour, although the interface appears to be more conducting than the silicon passivated with the alkyl monolayer (Figure 7.2c). This may be due to the high conductance of the DNA samples, however, such speculation is beyond the scope of this chapter; the electrical characterization of DNA monolayer is elaborated in Chapter 9.

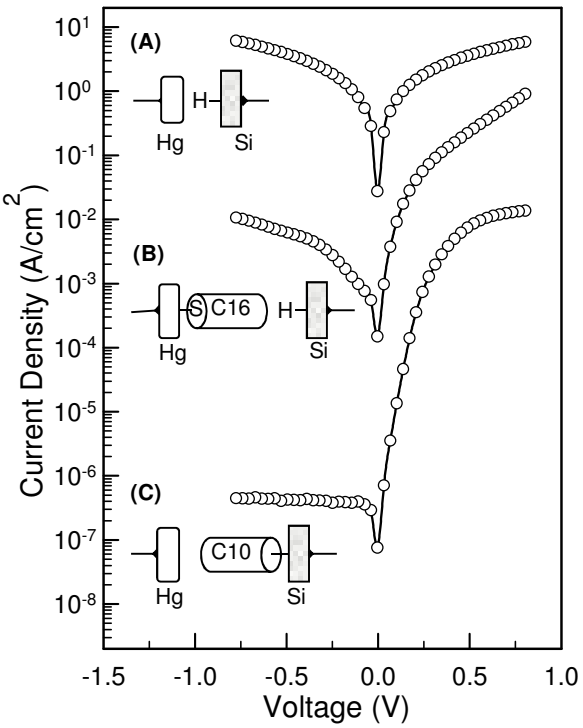

Figure 7.2 Current density-bias voltage (J – V) curves obtained for different semiconductor materials: (a) Hg | H-Si (n-type); (b) Hg-$SC_{16}H_{33}$ | H-Si (111); (c) Hg | $C_{10}H_{21}$-Si (111).

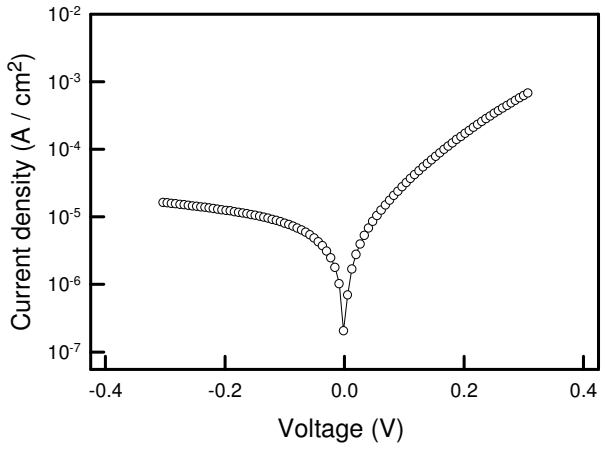

Figure 7.3 Representative current density-bias voltage (J- V) curve for an Hg| ssDNA-Si junction

7.3.3 Monitoring varied conditions

Using the traditional vacuum evaporation technique, it is not practical to prepare metal contacts on solid sample surfaces for electrical measurements over varying exposure periods in order to study the aging effect in the electrical performance of the materials. Our device can handle this task by simply re-positioning the sample to form a new contact at a different spot. This is demonstrated by monitoring the degradation of hydrogen-terminated silicon upon exposure to air under ambient conditions. Figure 7.4 shows the J-V curves of the Hg|H-Si junction at different exposure times. A fresh sample exhibits ohmic characteristics for the first 8-12 hours, then rectifying behaviour becomes dominant. The current density substantially decreases as exposure time increases. Organic contamination has been suggested to play an important role in the electrical degradation of the system.[31] These results are comparable to those obtained with spectroscopic methods.[33]

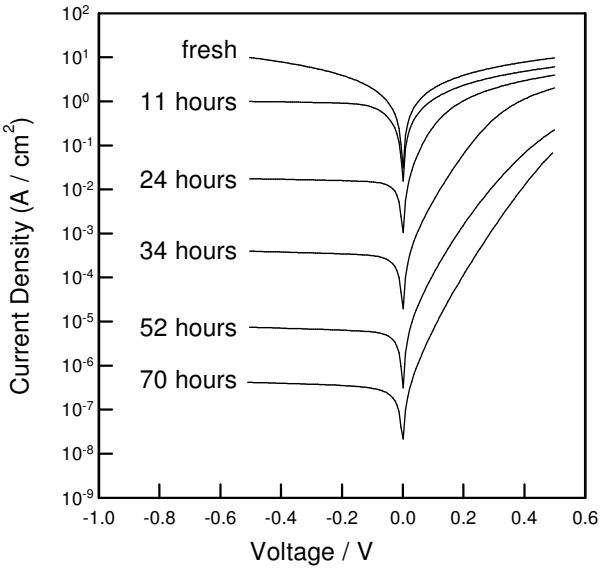

Figure 7.4 Representative J-V plots of the mercury-silicon junctions formed on H-Si(111) and after exposure to air for different periods.

7.3.4 Reproducibility test

Our device has the advantage to prepare multiple microjunctions on the samples to test the reproducibility of the data obtained in the measurements. As shown in Figure 6a, the current density-voltage curves of 20 independent Hg | H-Si junctions from several different samples are very close to each other and perfectly symmetric with respect to zero bias voltage. More than 90% of the junctions exhibited ohmic behaviour . Figure 6b shows the J-V curves of 20 independent Hg | $C_{10}H_{21}$-Si junctions from 12 samples. All of them exhibited rectifying behaviour with a saturated current under reversed bias. Beside the quality of the samples, these experiments unambiguously showed the reproducibility of the measurements carried out with our prototype device.

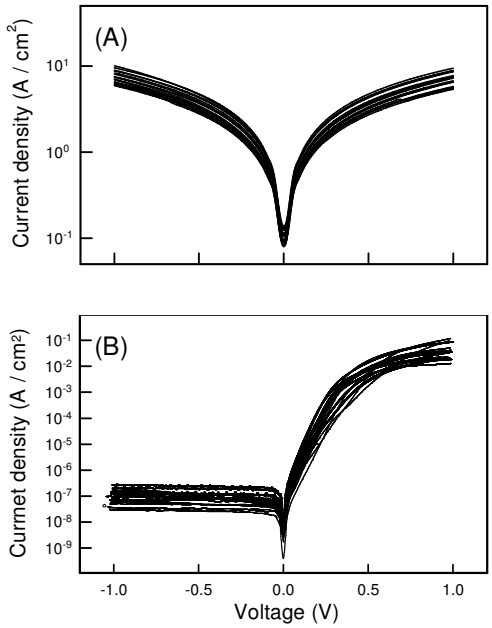

Figure 7.5 Reproducibility test: (A) J-V curves of 20 independent junctions of Hg | H-Si from 15 freshly prepared samples. (B) J-V curves of 20 independent junctions of Hg | C_{10}-Si from 12 samples.

The applicability, versatility and reproducibility of the proposed device for solid-state electrical measurements have been displayed. We have also shown that it is capable of monitoring the electrical performance of a sample as a function of time. We believe that its simplicity and versatility should provide an attractive alternative for the characterization of solid-state materials including DNA monolayer on silicon.

7.4 Bibliography

(1) Manhan, J. P. *Physical Vapour Deposition of Thin Film.* Wiley & Sons: New York , United States, **2000**.

(2) For reviews, see, Whitesides, G. M. *MRS Bulletin* **2002**, *27*, 56; Carroll, R. L.; Gorman, C. B. *Angew. Chem. Int. Ed.* **2002**, *41*, 4378.

(3) For example see, A. Ulman, *An Introduction to Ultrathin Organic Films, from Langmuir-Blodegett to Self-Assembly*. Academic Press: Boston, United States, **1991**.

(4) Mann, B.; Kuhn, H. *J. Appl. Phys.* **1971**, *42*, 4398.

(5) Vuillaume, D.; Boulas, C.; Collet, J. *Appl. Phys. Lett.* **1996**, *68*, 1646 and references therein.

(6) Bumm, L. A.; Arnold, J. J.; Cygan, M. T.; Dunbar, T. D.; Burgin, T. P.; Jones II, L.; Allara, D. L.; Tour, J. M.; Weiss, P. S. *Science* **1996**, *271*, 1705.

(7) Reed, M. A.; Zhou, C.; Muller, C. J.; Burgin, T. P.; Tour, J. M. *Science*, **1997**, *278*, 252.

(8) Klein, D. L.; McEuen, P. L. *Appl. Phys. Lett.* **1995**, *66*, 2478.

(9) Magonov, S. N.; Whangbo, M. H. *Surface Analysis with STM and AFM*. VCH: New York, United States, **1994**.

(10) Maker, M. V.; Landau, J. *Aust. J. Chem.* **1995**, *48*, 1201.

(11) Moons, E.; Bruening, M.; Shanzer, A.; Beier, J.; Cahen, D. *Synth. Met.* **1996**, *76*, 245.

(12) For example of forming alkanethiolate monolayers on mercury, see, Demoz, A.; Harrison, D. J. *Langmuir* **1993**, *9*, 1046.

(13) Baldwin, C. T. *Methods of Electrical Measurement*. Blackie & Son Ltd: London, United Kingdom, **1952**.

(14) Honig, E. P. *Thin Solid Films* **1976**, *33*, 231.

(15) Slowinski, K.; Chamberlain, R. V.; Bilewicz, R.; Majda, M. *J. Am. Chem. Soc.* **1996**, *118*, 4709.

(16) Slowinski, K.; Fong, H. K. Y.; Majda, M. *J. Am. Chem. Soc.* **1999**, *121*, 7257.

(17) Slowinski, K.; Majda, M. *J. Electroanal. Chem.* **2000**, *491*, 139.

(18) Rampi, M. A.; Shueller, O. J. A.; Whitesides, G. M. *Appl. Phys. Lett.* **1998**, *72*, 1781.

(19) Haag, R.; Rampi, M. A.; Holmlin, R. E.; Whitesides, G. M. *J. Am. Chem. Soc.* **1999**, *121*, 7895.

(20) Holmlin, R. E.; Haag, R.; Chabinyc, M. L.; Ismagilov, R. F.; Cohen, A. E.; Terfort, A.; Rampi, M. A.; Whitesides, G. M. *J. Am. Chem. Soc.* **2001**, 123, 5075.

(21) Holmlin, R. E.; Ismagilov, R. F.; Haag, R.; Mujica, V; Ratner, M. A.; Rampi, M. A.; Whitesides, G. M. *Angew. Chem. Int. Ed.* **2001**, *40*, 2316.

(22) Selzer, Y.; Salomon, A.; Cahen, D. *J. Am. Chem. Soc.* **2002**, *124*, 2886.

(23) Becucci, L.; Moncelli, M. R.; Guidelli, R. *J. Electroanal. Chem.* **1996**, *413*, 187.

(24) http://www.4dimensions.com/index.htm, accessed on May 24, 2009.

(25) http://www.mdc4cv.com/, accessed on May 24, 2009.

(26) Liu, Y. J.; Yu, H. Z. *ChemPhysChem* **2002**, *3*, 799.

(27) Asanuma, H.; Noguchi, H.; Uosaki, K.; Yu, H. Z. *J. Am. Chem. Soc.* **2008**, *130*, 8016.

(28) Liu, Y. J.; Yu, H. Z. *ChemPhysChem* **2003**, *4*, 335.

(29) Liu, Y. J.; Yu, H. Z. *J. Phys. Chem. B* **2003**, *107*, 7803.

(30) Liu, Y. J.; Waugh, D. M.; Yu, H. Z. *App. Phys. Lett.* **2002**, *81*, 4967.

(31) Liu, Y. J.; Yu, H. Z. *J. Electrochem. Soc.* **2003**, *150*, G861.

(32) Kampen, T. U.; Mönch, W. *Appl. Phys. A* **1995**, *60*, 391; Kampen, T. U.; Mönch, W. *Surf. Sci.* **1995**, *331*, 490.

(33) Shen, Y., Ichihara, T.; Uosaki, K. *App. Phys. Lett.* **1999**, 75, 1562.

Chapter 8. Electrochemical and solid-state electrical characterization of ω-functionalized organic monolayers on silicon

A handful of silicon samples were characterized with the mercury probe described in chapter 7. However, it must first be demonstrated that the mercury probe can reveal information about the influence of the monolayer on the electric properties of the Hg|monolayer-Si junction. For this purpose, a series of ω-functionalized alkyl monolayers on oxide-free silicon (≡Si-$(CH_2)_{10}COOH$, ≡Si-$(CH_2)_{11}CH_3$, ≡Si-$(CH_2)_{10}COOC_2H_5$, and ≡Si-$(CH_2)_{11}OH$) was prepared and characterized. The insulating effect of a monolayer was confirmed by electrochemical impedance measurements. Solid-state electrical measurements showed that mercury|monolayer-silicon junctions exhibit molecular tunability and a clear correlation between ideality factor and the film thickness / dielectric constant ratio. The barrier height is approximately proportional to the dipole moment of the monolayer. These results create the possibility of fine-tuning the electrical properties of silicon-based microelectronic devices using functionalized organic monolayers.

This chapter is reproduced in part with permission from Asanuma, H.; Bishop, E. M.; Yu, H.-Z. J. *Electrochimica Acta* **2007**, *52*, 2913-2919.

8.1 Introduction

Since the introduction of the first metal-oxide semiconductor field-effect transistor in the 1960s,[1] advances in the design of integrated circuits have been extremely rapid. They are often said to obey Moore's law, which predicts that the number of components on a chip quadruples every three years.[2] At the present rate of downscaling microelectronic devices, the thickness of conventional gate oxide film will reach its fundamental physical limit by the year 2012.[3, 4] Organic materials as media to control charge transport are promising alternatives to silicon oxide, because they are manipulable at scales ranging from angstrom units to nanometres. Silicon is the most important semiconductor used in modern technology; it is of great interest to molecularly control its electrical properties. As described in chapter 1, in the early 1990s Linford et al. prepared n-alkyl monolayers covalently bonded to silicon surfaces by photochemical methods.[5, 6] These monolayers are superior to other thin films (e.g., SAMs on oxidized silicon surface and LB films) because of their great chemical, mechanical, and thermal stability.[5-7]

The electrochemical and solid-state electric properties of these monolayers have not yet been thoroughly investigated. We have found improved insulating behaviour of n-alkyl monolayers on silicon (111) compared to SiO_2 films, and studied the chain-length dependence of its interfacial properties (reciprocal capacitance and effective barrier height).[8-10] More recently, extended study was carried out by Zuilhof and co-workers on silicon (100) surfaces.[11] Cheng et al. have extracted tunnelling constants of electron

transfer from silicon electrodes through alkyl monolayers to decamethylferricenium acceptors.[12] Wei and Zhao have found a non-linear relationship between capacitance and film composition for films prepared from dodecene and methyl undecylenate.[13] By monitoring leakage currents, Miramond and Vuillaume have assessed the effect of substrate doping on the quality of octadecyl monolayers.[14] Faucheu et al. have shown that the higher the molar ratio of carboxy-terminated molecules in mixed carboxy/methyl-terminated monolayers, the larger the effective dielectric constant.[15]

All previous investigations of the molecular tunability of electric properties have focused on the alkyl chain length dependence or the variation of the ratio of alkyl- and carboxy-terminated molecules in the mixed monolayers. There are indications that the intrinsic properties of the adsorbed molecules could also influence the electric properties of the system, as demonstrated in the case of GaAs or organic semiconducting materials.[15-23] In this chapter, we describe the preparation and characterization of a series of ω-functionalized alkyl monolayers on oxide-free silicon (≡Si-$(CH_2)_{10}COOH$, ≡Si-$(CH_2)_{11}CH_3$, ≡Si-$(CH_2)_{10}COOC_2H_5$, and ≡Si-$(CH_2)_{11}OH$). Both electrochemical capacitance (in contact with aqueous electrolyte) and solid-state electrical measurements (by fabricating mercury | ω-functionalized alkyl monolayer | silicon junctions) have been carried out.

8.2 Experimental Section

8.2.1 Materials

All chemicals were of reagent or the highest available commercial grade and used as received unless otherwise stated. Deionized water (>18.3 MΩ·cm) was obtained from a

Barnstead EasyPure UV/UF compact water system (Dubuque, IA). 1-Dodecene (98%), ethyl undecylenate (97%), and sodium borohydride were purchased from Aldrich (Milwaukee, WI); tetrahydrofuran (THF) and 1,1,1-trichloroethane (99.5%) from Caledon Laboratories Ltd. (Georgetown, ON); ammonium fluoride (40%), sulfuric acid (96%), hydrochloric acid (37%) and hydrogen peroxide (30%) from GEM Microelectronic Materials Inc. (Chandler, AZ). 1-Dodecene was distilled from sodium under reduced pressure (20-30 Torr); ethyl undecylenate was purified by passing through an activated Al_2O_3 column.

8.2.2 Sample preparation

Silicon (111) wafers (0.5-5.0 Ω·cm, n-type, Virginia Semiconductor Inc.) and Attenuated total reflectance (ATR) silicon crystals (25 × 5 × 1 mm^3, Harrick Scientific Inc.) were cleaned and etched as previously mentioned (Chapter 3.2.3). The fresh Si-H samples were transferred under argon into Schlenk tubes containing 2-3 mL of deoxygenated neat 1-dodecene or ethyl undecylenate to prepare 1-dodecyl monolayers (≡Si-$(CH_2)_{11}CH_3$) or ester-terminated monolayers (≡Si-$(CH_2)_{10}COOC_2H_5$) by UV irradiation for 3.5 hours (350 nm, 112 W). The modified silicon samples were then rinsed at room temperature with trifluoroacetic acid solution in THF (1%), THF and finally with 1,1,1-trichloroethane. The hydrolysis of ester-terminated monolayers (to prepare carboxylic acid-terminated monolayers, ≡Si-$(CH_2)_{10}COOH$) was carried out in 2.0 M HCl at 70º C for 2 hours. The ester-terminated monolayers were reduced via immersion in deoxygenated 0.5M $NaBH_4$ in methoxyether solution for 2 hours at 85ºC to generate hydroxyl-terminated monolayers (≡Si-$(CH_2)_{11}OH$).

8.2.3 Surface characterization

Wetting measurements were performed as described in Chapter 3.2.4. Ellipsometric measurements were carried out with an Uvisel spectroscopic ellipsometer (Horiba Jobin Yvon) as detailed in Chapter 5.2.3. A bilayer model was used to evaluate the thickness from the ellipsometric data. The dipole moment was calculated by first optimizing the geometry of a single organic molecule immobilized on a cluster of four Si atoms using Mopac (AM1). Then the dipole moment was estimated for the molecule (AM1).[24]

All the electrochemical / electrical characterizations were performed with an Autolab Electrochemical Analyzer (PGstat30, Eco Chemie BV, Netherlands) in a Faraday cage. The differential capacitance-potential measurements were carried out in a custom-designed three-electrode Teflon cell. Silicon samples (working electrode) were pressed against an opening in the cell bottom sealed with an O-ring; and the back contacts (ohmic) were prepared using InGa. The reference electrode was a Pd wire charged in 0.1 M H_2SO_4 at -2.0 V for 3 hours (-0.30 V vs. SCE), and the counter electrode was a Pt wire.[27] The electrolyte solution was 0.1 M H_2SO_4 + 2% HF for all electrochemical impendence measurements. It has been shown that the addition of dilute HF in the aqueous electrolyte retards the oxidation of the modified silicon surfaces, and this solution does not cause significant degradation of the organic monolayers formed on silicon via Si-C linkages.[25-27]

The solid-state electrical measurements were carried out with a home-made mercury-drop device as reported in Chapter 7.[28] The diameters of the contacts were in the range of 400 – 600 μm (uncertainty <10%).

8.3 Results and Discussion

8.3.1 Wetting and thickness measurements

The water contact angles and ellipsometric thicknesses of the ω-functionalized alkyl monolayers on silicon are summarized in Table 1. The larger-than-90° water contact angles obtained for ≡Si-$(CH_2)_{11}CH_3$ are indicative of hydrophobic methyl termination although they are lower than those reported for similar monolayers prepared via other surface reactions.[8, 29, 30] The difference may be due to the partial oxidation of the silicon surface upon UV irradiation since Si-H groups are also prone to oxidation. Nevertheless, the film thickness (13.4 ± 1.4 Å), which is in good agreement with the predicted value supports the conclusion that oriented 1-dodecyl monolayers were formed.[31] The ≡Si-$(CH_2)_{10}COOC_2H_5$ monolayers are less hydrophobic (82.8 ± 1.3°), due to the terminal ester groups.[32, 33] In comparison, the ≡Si-$(CH_2)_{10}COOH$ monolayers (made by ester hydrolysis) are more hydrophilic (50.1 ± 4.4°) and are thinner (i.e., the film thickness decreases from 11.9 ± 1.6 Å to 10.0 ± 1.3 Å upon hydrolysis).

	Water contact angle / degree	Thickness / Å
≡Si-$(CH_2)_{11}CH_3$	94.3 ± 1.4	13.4 ± 1.4
≡Si-$(CH_2)_{10}COOC_2H_5$	82.8 ± 1.3	11.9 ± 1.6
≡Si-$(CH_2)_{10}COOH$	50.1 ± 4.4	10.0 ± 1.3
≡Si-$(CH_2)_{11}OH$	46.4 ± 5.9	16.8 ± 3.2

Table 8.1 Wetting and ellipsometric measurements of ω-functionalized alkyl monolayers on silicon.

The ≡Si-$(CH_2)_{11}$OH monolayers, prepared by the reduction of ester-terminated monolayers, exhibit relatively low contact angles (46.4 ± 5.9°) attributable to the presence of hydrophilic hydroxyl groups; however, the film thickness of 16.8 ± 3.2 Å is larger than that predicted from the chain length of the parent molecule (12.3 Å assuming molecular tilt of 35º).[31] The origin of this higher thickness value is not clear, although we cannot rule out the possibility of partial oxidation during the multistep surface reactions. The formation of high-quality hydroxyl-terminated monolayers on silicon by a similar method has been previously reported by Boukhheroub et al.[34]

8.3.2 Electrochemical impedance measurements

Electrochemical impedance measurements provide information that permits a general assessment of the monolayer structures and a quantitation of the dielectric properties of organic thin films.[35] If a hydrogen-terminated silicon/electrolyte interface is represented by a series of two capacitors (at high frequency) ,[8] the total capacitance is the sum of the reciprocals, that is, $C_{tot}^{-1} = C_{SC}^{-1} + C_H^{-1}$, where C_{SC} is from the space charge layer of the semiconductor, and C_H is the Helmholtz double-layer capacitance at the electrode/electrolyte interface. In the case of depletion ($E > E_{fb}$ for n-type semiconductors), the total capacitance C_{tot} is dominated by C_{SC} (that is much smaller than C_H); therefore, the Mott-Schottky relationship is established.[27]

$$C_{SC}^{-2} = \frac{2}{q\varepsilon\varepsilon_0 N_d A_{elect}^{2}}\left(V - V_{fb} - \frac{kT}{q}\right) \quad \textbf{(1)}$$

Here q is the electronic charge, ε is the dielectric constant of silicon, ε_0 is the permittivity of free space, N_d is the dopant density, A_{elect} is the area of the electrode, V is the applied potential, V_{fb} is the flatband potential, k is the Boltzmann constant, and T is the temperature. At a potential that is more negative than the flatband potential ($V < V_{fb}$), an accumulation region will be formed at the n-type semiconductor | electrolyte interface. The space charge capacitance C_{SC} will exponentially increase as the potential shifts to the negative direction (equation 2), allowing C_H to dominate the total capacitance.[8, 36]

$$C_{SC} = \left(\frac{q^2\varepsilon\varepsilon_0 N_d}{2kT}\right)^{1/2} \exp\left(\frac{-q(V - V_{fb})}{2kT}\right) \quad \textbf{(2)}$$

In order to evaluate the dielectric properties of organically modified silicon, contributions from the monolayers must be considered. An organic thin film can be viewed as a capacitor between the semiconductor and the electrolyte, because monolayers are generally homogeneous (film thickness, composition, and molecular orientation). To account for the defects within the film, a resistor can be incorporated in parallel to the differential capacitance of the monolayer (C_m), leading to equation (3):[8]

$$C_{tot}^{-1} = C_{SC}^{-1} + C_m^{-1} + C_H^{-1} \quad \textbf{(3)}$$

Figure 8.1 shows the results of differential capacitance-potential measurements with organically modified silicon (111) electrodes in contact with 0.1 M H_2SO_4 + 2% HF; the electrode potential is normalized to the flatband potential (determined from the Mott-

Schottky measurements, Figure 8.1b). As mentioned above, the total capacitance should represent C_H when $V < V_{fb}$ for the Si-H | electrolyte system.

Unfortunately, a clear "plateau" (saturation capacitance) is not observed due to hydrogen evolution, and the capacitance increases at a steep rate.[8, 27] The total capacitance (in turn C_H), however, was estimated by determining the turning point between the initial rise of capacitance and the pseudoplateau before the abrupt hydrogen evolution. The value of C_H of Si-H was found to be 3.4 ± 0.8 $\mu F \cdot cm^{-2}$, which is in good agreement with previously reported results.[8, 27]

As shown in Figure 8.1(a), silicon electrodes modified with ω-functionalized monolayers showed more pronounced "plateaus", leading to a more accurate estimation of the valve of C_{tot} from each curve. It is commonly observed for these modified silicon surfaces that hydrogen evolution occurs at more negative potentials than that of Si-H because of the passivation/blocking effect of the organic monolayers. The differential capacitances of the ω-functionalized alkyl monolayers (C_m) were calculated from equation (3) assuming that C_H is unaffected by the presence of organic films (Table 8.2).

Figure 1(b) shows the Mott-Schottky plots for the above systems; the values of flatband potential E_{fb} and dopant density N_d were derived by fitting the linear portion of each curve. Thus obtained N_d values are close to each other and in good agreement with the direct resistance measurements. The flatband potentials (V_{fb}) for ≡Si-$(CH_2)_{11}CH_3$ and ≡Si-$(CH_2)_{10}COOC_2H_5$ are close to the value for Si-H (- 0.42 ± 0.04 V); in contrast, the values for ≡Si-$(CH_2)_{11}OH$ (-0.50 V) and ≡Si-$(CH_2)_{10}COOH$ (-0.52 V) deviate significantly. The fact that the flatband potential of n-Si is not influenced by the immobilization of n-alkyl monolayers[8, 9] indicates that the dipole moment introduced by

the end-groups (particular the polar ones, such as -OH and –COOH) of the ω-functionalized monolayers indeed affect the space charge density of the silicon.

	Differential Capacitance			Mott-Schottky	
	C_{tot} (μF/cm^2)	C_m (μF/cm^2)	ε	N_d (10^{15} cm^{-3})	$-E_{fb}$ (V vs. SCE)
≡Si-$(CH_2)_{11}CH_3$	0.9 ± 0.1	1.2 ± 0.2	1.9 ± 0.3	1.8 ± 0.9	0.45 ± 0.03
≡Si-$(CH_2)_{10}COOC_2H_5$	1.7 ± 0.1	3.4 ± 0.1	4.6 ± 0.2	1.7 ± 0.2	0.42 ± 0.03
≡Si-$(CH_2)_{10}COOH$	1.8 ± 0.1	4.0 ± 0.6	4.6 ± 0.7	1.8 ± 0.1	0.52 ± 0.07
≡Si-$(CH_2)_{11}OH$	1.1 ± 0.1	1.7 ± 0.3	3.2 ± 0.5	1.7 ± 0.1	0.50 ± 0.02
Si-H	3.4 ± 0.8 (C_H)	N/A	N/A	2.2 ± 0.3	0.42 ± 0.04

Table8.2 Electrochemical characterization of the Hg | monolayer | Si junctions prepared from the ω-functionalized alkyl monolayers.

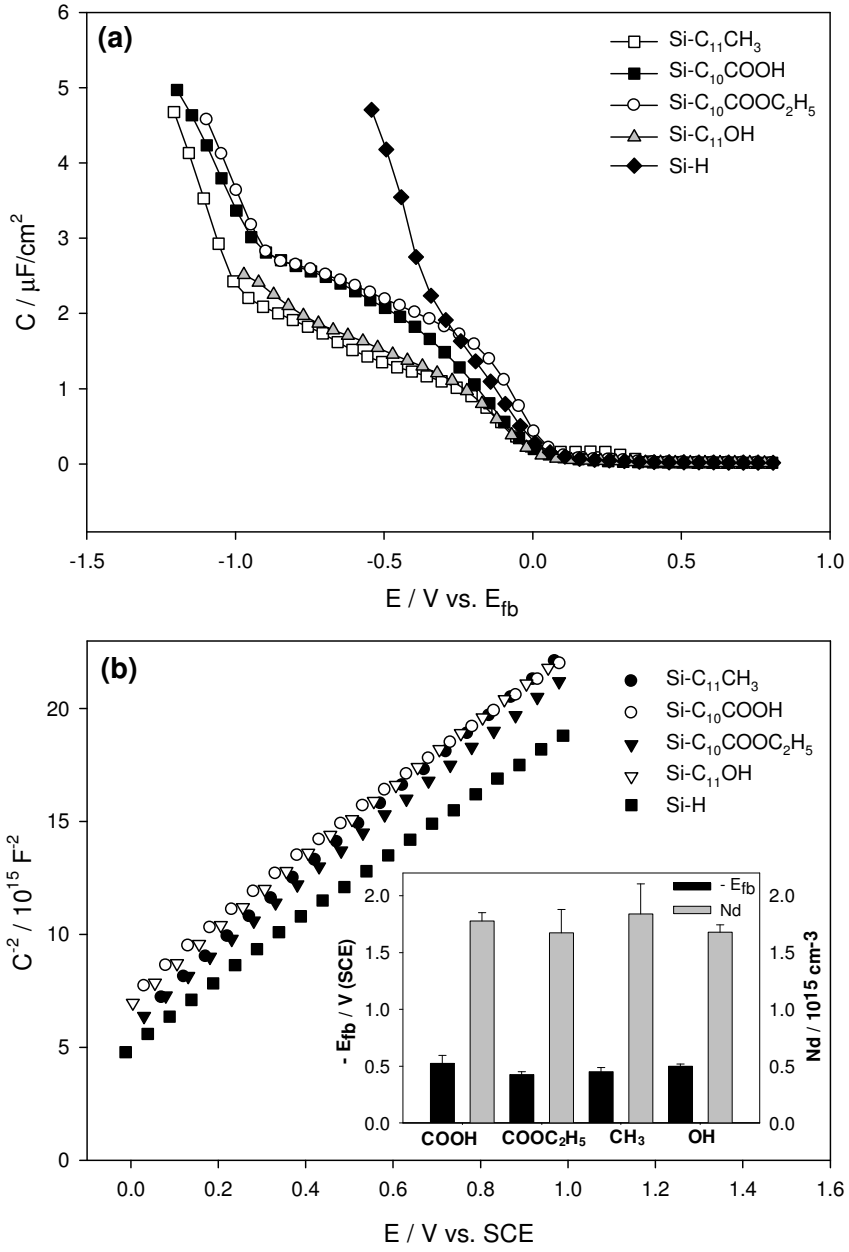

Figure 8.1 a.) Differential capacitance of functionalized Si(111) in contact with 0.1 M H_2SO_4 + 2% HF as a function of flat-band potential at frequency of 1kHz. b.) Mott-Schottky plots obtained with frequency of 50.0kHz.

To further illustrate such an effect, the total capacitances C_{tot} were plotted versus the calculated dipole moments of the parent molecules (Figure 8.2a). The values of the dipole moments used here are not the sums but the components normal to the surface. It is apparent from the plot, that the greater the dipole moment, the higher the C_{tot} (Figure 8.2a). As C_H is assumed to be constant, the difference must arise from the capacitance of the monolayers, C_m:

$$C_m^{-1} = \frac{d}{\varepsilon\varepsilon_0} \qquad \textbf{(4)}$$

The dielectric constants ε of the monolayers can be calculated because the film thickness d is available from the ellipsometric measurements; the results are included in Table 8.2. The dielectric constant of ≡Si-$(CH2)_{11}CH_3$ (1.9 ± 0.3) is in close agreement with the value reported by Faber et al.[11] Figure 8.2(b) shows the correlation between determined dielectric constants and the calculated dipole moments. It is not surprising that when the parent molecule possesses a dipole moment, the dielectric constant of the monolayer becomes much larger. In fact, the relationship between the dipole moment and dielectric constant of a substance is often described by the Debye equation:

$$\frac{\varepsilon - 1}{\varepsilon + 2}\frac{M}{\rho} = \frac{N_A}{3\varepsilon_0}\left(\alpha + \frac{\mu_0^2}{3kT}\right) \qquad \textbf{(5)}$$

where M is the molecular weight, ρ is the molecular density, N_A is the Avoagdro's number and α is the polarizability. This is a simplified equation that neglects polar interactions of dipoles with their surroundings; therefore it may not be directly applicable

to our systems. However, it does show qualitatively that an increase in molecular dipole μ would lead to an increased dielectric constant ε. More interestingly, the dependence of ε on the μ value (Figure 8.2b) shows that it is not the direction of the dipole but the magnitude of the dipole moment that affects the overall dielectric properties of organic monolayers. These results indicate that it is possible to control capacitive properties at interfaces by introducing terminal functional groups to the organic monolayers.

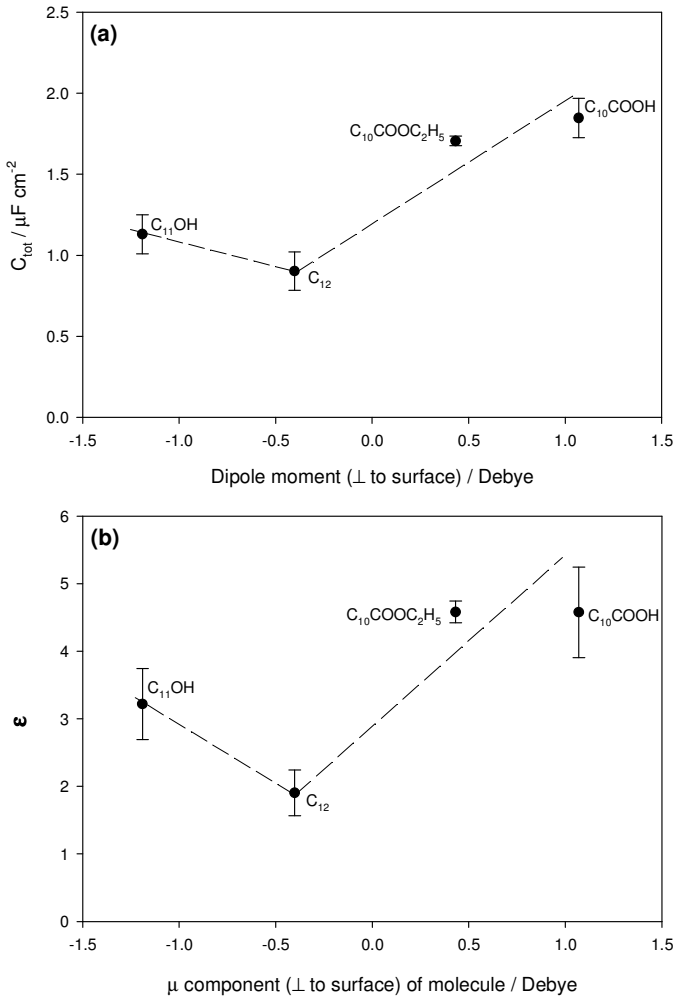

Figure 8.2 a.) Total capacitance Ctot and b.) dielectric constant ε plotted against dipole moment (⊥ to surface). C_{tot} and ε were derived and dipole moment was calculated using semiempirical (AM1) method (see text).

8.3.3 Solid state measurements via the formation of mercury | monolayer | silicon junctions

We further tested the electrical properties of ω-terminated alkyl monolayers on silicon by preparing Hg | monolayer | Si junctions, for which the procedure and general characterization were reported previously.[9, 10, 28] The effective barrier height and ideality factor of a Hg | monolayer | Si junction were extracted with method described in Chapter 6.2.4

To account for the intrinsic properties of the monolayer, an extra term has been introduced to compensate for the contribution of the organic monolayers:[9-11, 37]

$$q\phi_{eff} = q\phi_b + kT\beta_{tun}l \qquad \textbf{(8)}$$

Here, ϕ_b is the barrier height resulting from the difference between the energy levels in the metal and in the semiconductor, β_{tun} is the electron-tunnelling constant through the monolayer, and l is the thickness of the monolayer. The barrier height ϕ_b is expressed as: $q\phi_b = q\phi_{metal} - q\chi$; where $q\phi_{metal}$ is the work function of the metal, and $q\chi$ is the electron affinity of semiconductor. The work function is influenced by the surface dipole and can be written as:[16]

$$q\phi_b = q\phi_{metal} - (\chi^0 + q\phi_{dipole}) \qquad \textbf{(9)}$$

where χ is considered to be composed of χ^0 (constant) and ϕ_{dipole} (dipole contribution), and ϕ_{dipole} is expressed as:

$$\phi_{dipole} = \frac{N\mu\cos\theta}{\varepsilon\varepsilon_0} \quad \textbf{(10)}$$

In our case, we must consider both the film thickness (to produce tunnelling barrier) and the dipole moment, because the monolayers consist of different functional groups with different thicknesses. The expression which accounts for both properties can be derived by combining equations (8) and (9).

$$q\phi_{eff} = q\phi_{metal} - (\chi^0 + q\phi_{dipole}) + kT\beta_{tun}l \quad \textbf{(11)}$$

J-V curves of Hg | monolayer | Si junctions are shown in Figure 8.3(a). All the junctions exhibit rectifying behaviour; more significantly, the forward bias current (at the same bias voltage) increases in the order ≡Si-$(CH_2)_{10}COOH$ > ≡Si-$(CH_2)_{11}CH_3$ > ≡Si-$(CH_2)_{10}COOC_2H_5$ > ≡Si-$(CH_2)_{11}OH$. The effective barrier heights and ideality factors were extracted (using equation (7)) from these J-V curves and summarized in Table 8.3. As mentioned above, both the thickness and dipole moment must be accounted for by the effective barrier height (equation 11). In an attempt to analyze the effect of dipole moments on the effective barrier height, the contribution from the thickness ($kT\beta_{tun}l$) was considered first. The structure-dependent attenuation factor, β_{tun}, was taken from previously reported value (0.63 ± 0.10 per CH_2) for Hg | monolayer | Si junctions.[9] The thickness of the monolayers, l, was taken as the number of methylene groups. Figure 8.3(b) shows that the normalized values of barrier heights ($q\phi_{eff} - kT\beta l$) are inversely proportional to the dipole moments. The gradual decrease in the effective barrier height with increasing dipole moment can be explained by equations (9) and (10). As the dipole moment μ increases, ϕ_{dipole} increases and $q\phi_b$ in equation (10) decreases accordingly. This

is consistent with the observations for organically modified Au/GaAs diodes.[16] The change in barrier height induced by the dipole properties of monolayers may be attributed to the change in the silicon space charge density (evident by the shift in V_{fb}).[19]

We also studied the effect of dipole moments on the calculated ideality factors. Assuming that the metal | silicon junctions are free of surface states, the following equation can be used to express the ideality factor:[11, 13]

$$n = 1 + \frac{l\varepsilon_{Si}}{W\varepsilon_{film}} \text{ where } W = \frac{2\varepsilon_0\varepsilon_{Si}}{qN_d(V_{fb} - V_{bias})} \quad \textbf{(12)}$$

If the ideality factor (n) were plotted versus the value l/ε_{film}, a linear relationship with an intercept of unity would be found. Fig. 8.4 shows such a plot, for which the film thickness and the dielectric constant were obtained in section 8.3.1. The plot is apparently linear, and the least-squares fit provides an intercept of 1.00 ± 0.07 that matches the predicted value. These results indicate that these Hg| monolayer| Si junctions do not have significant amount of interface surface states, and the charge transport at the interface is predominately via a thermoionic pathway The discernible deviation of ideality factors of certain junctions, particularly ≡Si-C_{11}OH from the linearity may be due to the partial oxidation of the silicon surface, which is consistent to the above-mentioned ellipsometric and wetting observations.

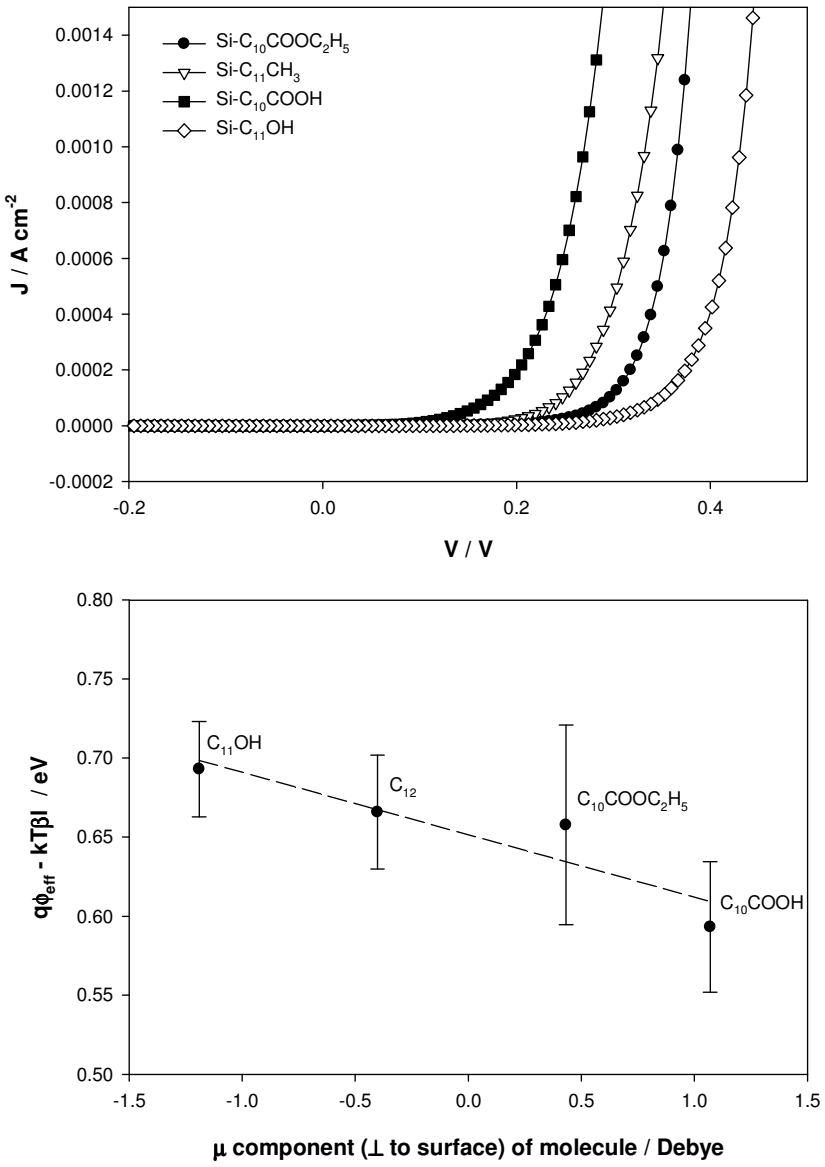

Figure 8.3 The current density-voltage (J-V) curves of Hg/monolayer-Si junctions. b.) The barrier height (with film thickness factor incorporated) plotted against the dipole moment (see text).

	Ideality factor		Barrier height	
	n	l/ε_{film}	$q\phi_{eff}$ (eV)	$q\phi_{eff} - kT\beta l$ (eV)
≡Si-$(CH_2)_{11}CH_3$	1.39 ± 0.06	1.9 ± 0.3	0.84 ± 0.02	0.67 ± 0.04
≡Si-$(CH_2)_{10}COOC_2H_5$	1.16 ± 0.04	4.6 ± 0.2	0.87 ± 0.05	0.66 ± 0.06
≡Si-$(CH_2)_{10}COOH$	1.14 ± 0.62	4.6 ± 0.7	0.77 ± 0.03	0.59 ± 0.04
≡Si-$(CH_2)_{11}OH$	1.39 ± 0.08	3.2 ± 0.5	0.87 ± 0.01	0.69 ± 0.03

Table 8.3 Solid-state electrical characterization of the Hg | monolayer | Si junctions prepared from the ω-functionalized alkyl monolayers.

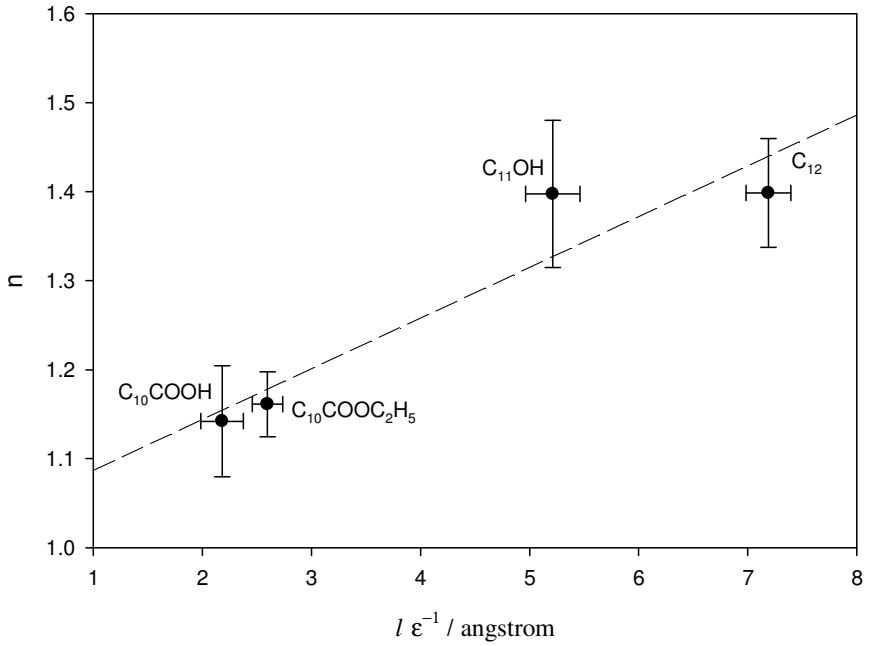

Figure 8.4 The ideality factor n plotted against film thickness/dielectric constant $l \cdot \varepsilon^{-1}$. The film thickness was estimated from ellipsometric measurements, dielectric constant

8.4 Conclusion

ω-Functionalized alkyl monolayers on oxide-free silicon (111) (≡Si-$(CH_2)_{10}COOH$, ≡Si-$(CH_2)_{11}CH_3$, ≡Si-$(CH_2)_{10}COOC_2H_5$, and ≡Si-$(CH_2)_{11}OH$) were prepared via photochemical reactions and characterized by electrochemical / solid-state electrical measurements. Differential capacitance-voltage studies revealed that all of the monolayers are of high quality and the obtained dielectric constants are influenced significantly by the dipole moments of the end groups. The custom made mercury probe successfully revealed the current density-voltage curves of the diode junctions. They displayed expected rectifying behaviour and the ideality factors of the junctions were dictated by the film thickness and the dielectric constant of the monolayer. The effective barrier heights were tuned by the introduction of functional groups in the monolayers.

8.5 Bibliography

(1) Kahng, D.; Atalla, M. US Patents 3206670 and 3102230, US, **1960**.

(2) Moore, G. E. *Int. Elec. Devices Mtg (IEDM) Technical Digest* **1975**, *75*, 11.

(3) Muller, D. A.; Sorsch, T.; Moccio, S.; Baumann, F. H.; Evans-Lutterodt, K.; Timp, G. *Nature* **1999**, *399* , 758.

(4) Schulz, M. Nature **1999**, *399* , 729.

(5) Linford, M. R.; Chidsey, C. E. D. *J. Am. Chem. Soc.* **1993**, *115*, 12631.

(6) Linford, M. R.; Fenter, P.; Eisenberger, P. M.; Chidsey, C. E. D. *J. Am. Chem. Soc.* **1995**, *117*, 3145.

(7) Sung, M. M.; Kluth, G. J.; Yauw,O. W.; Maboudian, R. *Langmuir* **1997**, *13*, 6164.

(8) Yu, H. Z.; Morin, S.; Wayner, D. D. M.; Allongue, P.; Henry de Villeneuve, C. *J. Phys. Chem. B* **2000**, *104*, 11157.

(9) Liu, Y. J.; Yu, H. Z. *ChemPhysChem* **2002**, *3*, 799.

(10) Liu, Y. J.; Yu,H. Z. *ChemPhysChem* **2003**, *4*, 335.

(11) Faber, E. J.; de Smet, L. C. P. M.; Olthuis, W.; Zuilhof, H.; Sudhölter, E. J. R.; Bergveld, P.; van den Berg, A. *ChemPhysChem* **2005**, *6*, 2153.

(12) Cheng, J.; Robinson, D. B.; Cicero, R. L.; Eberspacher, T.; Barrelet, C. J.; Chidsey, C. E. D. *J. Phys. Chem. B* **2001**, *105*, 10900.

(13) Wei, F.; Zhao, X. S. *Thin Solid Films* **2002**, *408*, 286.

(14) Miramond, C.; Vuillaume, D. *J. Appl. Phys.* **2004**, *96*, 1529.

(15) Faucheu, A.; Gouget-Laemmel, A.C.; de Villeneuve, C. H.; Boukherroub, R.; Ozanam, F.; Allongue, P.; Chazalviel, J. N. *Langmuir* **2006**, *22*, 153.

(16) Villan, A.; Shanzer, A.; Cahen, D. *Nature* **2000**, *404*, 166.

(17) Haick, H.; Ambrico, M.; Ligonzo, T.; Cahen, D. *Adv. Mater.* **2004**, *16*, 2145.

(18) Haick, H.; Ghabboun, J.; Niitsoo, O.; Cohen, H.; Cahen, D.; Vilan, A.; Hwang, J.; Wan, A.; Amy, F.; Kahn, A. *J. Phys. Chem. B* **2005**, *109*, 9622.

(19) Vearery-Roberts, A. R.; Evans, D. A. *App. Phys. Lett.* **2005**, *86*, 072105.

(20) Kampen, T. U.; Park, S. Zhan, D. R. T. *App. Surf. Sci.* **2002**, *190*, 461.

(21) Bolognesi, A.; Carlo, A. D.; Lugli, P.; Kampen, T.; Zahn, D. R. T. *J. Phys.: Condens. Matter* **2003**, *15*, S2719.

(22) Çakar, M.; Onganer, Y.; Türüt, A. *Synth. Met.* **2002**, *126*, 213.

(23) Çakar, M.; Türüt, A. *Synth. Met.* **2003**, *128*, 549.

(24) http://www.semichem.com/ampacmanual/methods.html, accessed on August 25, 2009.

(25) Allongue, P.; Henry de Villeneuve, C.; Pinson, J. O.; Chazalviel, J. N.; Wallart, X. *Electrochim. Acta* **1998** *43*, 2791.

(26) Henry de Villeneuve, C.; Pinson, J.; Bernard, M. C.; Allongue, P. *J. Phys. Chem. B* **1997**, *101*, 2415.

(27) Allongue, P.; Henry de Villeneuve, C.; Pinson, J. *Electrochim. Acta* **2000**, 45, 3241.

(28) Asanuma, H.; Liu, Y. J.; Yu, H. Z. *Jpn. J. Appl. Phys.* **2005**, *44*, 1991.

(29) Zhang, L.; Li, L.; Chen, S.; Jiang, S. *Langmuir* **2002**, *18*, 5448.

(30) Sieval, A. B.; Optiz, R.; Maas, H. P. A.; Schoeman, M. G.; Meijer, G.; Vergeldt, F. J.; Zuilhof, H.; Sudhölter, E. J. R. *Langmuir* **2000**, *16*, 10359.

(31) The monolayer thickness was predicted using equation, $d = 1.86 + d_0 \cos\theta$, where d_0 is the molecular length. The predicted thickness for ≡Si-$(CH2)_{11}CH_3$, 13.6Å (with tilt angle of 35°) is in good agreement with the experimental value. On the other hand, the predicted thickness for ≡Si-$(CH2)_{11}OH$, 12.3 Å, is lower than the experimental value.

(32) Sieval, A. B.; Demirel, A. L.; Nissink, J. W. M.; Linford, M. R.; Van der Maas, J. H.; De Jeu, W. H.; Zuilhof, H.; Sudhölter, E. J. R. *Langmuir* **1998**, *14*, 1759.

(33) Liu, Y. J.; Navasero, N. M.; Yu, H. Z. *Langmuir* **2004**, *20*, 4039.

(34) Boukherroub, R.; Wayner, D. D. M. *J. Am. Chem. Soc.* **1999**, *121*, 11513.

(35) Gerischer, H. *Electrochim. Acta* **1990**, *35*, 1677.

(36) Bansal, A.; Lewis, N. S. *J. Phys. Chem. B* **1998**, *102*, 1067.

(37) Selzer, Y.; Salomon, A.; Cahen, D. *J. Phys. Chem. B* **2002**, *106*, 10432.

Chapter 9. Conclusions and future work

9.1 Concluding Remarks

It has been demonstrated in this thesis that bioreactive semiconductor surfaces can be prepared via controlled surface chemistry and that their structures can be assessed using either advanced spectroscopic or solid-state electrical measurements. The conventional method to prepare ω-carboxy monolayers on silicon has limitations in terms of the reaction complexity (chapter 3). It has been shown that the surface hydrolysis is incomplete and its efficiency depends on the size of the terminal ester groups. More importantly, the hydrolysis reaction disrupts the monolayer integrity and molecular orientation, i.e., thus prepared ω-carboxy monolayers on silicon are less ordered than their alkyl counterparts. Examination of the reaction kinetics of n-alkene and 1-undecanoic acids with silicon led to the discovery of an alternative method to prepare carboxy-terminated monolayers on silicon (chapter 4), i.e., direct photochemical reaction between undecylenic acids and ≡Si-H surface for a controlled period of time.

DNA molecules are known to undergo conformational changes, particularly when the cations are changed; such phenomena are well documented in solution phase but not with DNA strands immobilized on chips. In chapter 5, it was shown that DNA strands can be immobilized on silicon surfaces by amide coupling between amine-functionalized DNA and carboxy-terminated monolayers on silicon. Our SFG spectroscopy

investigations have revealed that the type and concentration of metal cations directly affect both the immobilization of DNA strands on silicon and the subsequent hybridization with complementary targets. Divalent cations (Ca^{2+} and Mg^{2+}) induce greater DNA deformation (bending toward the surface instead of projecting into the solution) and disrupt the underlying linker monolayer more significantly compared to monovalent cations (Na^{+} and K^{+}) during the immobilization step; while for the hybridization process, the effect of dications is less remarkable.

The second half of this thesis demonstrates the feasibility of forming reliable metal contacts on bioreactive silicon surfaces and of carrying out reproducible electrical measurements of thus prepared biomolecularly-modified metal-semiconductor junctions. As an initial study (chapter 6), the limitation of traditional preparation protocols to make metal contacts (thermal evaporation and sputtering deposition of gold thin films) on n-alkyl monolayers on silicon has been revealed by combined spectroscopic and electrical measurements. It has been shown that the gold atoms penetrate through originally oriented alkyl chains and induce irreversible structural changes. This "reality" study motivated us to construct a mercury-drop device for solid-state electrical measurements of "soft" materials, which can provide both accurate and reproducible data for electrical measurements (i.e., J-V curves and capacitance) of organic monolayers formed on silicon (chapter 7). This study was then extended to test ω-functionalized monolayers on silicon. In particular, a correlation between interfacial electrical properties (i.e., effective barrier height and ideality factor) and molecular structure (different end-group derivatization) has been confirmed (chapter 8). This opens up a possibility of understanding the conductive behaviour of DNA monolayers on semiconductors by using direct solid-state

electrical measurement, which augments the potential of building DNA-based molecular junctions in the near future.

9.2 Future work

With increasing demands for improvements in integrated circuit design, particularly, in the downscaling of its components, the electronic chip will soon reach their physical size limits. In this regard, molecular electronics are considered as a possible technological solution. A molecular building block can typically be manipulated at length scales ranging from angstroms to nanometres, and thus it allows significant reduction in the size of electronics.[1] DNA is a promising molecule for the design of electric circuit due to its abilities to self-assemble and self-replicate.[2] Furthermore, DNA has been reported to show a wide range of electric responses, and can behave as a conductor, a semiconductor or an insulator. The conducting behaviour of DNA is controlled by the experimental conditions, i.e., DNA sequence, length, orientation, counterions, temperature, and electrode contact.[3]

The feasibility of implementing DNA into an integrated circuit was examined by studying an ssDNA monolayer prepared on silicon with a mercury probe device, as described in chapter 7. The J-V response was successfully measured, and the results are shown in Figure 9.1 along with the J-V curves of Hg|H-Si and Hg|C10-Si junctions.

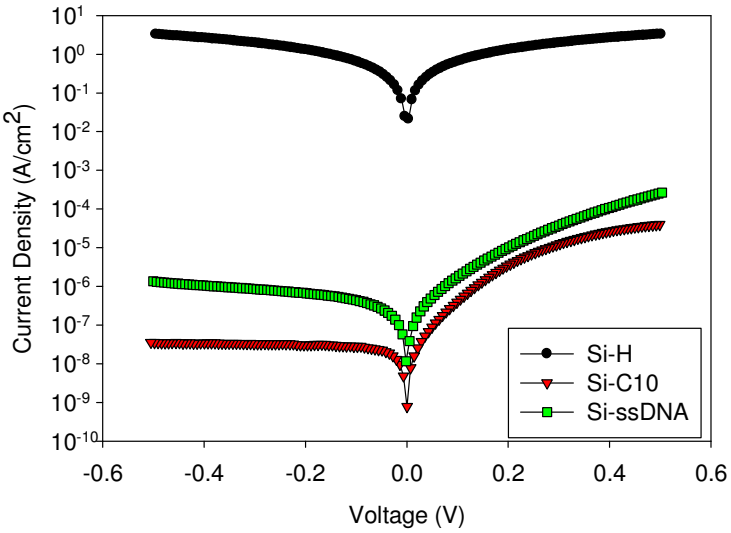

Figure 9.1 J-V curves of Hg|H-Si, Hg|C10-Si and Hg|ssDNA-Si junctions.

The J-V characteristic of the ssDNA-Si clearly differs from that of a C10-Si or an H-Si. Unlike the typical Ohmic-like behaviour of Hg|H-Si junction, the DNA modified junction rectified. More interestingly, the ssDNA-Si junction exhibits higher current density than the alkyl (C10) passivated silicon. Since the length of the linker layer of DNA monolayer is comparable to that of C10 monolayer (Figure 5.1), the higher current density indicates a better conductivity of the DNA monolayer. The DNA is clearly influencing the performance of the formed junction and this has a great implication; the biomolecule can be used as a component of electronic device. However, the low experimental reproducibility observed remains a great challenge, and discourages further discussion regarding the electrical conductivity of DNA monolayer. The low reproducibility is most likely due to variations in the DNA surface density and the mercury-DNA interactions. The surface density of DNA monolayers varies from 5 to 10% within the same sample, and the electrical measurements may reflect such differences. On the other hand, it has

been observed that a mercury drop and a DNA monolayer on silicon attract each other, as evident by the relatively large mercury contact diameters of 500 μm to 800 μm compared to those formed on n-alkyl monolayers (400 μm to 600 μm). This attraction may be facilitated by the mercury adsorption on polynucleotides, and perhaps, intrusion of mercury into the monolayer may have occurred.[4, 5] Nevertheless, the variation in electrical response is believed to arise from the probe sensitivity toward the state of the DNA monolayer. This will be an advantage once the causes of irreproducibility are identified. That said, resolving the uncertainties surrounding the surface densities and the DNA-Hg interactions are challenging.

The surface density of DNA monolayers on polycrystalline gold is more widely studied and found to typically vary from 15 to 30%.[6] Although a more reproducible surface density may be achievable with the atomically flat silicon (111) surface, completely uniform surface coverage is difficult to accomplish; this is especially true for the DNA monolayer in which the immobilization involves multiple steps (Figure 5.1). Indeed, to reduce variation of the surface density, most previously reported electrochemical characterizations of DNA monolayers on surfaces were done without changing the position of electric contact.[7, 8] With the experimental setup of the current device, the mercury contact position with respect to the sample is difficult to maintain constant. The most convenient solution to this problem is to incorporate an X-Y micro-positioning stage at the base of the mercury electrode. This would not only allow a precise positioning of the sample, but could also be extended to probe a DNA microarray. In addition, the accurate positioning of the sample will allow one to readily compare the electric response of a particular junction to the DNA surface density; assuming that the

surface coverage is mapped by means of electrochemistry, radio- or by fluorescent labelling.

The attraction between mercury and the polynucleotide may be another factor that is complicating the electrical response of a Hg|DNA-Si junction. To achieve reliable electrical contact, the mercury must be positioned at the top of the DNA monolayer and not penetrate. Mercury is known to react with most other metals to form an amalgam. The solid gold-mercury or silver-mercury amalgams can act as an excellent electrode; this was demonstrated by Jiranek *et. al.* using silver-mercury alloy as an electrode for electrochemical studies of nitroquinolines.[9] More importantly, the formation of solid mercury alloy as a contact will minimize the mercury-polynucleotide interactions and possibly lead to more reproducible data.

The proposed method uses nanoparticles as precursors for the amalgam formation (Figure 9.2). First, the metal nanoparticles (Au or Ag) suspended in organic solvent (i.e. dichloromethane) will be spray-casted on to the DNA-Si. Spray-casting with an airbrush has been reported to provide a more consistent and uniform nanoparticle film compared to drop-casting.[10] When the mercury contacts the layer of nanoparticles, amalgam will be formed at the interface. The formation of an amalgam and its solidification depend on the ratio of mercury and the metal.[11] Therefore, the amount and size of the nanoparticles on the substrate will likely influence the stability of the alloy; these two parameters in relation to the electric performance of the thus formed junctions require further investigation.

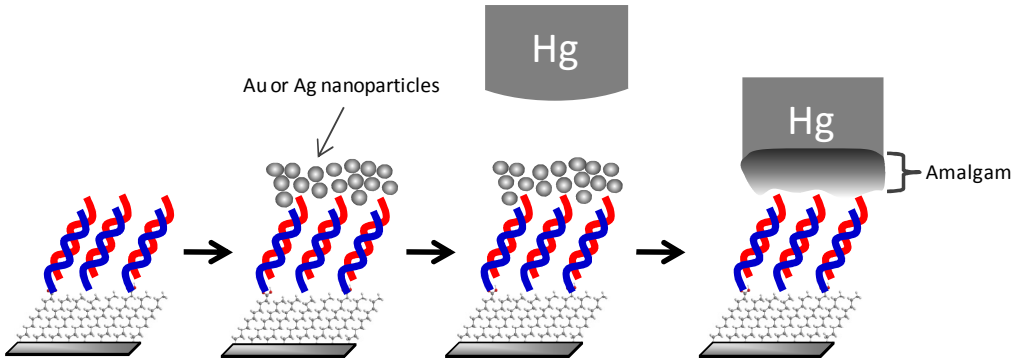

Figure 9.2 A preparation of amalgam electric contact on top of the DNA-Si using metal nanoparticles.

It has been shown that the electron transfer depends on the length and sequence of DNA as well as its conformation.[12] Artificial and secondary DNA structures (i.e. G-wires, DNA loop) most likely exhibit different electric responses. DNAs can also be combined with a wide variety of electrically active molecular elements, such as fullerenes, carbon nanotubes, metal clusters or certain molecular switches.[13] The junctions incorporating these DNA constructs will be interesting to investigate once the reproducibility issues are resolved.

9.3 Bibliography

(1) Flood, A. H; Stoddart, J. F., Steuerman, D. W.; Heath, J. R. *Science* **2004**, *306*, 2055, and references therein.

(2) Pike, A.; Horrocks, B.; Connolly, B.; Houlton, A. *Aust. J. Chem.* **2002**, *55*, 191.

(3) Ventra, M. D.; Zwolak, M. *Encyclopedia of Nanoscience and Nanotechnology* **2004**, *2*, 475.

(4) Brabec,V.; Paleček, E. *Biopolymers* **1972**, *11*, 2577.

(5) Ostana, V.; Paleček, E. *Langmuir* **2006**, *22*, 6481.

(6) Su, L.; Sankar, C. G.; Sen, D.; Yu, H. Z. *Anal. Chem.* **2004**, *76*, 5953.

(7) Wei, F.; Sun, B.; Guo, Y.; Zhao, X. S. *Biosens. Bioelectron.* **2003**, *18*, 1157.

(8) Cai, W.; Peck, J. R.; van der Weide, D. W.; Hamers, R. J. *Biosens. Bioelectron.* **2004**, *91*, 1013.

(9) Jiranek, I.; Peckova, K.; Kralova, Z.; Moreira, J. Barek, J. *Electrochimica Acta* **2009**, *54*, 1939.

(10) Maldonado, S.; Knapp, D.; Lewis, N. S. *J. Am. Chem. Soc.* **2008**, *130*, 3300.

(11) Braley, S. A.; Schneider, R. F. *J. Am. Chem. Soc.* **1921**, *43*, 740.

(12) Giese, B. *Annu. Rev. Biochem.* **2002**, *71*, 51, and references therein.

(13) Dekker, C.; Ratner, M. A. *Physics World* **2001**, 29.

Appendix I: Ellipsometry fitting

Experimentally determined Is (blue) and Ic (red) have been fitted with the model described in chapter 2.1; a bilayer system, an uniform monolayer on top of the crystalline silicon, is assumed (Figure AI.1). All the parameters with uncertainties were determined by the fitting.

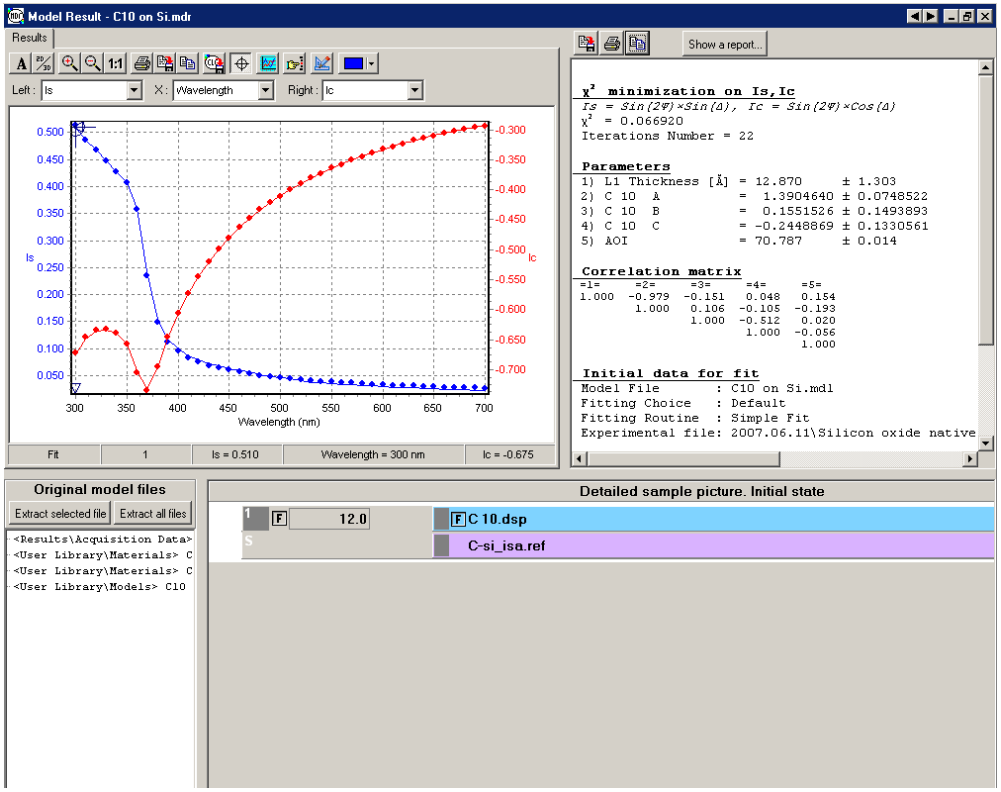

Figure I.1 The ellipsometry result of Si-C10 monolayer fitted with the model described.

Appendix II: SFG fitting

II.1 Fitting procedure

The equations 8 and 13 of chapter 2 are combined to express the SFG intensity:

$$I_{SFG} \propto \left| \vec{\vec{\chi}}^{(2)}_{eff,NR} + \sum_n \frac{\vec{\vec{A}}_{eff,n}}{\omega_{IR} - \omega_n - i\Gamma_n} \right|^2 \quad \textbf{(1)}$$

where $\vec{\vec{\chi}}^{(2)}_{eff,NR} = \vec{\vec{F}} : \vec{\vec{\chi}}^{(2)}_{NR}$, $\vec{\vec{A}}_{eff,n} = \vec{\vec{F}} : \vec{\vec{A}}_n$. A real and imaginary parts in $\vec{\vec{\chi}}^{(2)}_{NR}$ and $\vec{\vec{\chi}}^{(2)}_{R,n}$.

$$\vec{\vec{\chi}}^{(2)}_{NR} = \left|\vec{\vec{\chi}}^{(2)}_{NR}\right| e^{i\phi} = \left|\vec{\vec{\chi}}^{(2)}_{NR}\right| \cos\phi + i \left|\vec{\vec{\chi}}^{(2)}_{NR}\right| \sin\phi \quad \textbf{(2)}$$

$$\vec{\vec{\chi}}^{(2)}_{R,n} = \frac{\vec{\vec{A}}_n (\omega_n - \omega_{IR})}{(\omega_{IR} - \omega_n)^2 + \Gamma_n^2} + i \frac{\vec{\vec{A}}_n \cdot \Gamma_n}{(\omega_{IR} - \omega_n)^2 + \Gamma_n^2} \quad (3)$$

The terms 2 and 3 are substituted into equation 1:

$$I_{SFG} \propto \left\{ \left|\vec{\vec{\chi}}^{(2)}_{eff,NR}\right| \cos\phi + \sum_n \frac{\vec{\vec{A}}_{eff,n} (\omega_n - \omega_{IR})}{(\omega_n - \omega_{IR})^2 + \Gamma_n^{\,2}} \right\}^2 + \left\{ \left|\vec{\vec{\chi}}^{(2)}_{eff,NR}\right| \sin\phi + \sum_n \frac{\vec{\vec{A}}_{eff,n} \cdot \Gamma_n}{(\omega_n - \omega_{IR})^2 + \Gamma_n^{\,2}} \right\}^2 \quad \textbf{(4)}$$

which is used to fit all the SFG spectra. The fitting procedure has been carried out with Microcal Origin:

M1=A1/((B1−w)^2+C1^2) represents the term $\frac{A_n}{\omega_{IR} - \omega_n + i\Gamma_n}$;

M2=A2/((B2−w)^2+C2^2);

M3=A3/((B3−w)^2+C3^2);

M4=A4/((B4−w)^2+C4^2);

M5=A5/((B5−w)^2+C5^2);

U=3.14159/180*F represents the ϕ in radian;

R=D*cos(U)+M1*(B1−w)+M2*(B2−w)+M3*(B3−w)+M4*(B4−w)+M5*(B5−w

) represents $\left|\vec{\chi}^{(2)}_{eff,NR}\right|\cos\phi+\sum_n \frac{\vec{A}_{eff,n}(\omega_n-\omega_{IR})}{(\omega_n-\omega_{IR})^2+\Gamma_n^{\,2}}$;

I=D*sin(U)+M1*C1+M2*C2+M3*C3+M4*C4+M5*C5+M6*C6+M7*C7

represents $\left|\vec{\chi}^{(2)}_{eff,NR}\right|\sin\phi+\sum_n \frac{\vec{A}_{eff,n}\cdot\Gamma_n}{(\omega_n-\omega_{IR})^2+\Gamma_n^{\,2}}$;

S=(R)^2+(I)^2+s0 represents equation (4).

An example of SFG spectrum fitted with the corresponding parameters is shown below; the black squares are the data points and the red curve is the fit.

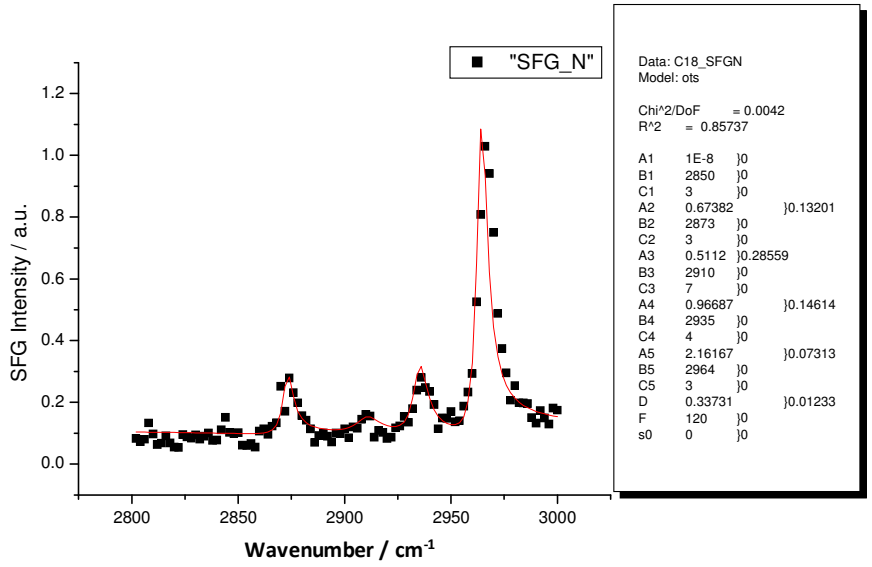

Figure II.1 SFG spectrum of Si-C18 monolayer fitted with equation 4.

II.2 Fitting parameters

For each vibrational band the fitting parameters were A (A_n), B (ω_{IR}), and C (Γ_n), while D($\chi^{(2)}_{NR}$) and F (ϕ_n) were kept the same for the entire spectrum. Another variable s0 was added to adjust baseline, although this term does not influence the spectra features as it is not frequency dependent. In the cases of fitting weak or overlapped bands, B and C can be fixed first, for which the initial values can be either obtained from the spectrum with well-resolved bands or the literature. The fitting is attempted multiple times to obtain best r^2 values. The parameter A, in some cases are fixed to the initial value obtained by the previous fitting routine; this is because multiple contributions from several peak elements are difficult to fit simultaneously. The fitting parameters for the SFG spectra are tabulated as following:

Methyl Ester Monolayer (Figure 3.5a top)

Parameter		**Parameter**		**Parameter**	
A1	2.7	**A3**	1.7	**A5**	1.7
B1	2850	**B3**	2905	**B5**	2956
C1	18	**C3**	10	**C5**	5
A2	1.4	**A4**	2.4	**D**	0.52
B2	2890	**B4**	2930	**F**	110
C2	14	**C4**	20	**s0**	0

Hydrolyzed Methyl Ester Monolayer (Figure 3.5a bottom)

Parameter		Parameter		Parameter	
A1	3	**A3**	4	**A5**	2.2
B1	2854	**B3**	2906	**B5**	2960
C1	18	**C3**	10	**C5**	8
A2	0.5	**A4**	2	**D**	0.43
B2	2890	**B4**	2930	**F**	110
C2	14	**C4**	16	**s0**	0.2

Ethyl Ester Monolayer (Figure 3.5b top)

Parameter		Parameter		Parameter	
A1	2.5	**A3**	2.5	**A5**	1.25
B1	2851	**B3**	2902	**B5**	2960
C1	20	**C3**	10	**C5**	6
A2	0.5	**A4**	1	**D**	0.53
B2	2890	**B4**	2930	**F**	110
C2	12	**C4**	12	**s0**	0

Hydrolyzed Ethyl Ester Monolayer (Figure 3.5b bottom)

Parameter		Parameter		Parameter	
A1	4	**A3**	1.8	**A5**	5.5
B1	2856	**B3**	2901	**B5**	2960
C1	17	**C3**	20	**C5**	30
A2	0.1	**A4**	6.1	**D**	0.36
B2	2885	**B4**	2928	**F**	110
C2	10	**C4**	15	**s0**	0.3

Propyl Ester Monolayer (Figure 3.5 c top)

Parameter		Parameter		Parameter	
A1	4	**A3**	3	**A5**	1.5
B1	2850	**B3**	2905	**B5**	2963
C1	18	**C3**	10	**C5**	5
A2	1.7	**A4**	3.1	**D**	0.72
B2	2885	**B4**	2930	**F**	110
C2	16	**C4**	8	**s0**	0

Hydrolyzed Proply Ester Monolayer (Figure 3.5c bottom)

Parameter		Parameter		Parameter	
A1	1.5	**A3**	2.8	**A5**	1.3
B1	2855	**B3**	2905	**B5**	2965
C1	9	**C3**	16	**C5**	12
A2	0.1	**A4**	3.6	**D**	0.46
B2	2885	**B4**	2934	**F**	110
C2	20	**C4**	13	**s0**	0

ssDNA NaCl (Figure 5.5a top)

Parameter		Parameter		Parameter	
A1	0.6	**A3**	6	**A5**	5
B1	2852	**B3**	2900	**B5**	2964
C1	8	**C3**	25	**C5**	6
A2	2	**A4**	2.8	**D**	0.095
B2	2877	**B4**	2930	**F**	-30
C2	12	**C4**	15	**s0**	0.2

dsDNA NaCl (Figure 5.5a bottom)

Parameter		Parameter		Parameter	
A1	0.7	**A3**	1.2	**A5**	1.5
B1	2848	**B3**	2900	**B5**	2964
C1	8	**C3**	15	**C5**	6
A2	1.1	**A4**	1.3	**D**	0.0260
B2	2872	**B4**	2930	**F**	-30
C2	6	**C4**	15	**s0**	0.2

ssDNA KCl (Figure 3.5b top)

Parameter		Parameter		Parameter	
A1	0.5	**A3**	5.7	**A5**	2.7
B1	2850	**B3**	2910	**B5**	2962
C1	6	**C3**	30	**C5**	6
A2	1	**A4**	1.5	**D**	0.125
B2	2870	**B4**	2930	**F**	-30
C2	7	**C4**	10	**s0**	0.2

dsDNA KCl (Figure 5.5b bottom)

Parameter		Parameter		Parameter	
A1	0.9	**A3**	4.7	**A5**	2.2
B1	2854	**B3**	2910	**B5**	2958
C1	10	**C3**	25	**C5**	7
A2	0.8	**A4**	1.7	**D**	0.007
B2	2875	**B4**	2922	**F**	-30
C2	7	**C4**	13	**s0**	0.1

ssDNA $CaCl_2$ (Figure 5.5c top)

Parameter		Parameter		Parameter	
A1	0.6	**A3**	6.5	**A5**	3.8
B1	2854	**B3**	2900	**B5**	2958
C1	8	**C3**	25	**C5**	7
A2	1.2	**A4**	2.7	**D**	0.006
B2	2870	**B4**	2928	**F**	-30
C2	7	**C4**	15	**s0**	0.15

dsDNA $CaCl_2$ (Figure 5.5c bottom)

Parameter		Parameter		Parameter	
A1	0.6	**A3**	6	**A5**	3.6
B1	2854	**B3**	2900	**B5**	2960
C1	8	**C3**	25	**C5**	7
A2	1.5	**A4**	3.0	**D**	0.05
B2	2872	**B4**	2928	**F**	-30
C2	10	**C4**	15	**s0**	0.1

ssDNA $MgCl_2$ (Figure 5.5d top)

Parameter		Parameter		Parameter	
A1	2.2	**A3**	6.5	**A5**	2.1
B1	2856	**B3**	2904	**B5**	2967
C1	15	**C3**	15	**C5**	5
A2	3.1	**A4**	2.8	**D**	7.5E-18
B2	2877	**B4**	2926	**F**	-30
C2	10	**C4**	8	**s0**	0.4

dsDNA $MgCl_2$ (Figure 5.5d bottom)

Parameter		Parameter		Parameter	
A1	2.2	**A3**	5	**A5**	2.5
B1	2856	**B3**	2910	**B5**	2962
C1	15	**C3**	20	**C5**	7
A2	2.5	**A4**	3	**D**	0.006
B2	2877	**B4**	2934	**F**	-30
C2	15	**C4**	10	**s0**	0.1

Au|C10-Si via thermal evaporation (Figure 6.3a)

Parameter		Parameter		Parameter	
A1	3	**A3**	2.8	**A5**	0.4
B1	2854	**B3**	2898	**B5**	2940
C1	10	**C3**	12	**C5**	5
A2	0.8	**A4**	2.3	**A6**	1.9
B2	2873	**B4**	2923	**B6**	2966
C2	6	**C4**	10	**C6**	5
D	1	**F**	-110	**s0**	0.85

Au|C12-Si via thermal evaporation (Figure 6.3b)

Parameter		Parameter		Parameter	
A1	1.18	**A3**	1.2	**A5**	0.9
B1	2856	**B3**	2902	**B5**	2940
C1	10	**C3**	12	**C5**	7
A2	0.7	**A4**	2.3	**A6**	1.6
B2	2876	**B4**	2922	**B6**	2966
C2	8	**C4**	10	**C6**	5
D	1	**F**	-110	**s0**	0.5

Au|C14-Si via thermal evaporation (Figure 6.3 c)

Parameter		Parameter		Parameter	
A1	2	**A3**	1.9	**A5**	0.4
B1	2856	**B3**	2900	**B5**	2940
C1	10	**C3**	10	**C5**	7
A2	0.6	**A4**	2.7	**A6**	1.4
B2	2876	**B4**	2920	**B6**	2966
C2	7	**C4**	10	**C6**	4
D	1	**F**	-90	**s0**	1

Au|C18-Si via thermal evaporation (Figure 6.3d)

Parameter		Parameter		Parameter	
A1	2.7	**A3**	0.9	**A5**	1
B1	2856	**B3**	2900	**B5**	2940
C1	10	**C3**	10	**C5**	7
A2	0.6	**A4**	3	**A6**	1.4
B2	2875	**B4**	2920	**B6**	2966
C2	7	**C4**	10	**C6**	4
D	1	**F**	-110	**s0**	0.73

Au|C10-Si via sputtering (Figure 6.4a)

Parameter		Parameter		Parameter	
A1	4.2	**A3**	5	**A5**	0.6
B1	2852	**B3**	2900	**B5**	2946
C1	10	**C3**	12	**C5**	5
A2	0.5	**A4**	7.5	**A6**	2.7
B2	2878	**B4**	2920	**B6**	2962
C2	8	**C4**	10	**C6**	5
D	1	**F**	-70	**s0**	2.51

Au|C12-Si via sputtering (Figure 6.4b)

Parameter		Parameter		Parameter	
A1	4	**A3**	5.8	**A5**	0.5
B1	2850	**B3**	2900	**B5**	2946
C1	10	**C3**	12	**C5**	5
A2	0.6	**A4**	7.6	**A6**	2.6
B2	2878	**B4**	2920	**B6**	2962
C2	8	**C4**	10	**C6**	5
D	1	**F**	-65	**s0**	2.43

Au|C14-Si via sputtering (Figure 6.4c)

Parameter		Parameter		Parameter	
A1	3.6	**A3**	3.3	**A5**	0.4
B1	2850	**B3**	2897	**B5**	2946
C1	10	**C3**	10	**C5**	5
A2	0.7	**A4**	6.9	**A6**	2.4
B2	2878	**B4**	2920	**B6**	2962
C2	8	**C4**	10	**C6**	5
D	1	**F**	-65	**s0**	2

Au|C18-Si via sputtering (Figure 6.4d)

Parameter		Parameter		Parameter	
A1	4.7	**A3**	4.4	**A5**	0.6
B1	2850	**B3**	2897	**B5**	2946
C1	10	**C3**	10	**C5**	5
A2	1.1	**A4**	7.91	**A6**	3.3
B2	2878	**B4**	2920	**B6**	2962
C2	8	**C4**	10	**C6**	5
D	1	**F**	-65	**s0**	2.8

Appendix III: Calculation of Fresnel factors

The Fresnel factors, F_{zzz} and F_{xxz}, are expressed as[1]

$$F_{ZZZ} = F_{ZZ}(\omega_{SFG}) \times F_{ZZ}(\omega_{Vis}) \times F_{ZZ}(\omega_{IR}) \times \sin\theta_{SFG} \times \sin\theta_{Vis} \times \sin\theta_{IR} \quad \textbf{(1)}$$

$$F_{XXZ} = (-F_{XX}(\omega_{SFG})) \times F_{XX}(\omega_{Vis}) \times F_{ZZ}(\omega_{IR}) \times \cos\theta_{SFG} \times \cos\theta_{Vis} \times \sin\theta_{IR} \quad (2)$$

These values for the monolayer/Au interface have been calculated using Maple software:

```
> anglev:=70; n1v:=1; n2v:=4.140 - I * 0.045;

                        anglev := 70

                         n1v := 1

                    n2v := 4.140 - .045 I

> angleI:=50; n1I:=1; n2I:=3.42+2e-11*I; n_m:=1.41; n_m_IR:=1.41;

                        angleI := 50

                         n1I := 1

                   n2I := 3.42 + .2e-10    I

                        n_m := 1.41

                       n_m_IR := 1.41

> T1v:=Pi/180*(anglev);

> T1I:=Pi/180*(angleI);
```

```
> T1s:=arcsin((18797 * sin(T1v) + 2900 * sin(T1I)) / (18797+2900));

> T2v:=(arcsin(n1v*sin(T1v)/n2v));

> T2I:=(arcsin(n1I*sin(T1I)/n2I));

> T2s:=(arcsin(n1s*sin(T1s)/n2s));

> #visible

> Lxxv:= evalf( abs(2*n1v*cos(T2v)/(n2v*cos(T1v)+n1v*cos(T2v))) );

                    Lxxv := .8150121920

> Lyyv:= evalf( abs(2*n1v*cos(T1v)/(n1v*cos(T1v)+n2v*cos(T2v))) );

                    Lyyv := .1563798564

> Lzzv:=

evalf(abs(2*n1v^2*n2v*cos(T1v)/n_m^2/(n2v*cos(T1v)+n1v*cos(T2v))) );

                    Lzzv := .5960531757

> #IR

> LxxI:= evalf( abs(2*n1I*cos(T2I)/(n2I*cos(T1I)+n1I*cos(T2I))) );

                    LxxI := .6143173792

> LyyI:= evalf( abs(2*n1I*cos(T1I)/(n1I*cos(T1I)+n2I*cos(T2I))) );

                    LyyI := .3233427000

> LzzI:=

 evalf( abs(2*n1I^2*n2I*cos(T1I)/n_m_IR^2/(n2I*cos(T1I)+n1I*cos(T2I))) );

                    LzzI := .6969883915
```

```
> #SFG
> Lxxs:= evalf( abs(2*n1s*cos(T2s)/(n2s*cos(T1s)+n1s*cos(T2s))) );
                        Lxxs := .6992953818
> Lyys:= evalf( abs(2*n1s*cos(T1s)/(n1s*cos(T1s)+n2s*cos(T2s))) );
                        Lyys := .1645784114
> Lzzs:=
evalf( abs(2*n1s^2*n2s*cos(T1s)/n_m^2/(n2s*cos(T1s)+n1s*cos(T2s))) );
                        Lzzs := .6543318915
> Fresnel Factor
> Fzzz:= evalf(Lzzs*Lzzv*LzzI*sin(T1s)*sin(T1v)*sin(T1I));
                        Fzzz := .1793382069
> Fxxz:= evalf(Lxxs*Lxxv*LzzI*cos(T1s)*cos(T1v)*sin(T1I));
                        Fxxz := .04163858424
```

The parameters are defined as follow:

anglev = angle of reflection for visible beam

angleI = angle of reflection for infrared beam

T1v = angle of reflection for visible beam (in radian)

T1I = angle of relfection for infrared beam (in radian)

T2v = angle of refraction for visible beam (in radian)

T2I = angle of refraction for infrared beam (in radian)

T1s = angle of reflection for sum frequency beam (in radian)

T2s = angle of refraction for sum frequency beam (in radian)

n1v = refractrive index of visible beam (air)

n2v = refractrive index of visible beam (Au)

n2I = refractrive index of infrared beam (air)

n2I = refractrive index of infrared beam (Au)

Lxxv = Fxx for visible beam

Lyyv = Fyy for visible beam

Lzzv = Fzz for visible beam

LxxI = Fxx for infrared beam

LyyI = Fyy for infrared beam

LzzI = Fzz for infrared beam

Lxxs = Fxx for sum frequency beam

Lyys = Fyy for sum frequency beam

Lzzs = Fzz for sum frequency beam

III.1 Bibliography

(1) Shen, Y. R. In *Nonlinear Spectroscopy for Molecular Structure Determination*, pp249-270*,* Field, R. W.; Hirota, E.; Maier, J. P.; Tsuchiya, S.*;* Blackwell Science Ltd.: Oxford*,* **1998**.

Appendix IV: Orientation of Methyl group

A molecular orientation of methyl group can be deduced from the ratio of SFG amplitudes estimated from the fit (Appendix II). The tilt angle of the molecular group is estimated by interpolating the obtained ratio to the simulated plot (signal ratio vs. tilt angle, i.e. Figure 6.5). Typically, the ratio of r^+ intensity in the ppp to that in the ssp polarization, the ratio of the r^- intensity in the sps to that in the ppp polarization, or the ratio of the r^- to r^+ intensities in the ppp polarization is used. In the simulation, the influence of fresnel factors (under effective polarization conditions) on the amplitudes is accounted to represent the observed signal intensity. The molecular orientation can be obtained from the molecular hyperpolazability that is expressed by Euler transformation of the estimated amplitudes (under the assumption of certain model). This appendix describes the method applied to determine the methyl tilt angles in chapter 6.

The second order non-linear electrical susceptibility, $\chi^{(2)}$ (equation 5.2), is a third-rank tensor having 27 elements (3^3) and expressed as:[1]

$$\chi^{(2)} = \begin{pmatrix} \chi^{(2)}_{xxx} & \chi^{(2)}_{xxy} & \chi^{(2)}_{xxz} & \chi^{(2)}_{xyx} & \chi^{(2)}_{xyy} & \chi^{(2)}_{xyz} & \chi^{(2)}_{xzx} & \chi^{(2)}_{xzy} & \chi^{(2)}_{xzz} \\ \chi^{(2)}_{yxx} & \chi^{(2)}_{yxy} & \chi^{(2)}_{yxz} & \chi^{(2)}_{yyx} & \chi^{(2)}_{yyy} & \chi^{(2)}_{yyz} & \chi^{(2)}_{yzx} & \chi^{(2)}_{yzy} & \chi^{(2)}_{yzz} \\ \chi^{(2)}_{zxx} & \chi^{(2)}_{zxy} & \chi^{(2)}_{zxz} & \chi^{(2)}_{zyx} & \chi^{(2)}_{zyy} & \chi^{(2)}_{zyz} & \chi^{(2)}_{zzx} & \chi^{(2)}_{zzy} & \chi^{(2)}_{zzz} \end{pmatrix} \quad (1)$$

Here $\chi^{(2)}_{ijk}$ describes i direction of electric susceptibility influenced by j component of electric field E_1 and k component of E_2. The underscripts i, j, k is defined by x, y, z Cartesian coordinates. With the isotropic surface such as the gold deposited on silicon (chapter 6), the $\chi^{(2)}$ can be reduced by symmetry considerations as follow:[1]

$$\chi^{(2)} = \begin{pmatrix} 0 & 0 & \chi^{(2)}_{xxz} & 0 & 0 & 0 & \chi^{(2)}_{xzx} & 0 & 0 \\ 0 & 0 & 0 & 0 & 0 & \chi^{(2)}_{yyz} & 0 & \chi^{(2)}_{yzy} & 0 \\ \chi^{(2)}_{zxx} & 0 & 0 & 0 & \chi^{(2)}_{zyy} & 0 & 0 & 0 & \chi^{(2)}_{zzz} \end{pmatrix} \quad (2)$$

Since the x and y axes are equivalent for an isotropic surface, $\chi^{(2)}_{ijk}$ components that can possibly contribute to a sum frequency signal are:

$$\chi^{(2)}_{xxz} = \chi^{(2)}_{yyz},\ \chi^{(2)}_{xzx} = \chi^{(2)}_{yzy},\ \chi^{(2)}_{zxx} = \chi^{(2)}_{zyy},\ \chi^{(2)}_{zxx} = \chi^{(2)}_{zyy},\ \chi^{(2)}_{zzz}$$

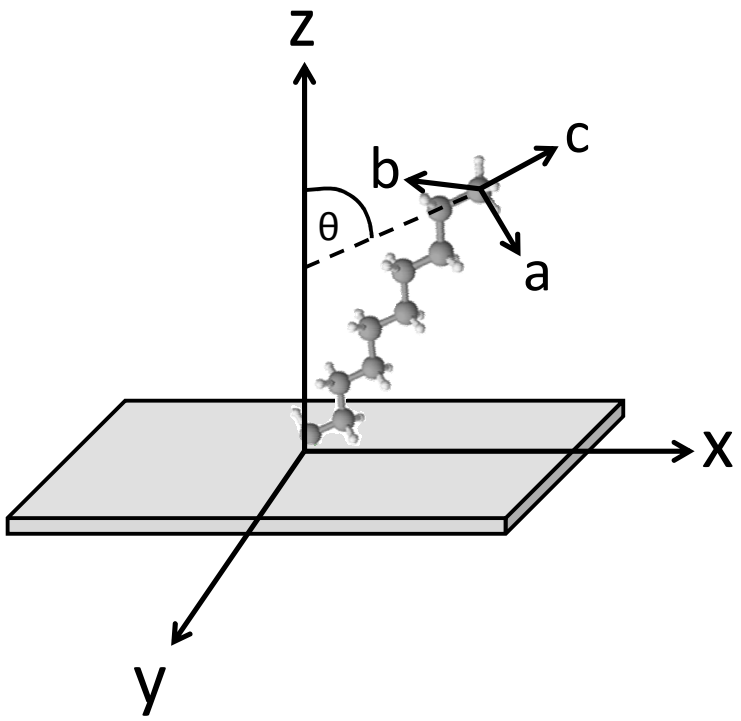

Figure IV.1 The Euler transformation converts molecular abc coordinate system to the macroscopic laboratory frame xyz.

In this thesis the tilt angles have been estimated from SFG spectrum obtained under ppp; under such polarization, the non-vanishing components are $\chi^{(2)}_{zzz}$, $\chi^{(2)}_{xzx}$, $\chi^{(2)}_{xxz}$, and $\chi^{(2)}_{zxx}$ (chapter 2.6.3) and the SFG intensity, I, is described as

$$I_{ppp} \propto \left| F_{zzz}\chi^{(2)}_{zzz} + F_{xzx}\chi^{(2)}_{xzx} + F_{xxz}\chi^{(2)}_{xxz} + F_{zxx}\chi^{(2)}_{zxx} + \chi^{NR}_{ppp} \right|^2 \quad (3)$$

where χ^{NR}_{ppp} is non-resonant contribution. On the metal surface, the x and y components of infrared electric field vanish and therefore equation 3 is further simplified to:

$$I_{ppp} \propto \left| F_{zzz}\chi^{(2)}_{zzz} + F_{xxz}\chi^{(2)}_{xxz} + \chi^{NR}_{ppp} \right|^2 \quad (4)$$

The Fresenel factors, F_{zzz} and F_{xxz}, in the above equations are expressed as:

$$F_{zzz} = F_{zz}(\omega_{SFG})F_{zz}(\omega_{VIS})F_{zz}(\omega_{IR})\sin\theta_{SFG}\sin\theta_{VIS}\sin\theta_{IR}\,\chi_{zzz} \quad (5)$$

$$F_{xxz} = F_{xx}(\omega_{SFG})F_{xx}(\omega_{VIS})F_{zz}(\omega_{IR})\cos\theta_{SFG}\cos\theta_{VIS}\sin\theta_{IR}\,\chi_{xxz} \quad (6)$$

$\chi^{(2)}$ is related to molecular hyperpolazability tensor, $\beta^{(2)}_{i,j,k}$, by:

$$\chi^{(2)}_{i,j,k} = N_s\langle\beta^{(2)}_{i,j,k}\rangle \quad (2\text{-}10)$$

The term $\beta^{(2)}_{i,j,k}$, which is defined within the macroscopic lab coordinate frame, can be represented in microscopic molecular coordinate frame; Euler transformation converts a, b, c coordinates to x, y, z coordinates (Figure IV.1). In fact, Hirose et al. have derived 729 unique mathematical expressions after the Euler transformation of each microscopic hyperpolarizability tensor.[2] Under the ppp polarization, $\beta^{(2)}$ of isotropic methyl group are described by the following equations[3]

for symmetric bands:

$$\beta_{zzz} = (\beta_{aac} - \beta_{ccc})(cos\theta - cos^3\theta) + \beta_{ccc}cos\theta$$

$$\beta_{xzx} = -(\beta_{aac} - \beta_{ccc})(cos\theta - cos^3\theta)/2$$

$$\beta_{xxz} = -(\beta_{aac} - \beta_{ccc})(cos\theta - cos^3\theta)/\,2\; + \beta_{aac}cos\theta$$

$$\beta_{zxx} = \beta_{xzx}$$

for antisymmetric bands:

$$\beta_{zzz} = 2\beta_{caa}(cos\theta - cos^3\theta)$$

$$\beta_{xzx} = \beta_{caa}cos^3\theta$$

$$\beta_{xxz} = -\beta_{caa}(cos\theta - cos^3\theta)$$

$$\beta_{zxx} = \beta_{xzx}$$

The intensity of each vibrational mode can be represented with above expressions and the fresnel factors determined in appendix III (equation 4). Then the ratio of r- and r+ signal intensity (ppp polarization) is

$$\left|\frac{A_q(r^-)}{A_q(r^+)}\right| = \left|\frac{\boldsymbol{\beta_{caa}}}{\boldsymbol{\beta_{aac}}} \times \frac{(2F_{zzz} - F_{xxz})(cos\theta - cos^3\theta)}{\left(F_{zzz} + \frac{1}{2}F_{xxz}(1+r)\right)cos\theta - \left(F_{zzz} - \frac{1}{2}F_{xxz}\right)(1-r)cos^3\theta} + \chi_{ppp}^{NR}\right|^2 \qquad (7)$$

Here r is β_{ccc}/β_{aac} . The molecular orientation of the methyl group, θ, is determined from the plot ($A_q(r^-)/ A_q(r^+)$) versus tilt angle (θ) (Figure 6.5) based on equation 7.

IV.1 Bibliography

(1) Lambert, A. G.; Davies, P. B.; Neivandt, D. J. *Appl. Spectrosc. Rev.* **2005**, *40*, 103.

(2) Hirose, C.; Akamatsu, N.; Domen, K. *Appl. Spectrosc.* **1992**, *46*, 1051.

(3) Watanabe, N.; Yamamoto, H.; Wada, A.; Domen, K.; Hirose, C.; Ohtake, T.; Mino, N. *Spectrochim. Acta* **1994**, *50A*, 1529.

Appendix V: Metal–Insulator-Semiconductor Junction

A potential barrier can originate from the differences in the work functions of the metal and the semiconductor.[1-3] The work function (φ) is the minimum energy required to remove an electron from the Fermi-Level (E_F) to vacuum (E_{Vac}); it is unique to a given material. The Fermi-Level is defined as the highest occupied electron state at 0 K. In an electrical conductor, the electron density is very high and the Fermi-Level is within an allowed band. On the other hand, in a semiconductor, the Fermi-Level is located within the band gap (Figure V.1a).

Upon the formation of the metal/ semiconductor interface, electrons diffuse from the side with more quasi-free electrons (higher E_F). Such electron transfer equilibrates the Fermi-Level (E_F is same for the both sides) and creates electric dipole at the junction; as the electrons move, they leave positive donor ion at the interface. This bends the band in the silicon and the potential barrier arises. In such case, difference between the work function of metal (φ_m) and the semiconductor's electron affinity (χ_s) is the barrier height (ϕ_b) of the junction:[1-3]

$$\phi_b = \varphi_m - \chi_s \qquad (1)$$

When an n-type semiconductor contacts a metal, electrons will flow from the semiconductor into the metal. This leads to a formation of a depletion region in the semiconductor and cause the band to bend upwards (Figure V.1b). The barrier arises from such band- bending. However, Hg | H-Si(n-type) junction exhibited ohmic

behaviour (Chapter 7.3.2) and hence the barrier height at the interface was not sufficient enough for the junction to rectify.

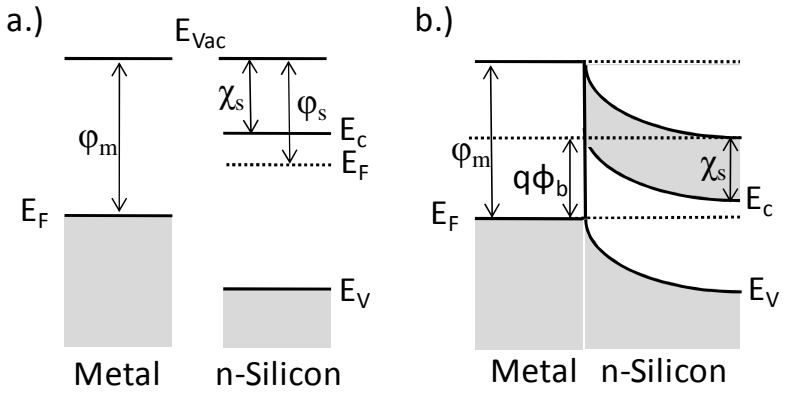

Figure V.1 Energy-band diagrams of metal-semiconductor (a) prior to and (b) in contact. under thermal equilibrium. EF, Ec, EVac are the energies of the Fermi-level, the conduction band of the n-type silicon, and the vacuum, respectively.

In contrast, upon incorporation of alkyl monolayer, Hg | $C_{10}H_{21}$-Si junction rectified. The unidirectional electron flow in such case can be explained by considering surface states and the insulating monolayer (Figure V.2). Here d represents insulating molecular layer. In the case of n-type silicon, Cowley and Sze have shown that the barrier height can be expressed as:[3]

$$\phi_b = \gamma(\varphi_m - \chi_s) + (1-\gamma)(E_g - \varphi_o) \tag{2}$$

$$\gamma = \frac{\varepsilon_1 \varepsilon_0}{\varepsilon_1 \varepsilon_0 + edD_s} \tag{3}$$

where E_g is the energy bandgap of the semiconductor, φ_o is the 'neutral level' (a surface state level in which interface becomes electrically neutral, when occupied), ε_1 is relative permittivity of the monolayer, ε_0 is the permittivity of free space, D_s is density of

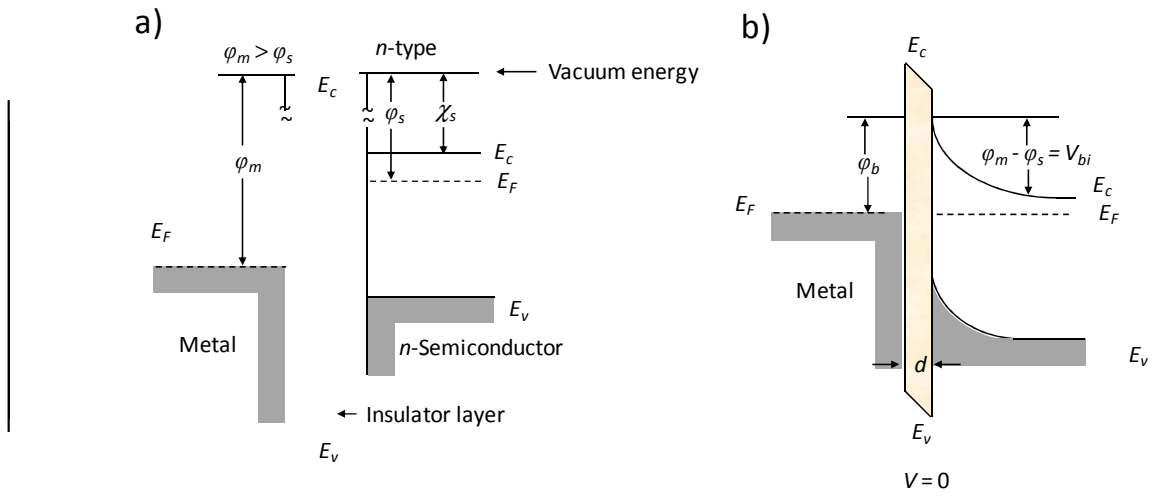

Figure V.2 Energy-band diagrams of metal-insulator-semiconductor (a) prior to and (b) in contact.

surface states per electron-volt per unit area of semiconductor surfaces, and e is. When the insulator thickness, d, is zero, $\gamma = 1$ and equation (2) becomes equation (1), $\phi_b = \varphi_m - \chi_s$ and therefore, φ_m influences the barrier height. On the other hand, when the term edD_s in equation (3) is prominent, the barrier height of the junction will be governed by the term $(E_g - \varphi_o)$; the barrier height is no longer dictated by φ_m.

V.1 Bibliography

(1) Anderson, B. L.; Anderson, R. L. *Fundamentals Semiconductor Devices*. McGraw-Hill: New York, USA, **2005**.

(2) Sze, S. M. Physics of Semiconductor Devices, 2nd ed. John Wiley and Sons: New Jersey, USA, **1981**.

(3) Rhoderick. E. H. *J. Phys. D: Appl. Phys.* **1970**, *3*, 1153.

Appendix VI: J-V reproducibility of Au deposited samples

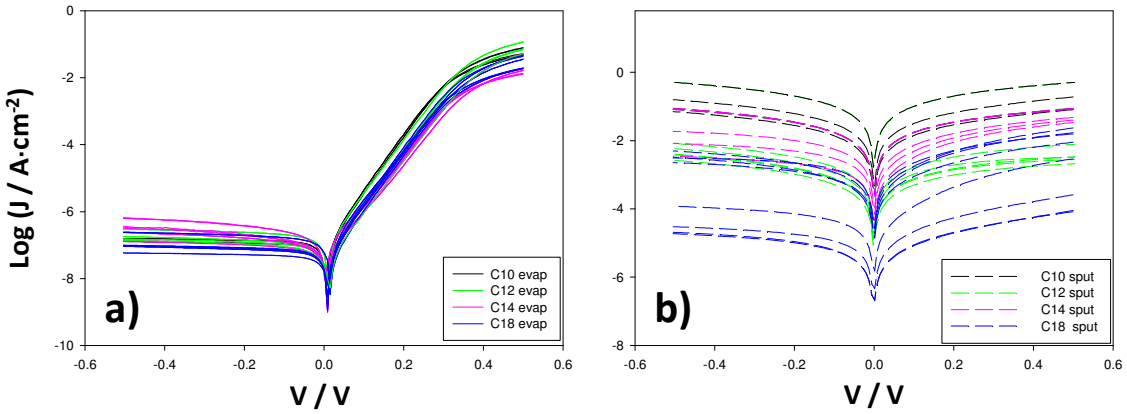

Figure VI.1 Current density-bias voltage (*J-V*) plots of at least three independent samples of Au/n-alkyl monolayer/Si junctions, for which the alkyl chain length was systematically varied. The gold contacts were prepared by (a) thermal evaporation and (b) sputtering deposition, respectively.

J-V curves of Au/n-alkyl monolayer/Si junctions prepared by thermal deposition (Figure VI.1a) exhibited high reproducibility which is comparable to Hg/$C_{10}H_{21}$/Si junctions (Chapter 7.3.4). In contrast, Au contact formed by sputtering results in a poorer J-V curve reproducibility however, the trend exists; as the chain length increases, the junction appear to be less conductive and the rectifying behaviour became more prominent (i.e., the current at forward bias becomes much higher than that at the revised bias).